STATUS OF THESIS

Title of thesis

| MODELING OF FLOW AND PARTICLE DYNAMICS IN HUMAN RESPIRATORY SYSTEM USING COMPUTATIONAL FLUID DYNAMICS |

I_____ DANG DINH THANG _____

hereby allow my thesis to be placed at the Information Resource Center (IRC) of Universiti Teknologi PETRONAS (UTP) with the following conditions:

1. The thesis becomes the property of UTP

2. The IRC of UTP may makes copies of the thesis for academic purposes only.

3. This thesis is classified as

☐ Confidential

☐ Non-confidential

If this thesis is confidential, please state the reason:

_____

_____

The contents of the thesis will remain confidential for _____ years.

Remarks on disclosure:

_____

_____

Endorsed by

_____            _____

Signature of Author                 Signature of Supervisor

Permanent address                   Name of Supervisor

133 To Hieu,

Le Chan Dist., Hai Phong city,       Dr. Nurul Hasan

Vietnam.

Date: _____            Date: _____

UNIVERSITI TEKNOLOGI PETRONAS

MODELING OF FLOW AND PARTICLE DYNAMICS

IN HUMAN RESPIRATORY SYSTEM USING

COMPUTATIONAL FLUID DYNAMICS

by

DANG DINH THANG

The undersigned certify that they have read, and recommend to the Postgraduate Studies Programme for acceptance this thesis for the fulfillment of the requirements for the degree stated.

Signature: _____

Main Supervisor: Dr. Nurul Hasan _____

Signature: _____

Head of Department: Associate. Professor. Dr. Shuhaimi Mahadzir _____

Date: _____

MODELING OF FLOW AND PARTICLE DYNAMICS

HUMAN RESPIRATORY SYSTEM USING

FLUID DYNAMICS


by


DANG DINH THANG


A Thesis

Submitted to the Postgraduate Studies Programme

as a Requirement for the Degree of


MASTER OF SCIENCE

CHEMICAL ENGINEERING

UNIVERSITI TEKNOLOGI PETRONAS

BANDAR SERI ISKANDAR,

PERAK


JUNE 2011

# DECLARATION OF THESIS

Title of thesis
> MODELING OF FLOW AND PARTICLE DYNAMICS IN HUMAN RESPIRATORY SYSTEM USING COMPUTATIONAL FLUID DYNAMICS

I_____ DANG DINH THANG _____

hereby declare that the thesis is based on my original work except for quotations and citations which have been duly acknowledged. I also declare that it has not been previously or concurrently submitted for any other degree at UTP or other institutions.

Endorsed by

_____          _____

Signature of Author                                        Signature of Supervisor

Permanent address                                       Name of Supervisor
133 To Hieu,
Le Chan Dist., Hai Phong city,                      Dr. Nurul Hasan
Vietnam.


Date: _____          Date: _____

# ACKNOWLEDGEMENTS

# ABSTRACT

The aim of this research is to study numerically the flow characteristics and particle transport within a human respiratory system, including the human nasal cavity and the bifurcation. Various flow rates and particle sizes are main parameters varied in order to analyze the effects on particle movements and deposition on the human respiratory system. There are three main systems considered in this research: flow around a blockage in a channel, flow in the Final particle deposition with Stokes number, St = 0.12 for inlet flow rates of: (a) 30 L/min; (b) 60 L/min in human nasal cavity, and flow in the double bifurcation. Computational Fluid Dynamics (CFD) is used to solve gas-particle flow equations using a commercial software, FLUENT.

Flow around a blockage in a channel was performed to gain confidence in the CFD model that has recirculation zone behind the block. The unsteady vortices flow around this blockage is investigated for Reynolds numbers, Re = 150, 300, 600, 900, and 1200 and Stokes numbers, $St$ = 0.01, 0.1, 0.5, 1.0 and 2.0 by solving momentum and particle model equations. A detailed airflow structures such as vortices, flow distribution are obtained. It was found that the particle distribution depends on vortical structures and Stokes number.

A model of real human nasal cavity is reconstructed from computerized tomography (CT) scans. The flow structure is validated with experimental data for flowrates of 7.5 L/min (Re = 1500) and 15 L/min (Re = 3000). The total particle deposition in nasal cavity is also validated with experimental data using inertial parameter. Then the model is further investigated the effect of turbulence on particle deposition with flowrates of 20, 30 and 40 L/min. Deposition was found to increase with Stoke number for the same Reynolds number.

Three-dimensional double bifurcations with coplanar configurations are employed to investigate the flow. Results of laminar flow (Re = 500, Re = 1036, and Re = 2000) are used to compare with experimental and numerical solution for validation. The model is further used to investigate the turbulent flow and particle deposition for heavy breathing with flowrates of 30 L/min (Re = 7300) and 60 L/min (Re = 14600). It was found that the deposition efficiency is dependent on Reynolds number and Stokes numbers. This research outcome will guide to improve the injection particle drugs to human lungs and to develop nasal mask to protect the lungs from hazardous particles.

ABSTRAK

Kajian ini dilakukan bertujuan untuk mengkaji ciri-ciri aliran dan pergerakan partikel di dalam sistem pernafasan manusia yang merangkumi rongga hidung dan saluran pernafasan bahagian atas secara numerikal. Parameter-parameter utama yang dimanipulasikan untuk menganalisis kesan ke atas pergerakan partikel dan pemendapan ialah kelajuan aliran dan saiz partikel. Terdapat tiga sistem utama diambil kira dalam kajian ini: aliran di dalam saluran yang tersumbat, aliran di dalam rongga hidung manusia dan aliran di dalam sistem pernafasan manusia – bifurkasi berganda. Pengkomputeran Dinamik Cecair (CFD) digunakan untuk menyelesaikan persamaan aliran gas-partikel menggunakan perisian komersil FLUENT.

Kajian terhadap aliran di dalam saluran yang tersumbat dijalankan bagi menambahkan keberkesanan model CFD di mana mengandungi zon peredaran semula di belakang blok. Di samping itu, ia juga mempunyai banyak data eksperimen untuk dibandingkan. Kajian pergerakan vortikal yang tidak stabil melalui silinder tiga segi dijalankan menggunakan nombor Reynolds, Re = 150, 300, 600, 900, dan 1200 manakala nombor Stokes yang digunakan ialah, $St$ = 0.01, 0.1, 0.5, 1.0 dan 2.0 dengan menyelesaikan persamaan Navier-Stokes dan model partikel. Struktur terperinci aliran udara seperti gerakan vorteks dan peredaran aliran dapat diperolehi. Ini menunjukkan bahawa peredaran aliran bergantung kepada struktur vortikal and nombor Stokes.

Model sebenar rongga hidung manusia dibina semula berdasarkan imej imbasan CT. Struktur aliran disahkan dengan data eksperimen menggunakan kelajuan aliran 7.5 L/minit (Re = 1500) dan 15 L/minit (Re = 3000). Jumlah pemendapan partikel di dalam rongga hidung juga disahkan dengan data eksperimen menggunakan parameter inersia. Kajian dijalankan ke atas model ini untuk mengkaji gerakan turbulen dan pemendapan partikel menggunakan kelajuan aliran sebanyak 20, 30 dan 40 L/minit. Pemendapan partikel didapati meningkat apabila nombor Stokes bertambah dengan menggunakan nombor Reynolds sama.

Kajian untuk aliran dijalankan menggunakan bifurkasi berganda 3-dimensi dengan konfigurasi coplanar dan $90^o$ bukan planar. Hasil dari aliran laminar (Re = 500, Re = 1036, dan Re = 2000) digunakan untuk membandingkan data secara eksperimen dan numerikal untuk pengesahan.Model ini kemudian digunakan untuk mengkaji aliran turbulen dan pemendapan partikel bagi kesukaran pernafasan dengan kelajuan aliran 30 L/minit (Re = 7300) dan 60 L/minit (Re = 14600). Kajian mendapati  keberkesanan pemendapan bergantung kepada nombor Reynolds dan nombor Stokes. Hasil daripada kajian ini akan dapat memberi panduan bagi penambahbaikan dalam proses penyuntikan partikel ubat ke dalam paru-paru manusia dan juga bagi penciptaan penutup hidung untuk melindungi paru-paru dari partikel-partikel berbahaya.

TABLE OF CONTENTS

Chapter

# LIST OF FIGURES

xiii

# LIST OF TABLES

# LIST OF SYMBOLS

| | |
|---|---|
| $A_C$ | Relative acceleration factor |
| $B$ | Square cylinder side length |
| Br | Blockage ratio $B/H$ |
| $C_A$ | Correction factor for high Re effect in added mass |
| $C_D$ | Drag coefficient |
| $C_{Ds}$ | Correction factor for high Re effect on the steady state drag coefficient |
| $C_H$ | Correction factor for high Re effect in Basset history term |
| $d_{ij}$ | Deformation rate tensor |
| $d_1, d_2, d_3$ | Diameter of generation 1, 2 and 3 tubes |
| $d_p, d_{inlet}$ | Particle and inlet diameter |
| $d_{ae}$ | Aerodynamic equivalent diameter |
| $\varepsilon$ | Particle to fluid density ratio |
| $\vec{F}$ | Force vector |
| $\vec{F}_{grav}, \vec{F}_{drag}$ | Gravity and drag force vectors |
| $F_d$ | Drag force |
| $Fr$ | Froude number |
| $g$ | Gravitational acceleration |
| $g_x$ | Gravity in x-direction |
| $G(x, x')$ | Filtered function |
| $H$ | Channel height |
| $I$ | Inertial parameter |
| $L$ | Fluid molecules mean free path |
| $L_1, L_2, L_3$ | Length of duct in generation 1,2,3 |
| $p$ | Pressure |

| | |
|---|---|
| $P$ | Outlet pressure |
| $\bar{P}$ | Filtered Pressure |
| $Q_{in}$ | Inlet flow rate |
| $r_{b1}, r_{b2}$ | Bifurcation 1 and 2 radius of curvature |
| $r_{c1}, r_{c2}$ | Radius of curvature |
| $R$ | Correlation coefficient |
| $\text{Re}$ | Reynolds number |
| $\text{Re}_p$ | Particles Reynolds number $\left( = u_p d_p \rho_p / \mu \right)$ |
| $SF$ | Stream function (Psi) |
| $St$ | Stokes number |
| $t$ | Time |
| $t_p$ | Particle response time |
| $u$ | Instantaneous fluid velocity |
| $u_i$ | Mean flow fluid velocity |
| $u_j$ | Gas velocity vector |
| $u, u_p$ | Inlet velocity and particle velocity |
| $\bar{u}_i, \bar{u}_j$ | Filtered velocity |
| $u_{pj}$ | Particle velocity vector |
| $u_m$ | Velocity at the channel entrance |
| $u_p$ | Relative particle velocity |
| $V$ | Volume of computational cell |
| $x_i$ | Particle position |
| $\rho_g$ | Gas density |
| $\rho$ | Fluid density |
| $\rho_p$ | Particle density |
| $\nu$ | Kinematic viscosity |
| $\nabla$ | Laplace operator |

| | |
|---|---|
| $\delta_{ij}$ | Delta function |
| $\mu$ | Fluid viscosity |
| $\omega$ | Vorticity |
| $\sigma_{ij}$ | Stress tensor |
| $\bar{\phi}(x)$ | Filtered operator |
| $\theta_1, \theta_2$ | Bifurcation half-angle |

CHAPTER 1

INTRODUCTION


## 1.1 Introduction

Urban air pollution can potentially cause respiratory diseases [1]. During inhalation, air may contain toxic particle that may harm the body. In working environment of particular industries (i.e. sanding, wood processing, concrete cutting), foreign toxic particles are the possible harm caused to human during the inhalation process. Furthermore, urban air contains foreign particles due to vehicle exhausts and industrial by-products. By breathing oxygen in the air, foreign particles are brought into the lungs and into close contact with the blood. Blood absorbs oxygen and simultaneously gives up carbon-dioxide, which is carried out of the lungs when air is breathed out.

The effects of inhaling particulate matter have been widely studied in humans and animals and include asthma, lung cancer, cardiovascular disease, and premature death. According to Jayaraju [2], since 2000, particulate matter pollution is estimated to cause 22,000 to 52,000 deaths per year in the United States and 200,000 deaths per year in Europe. The size of the particle is a main determinant of where in the respiratory tract the particle will deposit when inhaled. Larger particles ($> 10 \mu m$) are generally filtered in the nose and throat and do not cause adverse problems, but particulate matter smaller than about 10 $\mu m$ can settle in the bronchi and lungs and cause health problems. The 10 $\mu m$ size does not represent a strict boundary between respirable and non-respirable particles, but has been agreed upon for monitoring of airborne particulate matter by most regulatory agencies. Similarly, particles smaller than approximately 2 $\mu m$ tend to penetrate into the gas-exchange regions of the lung, and very small particles ($< 100$ nanometers) may pass through the lungs to affect other organs [2].

According to World Health Organization (WHO), around 300 million people suffer from asthma and around 255,000 people died of asthma in 2005 [3]. It is predicted that the asthma deaths will increase by 20% in the coming 10 years if proper care is not taken. Inhaled medication is the preferred method of drug administration to the lung for the first-line therapy of asthma and chronic obstructive pulmonary diseases. Asthma is a chronic condition in which the airways occasionally constrict, become inflamed, and are lined with excessive amounts of mucus. Symptomatic control of episodes of wheezing and shortness of breath due to asthma is generally achieved with fast acting bronchia-dilators, which are basically pocket-sized pharmaceutical aerosol inhalers [3]. While targeting a delivery dose of inhaled pharmaceutical aerosol to the lower airways, a high percentage of it is lost due to deposition and clearance in the upper airways. Furthermore, adverse health effects such as cellular damage, inflammation and tumor formation can occur in the upper airways potentially as a result of local deposition and absorption patterns [4].

Recent research has proven that from 1995 to current inhalation therapies have only 10-20% delivery of drug load to the lung with an effective inhalation [5]. In addition, Roland et al. [6] reviewed that extra drug load (80-90%) of certain types of drugs - corticosteroid drugs, such as: budesonide, prednisolone - can cause serious side effects to patient. The efficiency of those products was measured by the amount of particle deposited on the vascular mucous walls. Accurate prediction of inhaled particle deposition in the human nasal cavity and lower airway should provide useful information to clinical researchers to innovate the inhalation therapies. Investigation on the gas-particle flows in the human nasal cavity and human lower airway will provide understanding on the mechanism and behavior of particle deposition inside the human nasal cavity and lung. There have been numerous researches on the deposition of aerosol particles in the human nasal cavity and respiratory system [7-13]. Many works have been done to investigate the parameters that can affect the deposition of aerosols. Particle properties, breathing conditions and lung geometry are known to be the main factors influencing the deposition of aerosols. Different particle properties and breathing conditions have been studied extensively. However, experimental studies would be very costly and difficult to conduct to study the particle transport and deposition in the human nasal cavity and lower airway.

Numerical simulations provide wide range of study with repeatability and accuracy based on the advance of powerful computers employing Computational Fluid Dynamics (CFD) techniques. The disadvantage of using CFD is the lack of precise geometry with more realistic boundary conditions, which may produce less reliable results. In addition, air flow studies of the nasal cavity are important in establishing the effects of airway geometry on the airflow, particularly in abnormal nasal cavity anatomies. These anomalies may impair airflow by producing narrowed or obstructed areas leading to adverse health effects. For example, spurs and deviation of the nasal septum (nasal wall that separates the left and right cavity) may impair airflow, especially if the spur or deviated septum compresses the middle airway walls (turbinates) or lateral wall of the nasal cavity, leading to obstruction of the airway and compression of the turbinates.

For the above reasons, it is utmost important to understand the fluid-particle dynamics in the lower airways. The present thesis is a step forward in attempts to understand this important and very interesting aspect of biomechanics. By understanding the air flow dynamics caused by geometrical differences especially anomalies; better clinical appraisals can be delivered, leading to better informed decision-making on surgical procedures. The computational simulation can act as a predictive or 'virtual surgery' tool, which will improve medical planning, patient recovery, and reduce the overall risks of surgery. In this thesis, realistic human nasal cavity has been reconstructed successfully and therefore; numerical simulations were carried out with validation of experimental data.

## 1.2 Objectives

In overall, this study is to numerically investigate the effects of flow (Reynolds number) and particle sizes (Stokes number) effects of particle distribution and deposition in human respiratory system: upper airway system – human nasal cavity and lower airway system – human lung. It is to assist practical clinical studies where information regarding airflow structures, deposition efficiencies and deposition patterns in human nasal cavity and human lung were presented. An additional research of particle flow in blocked channel – a simple geometry, is to understand the

basic knowledge of flow to a blocked object, which exists in the human nasal cavity and double bifurcation.

### 1.2.1 Flow in Blocked Channel

The objective of this section is to numerically simulate and analyze particle transport in an unsteady laminar flow over a square cylinder placed in a channel and to differentiate the flow regimes with different Reynolds (Re = 150, 300, 600, 900 and 1200) and different Stokes numbers (*St* = 0.01 - 2.0). The particles injected in such complex, transient flows are subjected to both unsteady lift and drag forces. Detailed two dimensional simulation model and flow visualization are employed to analyze the transient flow field and vortex dynamics, as well as the particle dynamics and dispersion behavior.

### 1.2.2 Fluid Flow and Particle Deposition in Human Nasal Cavity

This section focuses on the understanding and prediction of particle transport and deposition characteristics in the human lower respiratory airways is important for targeting the delivery of drug particles or assessing the health risks of inhaled pollutant particles. It is to develop numerical simulation that can accurately predict both the air and particle flow and deposition patterns under the realistic physiological conditions of the lower airway system for different inlet flowrates $Q = 7.5 \ L/\min$ (Re = 1500, 3000, 4000 and 6000). Particles were injected with different sizes to study particles flow and deposition patterns in nasal cavity and also the effects of inertial parameter, Stokes number and particle Reynolds number on deposition efficiency $(\eta)$. Several important effects were neglected: various realistic airway geometry for accurate flow description; turbulent fluctuating eddies acting on the particle trajectory ultimately influenced on deposition patterns; and the consideration of mucus of airway and nasal hair affecting the particle deposition.

### 1.2.3 Fluid flow and particle deposition in double bifurcation

This section focuses on the understanding and prediction of particle transport and deposition characteristics in the human lower respiratory airways – double bifurcation is important for targeting the delivery of drug particles or assessing the health risks of inhaled pollutant particles. The model of double bifurcation is reconstructed and used to develop numerical simulation that can accurately predict both the air and particle flow and deposition patterns under the realistic physiological conditions of the lower airway system for light breathing (Re = 500, 1036 and 2000) and heavy breathing rates of 30 L/min (Re = 7,264) and 60 L/min (Re = 14,528). The model is verified and validated with numerical data by Comer *et al.* [10] and experimental data of Kim & Fisher [14]. Particles were injected with different sizes to study particles flow and deposition patterns in double bifurcation and also the effects of Stokes number on deposition efficiency $(\eta)$.

### 1.3 Thesis Structure

The rationale for conducting this research, the objectives and outlines of this thesis are explained in Chapter 1.

In Chapter 2, an in-depth review of the background for this research is provided. The chapter begins with an introduction to human airway system, and followed by detailed flow regimes with different methods. The previous studies on flow in blocked channel, in human nasal cavity and human lung were introduced. And finally, basic understanding on grid independence test and computational fluid dynamics solver procedures are explained.

In Chapter 3, it addresses the governing equations of fluid and particle flows of all three cases. The steps to reconstruct the human nasal cavity from CT scans were explained. All dimension details, boundary conditions and test cases are listed in this chapter.

In Chapter 4, it shows the verification and validation of the model with previous experimental and numerical data. The fluid flow and particle flow patterns in all three cases were illustrated with figures. Effects of Stokes number, Reynolds number, inertial parameter to fluid flow, particle flow and particle deposition patterns were studied. The results will contribute useful information to improve the medical treatment for airway diseases.

The thesis concludes within Chapter 5 by summarizing significant outcomes from each research sections presented in whole study. The final section of this chapter highlights the potential clinical significance of this study and provides recommendation for future work.

CHAPTER 2

LITERATURE REVIEW

## 2.1 Human Upper Airway System

Fig. 2.1 shows a schematic representation of the human respiratory system as well as the respiratory pathway. The respiratory system is basically divided into three categories namely the extra-thoracic region, the trachea-bronchial region and the alveolar region.
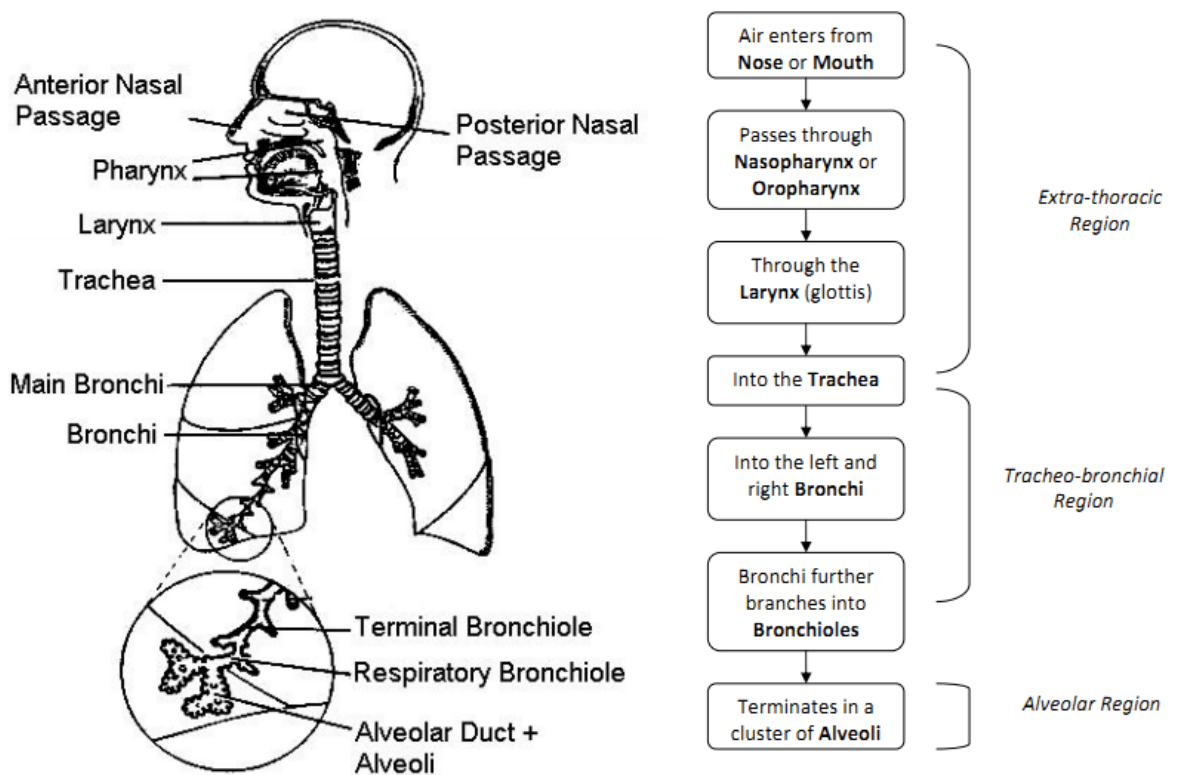


Figure 2.1: Left: Schematic representation of the human respiratory system; Right: The respiratory pathway. (Source: Computational fluid-particle dynamics lab) [15]

- *Extra-thoracic region*

The nose (nasal cavity) is the preferred entrance for outside air into the respiratory system. The nasal passage serves as a moistener, a filter, and a warm up before the air intake. While the hairs in the nostrils act as a filter for the foreign particles, the mucus and cilia (tail like projections on the surface) collect dust, bacteria and other particles in the air.

The main function of pharynx (throat) is to collect the air coming from the nose and mouth, and pass it downstream towards trachea. The pharynx is further subdivided into nasopharynx and oropharynx. In subjects with oral allergy syndrome and related allergies, the pharynx is often a reaction site to allergens, with common symptoms including burning and itching.

The larynx (glottis, voice box) houses the vocal chords and as the air is expired, the vocal chords vibrate. Humans can control these vibrations which enable us to make sound. The vocal folds affect the shape and magnitude of glottis cross-section depending on the flow rate and are seen to be a crucial geometric feature to be considered in the airflow dynamics study [16].

The trachea is a tube-like structure which acts as a passage from the pharynx to the lungs. The trachea is kept open by cartilage rings within its walls. The presence of cartilage rings can have a considerable effect on the flow dynamics [17]. Trachea roughly measures 10-14 cm in length and 16-20 mm in diameter. Similar to nasal cavity, trachea is covered with ciliated mucous membrane which acts as a filter for foreign particles.

- *Trachea-bronchial region*

The trachea further divides into two cartilage-ringed and ciliated tubes called the main bronchi. The bronchi enter the lungs and spread into a tree-like structure by further subdividing itself into the lobar bronchi, segmental bronchi and finally ends up becoming tiny terminal bronchioles (approximately 30,000) leading into the gas exchanging (alveolated) zone. The trachea-bronchial region is also referred to as the

lower airways. The extra-thoracic and trachea-bronchial airways taken together are called the 'conducting airways' as they transport air to the gas-exchange region of the lungs. The term central airway is sometimes used to refer to the upper regions of the trachea-bronchial airways [18].

- *Alveolar region*

Each terminal bronchiole subtends an air chamber that could be like a bunch of grapes. Each chamber contains many cup-shaped cavities known as alveoli. The walls of the alveoli, which are only about one cell thick, are the respiratory surface. They are thin, moist, and are surrounded by several numbers of capillaries. The estimation is that lungs contain about 300 million alveoli and that the thin barrier with a large surface makes it ideal for the exchange of oxygen and carbon dioxide between blood and through these walls. Their total surface area is roughly about $70 \, m^2$.

## 2.2 Flow Regimes

When a fluid is flowing through a closed channel such as a pipe or between two flat plates, either of two types of flow may occur depending on the velocity of the fluid: laminar flow or turbulent flow. The type of flow occurring in a fluid in a channel is important in fluid dynamics problems. The dimensionless Reynolds number is an important parameter in the equations that describe whether flow conditions lead to laminar or turbulent flow.

## 2.2.1 Laminar Flow

Laminar flow, sometimes known as streamline flow, occurs when a fluid flows in parallel layers, with no disruption between the layers [19]. At low velocities the fluid tends to flow without lateral mixing, and adjacent layers slide past one another like playing cards. There are no cross currents perpendicular to the direction of flow,

nor eddies or swirls of fluids [20]. In laminar flow the motion of the particles of fluid is very orderly with all particles moving in straight lines parallel to the pipe walls [21]. In fluid dynamics, laminar flow is a flow regime characterized by high momentum diffusion and low momentum convection. Laminar flow is the opposite of turbulent flow which occurs at higher velocities where eddies or small packets of fluid particles form leading to lateral mixing. In nonscientific terms laminar flow is "smooth", while turbulent flow is "rough".

The type of flow occurring in a fluid in a channel is important in fluid dynamics problems. The dimensionless Reynolds number is an important parameter in the equations that describe whether flow conditions lead to laminar or turbulent flow. In the case of flow through a straight pipe with a circular cross-section, Reynolds numbers of less than 2100 [22] are generally considered to be of a laminar type; however, the Reynolds number upon which laminar flows become turbulent is dependent upon the flow geometry. When the Reynolds number is small, creeping motion or Stokes flow occurs. This is an extreme case of laminar flow where viscous (friction) effects are much greater than inertial forces. The common application of laminar flow would be in the smooth flow of a viscous liquid through a tube or pipe. In that case, the velocity of flow varies from zero at the walls to a maximum along the centerline of the vessel. The flow profile of laminar flow in a tube can be calculated by dividing the flow into thin cylindrical elements and applying the viscous force to them [23].


## 2.2.2  Turbulent Flow


*2.2.2.1 Overview*


In fluid dynamics, turbulence or turbulent flow is a flow regime characterized by chaotic and stochastic property changes. This includes low momentum diffusion, high momentum convection, and rapid variation of pressure and velocity in space and time. While there is no theorem relating Reynolds number to turbulence, flows with high

Reynolds numbers usually become turbulent, while those with low Reynolds numbers usually remain laminar. For pipe flow, a Reynolds number above about 4000 will most likely correspond to turbulent flow, while a Reynolds number below 2100 indicates laminar flow. The region in between (2100 < Re < 4000) is called the transition region. In turbulent flow, unsteady vortices appear on many scales and interact with each other. Drag due to boundary layer skin friction increases. The structure and location of boundary layer separation often changes, sometimes resulting in a reduction of overall drag. Although laminar-turbulent transition is not governed by Reynolds number, the same transition occurs if the size of the object is gradually increased, or the viscosity of the fluid is decreased, or if the density of the fluid is increased [24].

Turbulence is highly characterized by the following features,

- *Irregularity:* Turbulent flows are always highly irregular. This is why turbulence problems are always treated statistically rather than deterministically. Turbulent flow is always chaotic but not all chaotic flows are turbulent.

- *Diffusivity:* Turbulence is highly associated with rapid mixing. One of the useful effects of turbulence, it tends to accelerate the homogenization of any non-uniform fluid mixture. The process which brings any non-uniform state of a system into a uniform one is called mixing and when the system is in its uniform state, the system becomes a homogeneous system. A mixing process requires sufficient input of energy which is readily available in a turbulent flow. The characteristic which is responsible for the enhanced mixing and increased rates of mass, momentum and energy transports in a flow is regarded as diffusivity.

- *Dissipation ($\varepsilon$):* To sustain turbulent flow a constant source of energy supply is required. Otherwise, turbulence dissipates rapidly as the kinetic energy is converted into internal energy (heat) by viscous shear stress. Turbulence causes the formation of eddies of many different length scales. Most of the kinetic energy of the turbulent motion is contained in the large scale

structures. The energy "cascades" from these large scale structures to smaller scale structures by an inertial and essentially inviscid mechanism. This process continues, creating smaller and smaller structures which produces a hierarchy of eddies. Eventually this process creates structures that are small enough that molecular diffusion becomes important and viscous dissipation of energy finally takes place.

*2.2.2.2 Approaches*

Time-dependent solutions of the Navier-Stokes equations for high Reynolds number turbulent flows in complex geometries which set out to resolve all the way down to the smallest scales of the motions are unlikely to be attainable for some time to come. Two alternative methods can be employed to render the Navier-Stokes equations tractable so that the small-scale turbulent fluctuations do not have to be directly simulated:

- *The Realizable $k - \varepsilon$ Model*

The simplest complete models of turbulence are the two-equation models in which the solution of two separate transport equations allows the turbulent velocity and length scales to be independently determined. The standard $k - \varepsilon$ model in ANSYS FLUENT falls within this class of models and has become the workhorse of practical engineering flow calculations in the time since it was proposed by Launder and Spalding [25]. Robustness, economy, and reasonable accuracy for a wide range of turbulent flows explain its popularity in industrial flow simulations. It is a semi-empirical model, and the derivation of the model equations relies on phenomenological considerations and empiricism.

As the strengths and weaknesses of the standard $k - \varepsilon$ model have become known, improvements have been made to the model to improve its performance. Two of these variants are available in ANSYS FLUENT: the realizable $k - \varepsilon$ model [26]. The $k - \varepsilon$ model is a semi-empirical model based on model transport equations for the turbulence kinetic energy $(k)$ and its dissipation rate $(\varepsilon)$. The model transport

equation for $k$ is derived from the exact equation, while the model transport equation for $\varepsilon$ was obtained using physical reasoning and bears little resemblance to its mathematical exact counterpart.

The realizable $k - \varepsilon$ model is a relatively recent development and differs from the standard $k - \varepsilon$ model in two important ways:

- The realizable $k - \varepsilon$ model contains a new formulation for the turbulent viscosity.
- A new transport equation for the dissipation rate, $\varepsilon$, has been derived from an exact equation for the transport of the mean-square vorticity fluctuation.

The term "realizable" means that the model satisfies certain mathematical constraints on the Reynolds stresses, consistent with the physics of turbulent flows. The standard $k - \varepsilon$ model is not realizable. An immediate benefit of the realizable $k - \varepsilon$ model is that it more accurately predicts the spreading rate of both planar and round jets. It is also likely to provide superior performance for flow involving rotation, boundary layers under strong adverse pressure gradients, separation, and recirculation. The realizable $k - \varepsilon$ model has shown substantial improvements over the standard $k - \varepsilon$ model where the flow features include strong streamline curvature, vortices and rotation.

One limitation of the realizable $k - \varepsilon$ model is that it produces non-physical turbulent viscosities in situations when the computational domain contains both rotating and stationary fluid zones, which is not applied in this study.

- *Large Eddy Simulation Method*

Large Eddy Simulation (LES) provides an alternative approach in which large eddies are explicitly computed in a time-dependent simulation using the "filtered" Navier-Stokes equations. The rationale behind LES is that by modeling less of turbulence, the error introduced by turbulence modeling can be reduced. It is also believed to be easier to find a universal model for the small scales, since they tend to

be more isotropic and less affected by the macroscopic features like boundary conditions, than the large eddies. Filtering is essentially a mathematical manipulation of the exact Navier-Stokes equations to remove the eddies that smaller than the size of the filter, which is usually taken as the mesh size when spatial filtering is employed as in ANSYS FLUENT. The filtering process creates additional unknown terms that must be modeled to achieve closure.

LES for high Reynolds number flows requires a significant amount of computational resources. This is mainly because of the need to accurately resolve the turbulent eddies in both space and time domains, which becomes most acute in near-wall regions where the scales to be resolved become much smaller. Wall functions in combination with a coarse near wall mesh can be employed to reduce the cost of LES for wall-bounded flows. However, the ramification of using wall functions for the flow needs to be considered carefully, and LES also requires highly accurate spatial and temporal discretizations.

In LES, large eddies are resolved directly, while small eddies are modeled. The rationale behind LES can be summarized as follows:

- Momentum, mass, energy, and other passive scalars are transported mostly by large eddies.
- Large eddies are more problem-dependent. They are dictated by the geometries and boundary conditions of the flow involved.
- Small eddies are less dependent the geometry, tend to be more isotropic, and are consequently more universal.
- The chance of finding a universal turbulence model is much higher for small eddies.

Resolving only the large eddies allows one to use much coarse mesh and large time step sizes in LES and LES still requires substantially fine meshes. In addition, LES has to be run for sufficiently long flow-time to obtain stable statistics of the flow being modeled.

## 2.3 Flow Over a Blockage Channel

The particles distribution in laminar flows has many applications in engineering biological and environmental systems [27]. The deposition of aerosols particles in channels and pipes, as well as in bends and contractions, is important in many applications, including dust inhalation and human respiratory systems, chip fabrication, particle size characterization and sampling of radioactive aerosols. In coal combustion systems and coal liquefaction-gasification pipelines, the erosion of material by solid particle impact is an important problem. In order to gain a fundamental understanding of the particle impaction and deposition phenomena, as well as to make meaningful design improvements. In the recent studies, analytical and experimental techniques are used to predict the particle deposition over some obstructions placed in the flow. One of the earliest papers in numerical simulation of two-dimensional Navier-Stokes flows within a channel was developed by Kawaguti [28] in 1961. In this work, the author used a finite difference approximation of the vorticity-stream function formulation of the steady equations of motions. His observations included the downstream drift of the primary vortex center with the increase of Re. Bowen et al. [29] used a theoretical approach to approximate the deposition of colloidal particles onto the walls of rectangular and cylindrical channels for fully developed laminar flows. Stratmann et al. [30] numerically modeled the deposition of small particles onto a flat plate in a stagnation flow to mimic the contamination of water surfaces in the electronics industry. Vatistas, Vasăk and Konstandopoulos [31-33] studied the phenomena of particle deposition on channel walls in different flow conditions; they investigated numerically and experimentally the vortex shredding behind two dimensional cylinders in a confined flow. For example, Vasak et al. [32] used fine silica and polystyrene particles in a channel in which the particles and channel wall were given opposite charges. A numerical study by Davis [34] of vortex shredding from rectangles in infinite domains is extended to include the effects of confining walls. An additional of a direct solver for the pressure equation was applied to solve with Reynolds number, blockage ratio and upstream velocity profile. Several experimental [35] and numerical [36, 37] investigations have

also introduced the phenomena of particle dispersion in shear flows whose dynamics and mixing characteristics are dominated by large-scale vortex structures.

The particle dispersion in such flows was found to be characterized by the Stokes number ( $St$ ), and defined as the ratio of particle response time ( $t_p$ ) to a characteristic flow time ( $t_f$ ). The flow time was defined by the dominant frequency associated with the vortex structures. Based on the steady-state Stokes drag law the particle response time was defined as $t_p = \rho_p d_p^2 / 18\mu$, where $\rho_p$ is the particle density $\left( kg / m^3 \right)$, $d_p$ the particle diameter $\left( m \right)$, and $\mu$ the gas viscosity $\left( Pa.s \right)$. Both experimental and numerical studies have shown that the presence of large vortex structures lead to a size-selective dispersion behavior such that the particles with Stokes number near unity ($St \sim 1.0$) exhibit maximum dispersion, while small particles (small Stokes number) get caught in the vortical structures and large particles (large Stokes number) pass through them.

The present study is to numerically simulate and analyze particle transport in an unsteady particle laden flow over a square cylinder placed in channel. The presence of the cylinder creates an unsteady or periodic flow field characterized by the presence of shredding vortices and recirculation in the fluid-wake region of the cylinder. In addition, the flow contains a stagnation region in front of the cylinder, as well as regions of flow acceleration and deceleration around it. The complexity of the flow and particle streams can be taken into consideration for the study of flow in human nasal cavity and respiratory system due to the blockage inside.

## 2.4 Flow in Human Nasal Cavity

### 2.4.1 Human Nasal Cavity Anatomy

The human nasal cavity is an important component to the respiratory system, which performs a variety of physiological functions. It is responsible for heating and humidifying inspired air to near body core temperature with full saturation, filters the

air from pollutants and toxic particles, and provides the sense of smell through olfactory recesses. Externally the nose consists of the triangular-shaped projection in the center of the face divided into two cavities (fossae) by cartilage called the septum. This forms a curved wall internally on the medial sides of each cavity. The axial length of the nasal passage between the external and internal openings is about 10 cm in adults [38]. The framework of the nostrils is made of cartilage, while the nasal septum, which separates the nostrils in the midline, is part bone closer to the skull and part cartilage at the outer tip (Fig. 2.2).
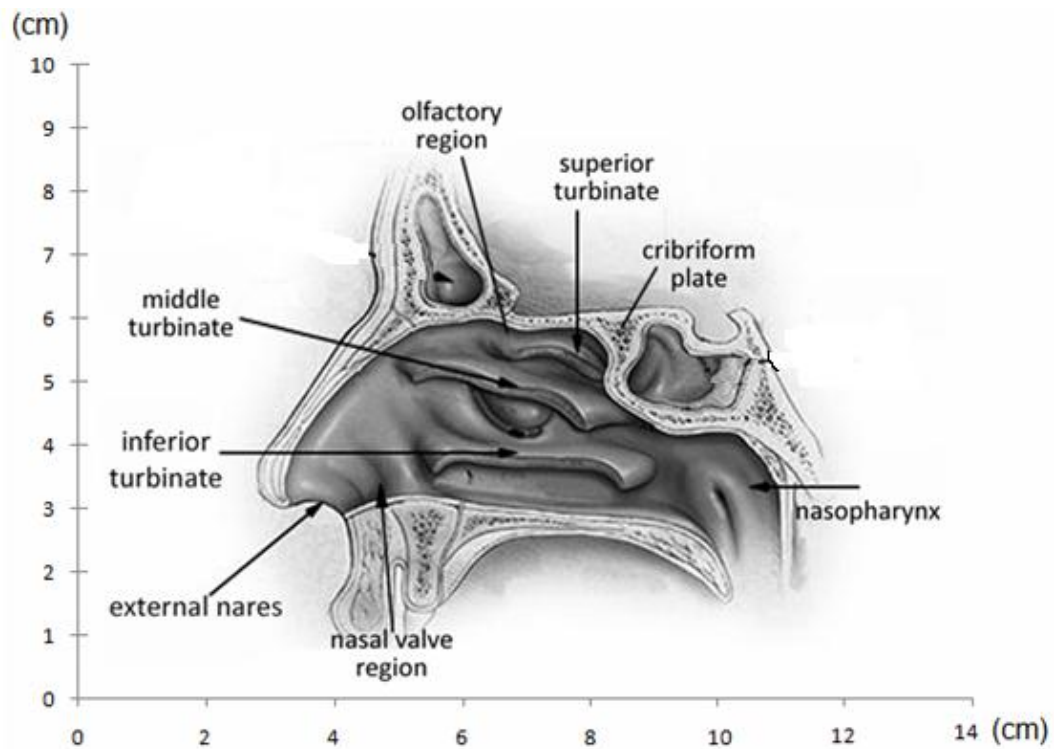


Figure 2.2: Nasal cavity anatomy: adapted from the Gray's anatomy of the human body, originally published in 1918 [39]

The clearance mechanism of deposited particles in this region is thought to occur by physical means such as sneezing, wiping, and blowing [40], which lead to a slower clearance than in the ciliated epithelium region. At the upper region of the main nasal passage where the nasal roof is, a slit-shaped airway is contained between the superior turbinate and the septum which is the olfactory region. The sense of smell is provided by the olfactory nerves which trap odor bearing particles for olfaction. The olfactory recesses are located at the superior most portion of the nasal cavity, medial to the paired superior turbinates. Olfactory nerves are found on the superior portion of the

septum, superior turbinates, and cribriform region. The width of the olfactory airway from the lateral to medial sides is 1-2 mm. The surface area of the olfactory epithelium varies somewhat from person to person, and values between 2 and 10 cm$^2$ have been reported for adults [41, 42].

Air enters the nose through external openings in the vestibule. The openings are called the nares or nostrils, and measure about 1.5 cm anteroposteriorly while at the back of the nose is the choanae (internal nares) measuring 2.5 cm vertically and 1.5 cm transversely which are the openings into the nasopharynx [38]. The vestibule of the nose is the visible rounded part that contains the external nares. It is lined with a stratified squamous epithelium that is moderately keratinized, and contains a highly variable mesh of hair projecting into the air-stream [43, 44]. The airway is largest at the nares and narrows inwards in a funnel like shape as it approaches the main entrance to the nasal passage. This entrance region is known as the nasal valve.

Human nose is an important part of the respiratory system performing a variety of physiological functions. The human nasal cavities do filter, warm and humidify air [39]. Drug deposition onto these turbinates can potentially treat health problems and can be used as an alternative injection of medicine [45]. Human nasal cavity contains three turbinates and is made of cartilage. It is expensive and difficult to perform experiments on the human nasal cavity as MRI and CT are involved, even if experiments were conducted on the hypothetical nasal cavity. CFD is a better option which provides better understanding of the flow inside the nasal cavity and deposition of the drug particle. Also the hypothetical nasal test experiments can be used to validate the CFD models.

The nasal septum separates the nostrils in the middle, is part bone closer to the skull and part cartilage at the outer tip (Fig. 2.2). The axial length of the nasal passage between the nasal valve region entry to nasopharaynx (Fig. 2.2) is about 8 cm [39]. The nasal valve region is also referred to as the internal valve and is the region where the lower edge of the upper lateral cartilage is attached to the septum, forming an angle of approximately 10-15° [46]. The nasal valve and the vestibule collapse at high flow rates caused by the increased pressure gradient between ambient and inhaled air.

During quiet breathing, however, the dimensions of the nasal cavity are constant. The olfactory region contains 3 paired turbinates: superior, middle and inferior. The inferior turbinate is the largest, spanning nearly the entire length of the main nasal passage; the middle turbinate is almost as big while the superior turbinate is half size of middle turbinate. Air enters the nose through external nares in the vestibule. The openings are called the nares or nostrils [47], measured about 1.5 cm in front of cribriform plate (Fig. 2.2).

## 2.4.2 Previous Research

Nasal airflow has been studied by a number of researchers. Early investigations of airflow were performed by Swift and Proctor [48]. Swift [49] studied droplet deposition for droplet diameters of 1.40 μm and flow rate of 7.50 L/min, respectively. Guilmette [50] examined inertial depositions in a nasal replica for droplet size of 0.60 to 12 μm and flow rate of 10 to 40 L/min. Zwartz and Guilmette [51] constructed another replica of the human nasal cavity who used 5.50 μm droplets and flow rates ranging from 10 to 40 L/min. Hauermann [52] investigated the differences in total deposition for 1.70-10 μm droplet. Cheng [53] summarized the droplet deposition, including both nasal and oral airways. Croce et al. [54] measured and simulated pressure-flow relationships for both nasal cavities. Numerical inspiratory airflow simulations were performed by Croce et al. [54] for flow rate ranged from 6.54 - 21.18 L/min in both the nostrils using CFD software FLUENT (Ansys Inc., USA). An early study was performed by Keyhani *et al.* [55] using a finite element mesh based on the experimental model used by Hahn *et al.* [56]. In all these research, nothing was conclusive regarding the collection of droplet.

Lippman et al. [57] discussed three main mechanisms for deposition of inhaled drug particles: inertial impaction, gravitational sedimentation, and Brownian diffusion. Only particle smaller than 1 $\mu m$ will deposit by Brownian diffusion [58], meanwhile in micro range, specifically particle greater than 1 $\mu m$, the effects of particle inertia become important and deposition by inertial impaction becomes dominant. The inertial parameter, $I = d_{ae}^2 Q$, where $d_{ae}$ is the aerodynamic equivalent

diameter in microns and $Q$ is the flowrate in cm$^3$/sec [57]. This is a measure to determine the significance of inertia.

Detailed air flow patterns can provide data that is pertinent to the prediction of gas-particle flows and regional tissue exposure to inhaled air. The nasal anatomy, characterized by thin airway channels does not allow direct measurements of flow patterns inside the human nose. Instead rigid cast models have been used to experimentally study the airflow patterns by a number of researchers. Early investigations of airflow were performed by Swift and Proctor [59], which provided the first quantitative in vitro velocity measurements. The results showed that the majority of flow passed through the middle airway with a small fraction of the flow separated upward, forming a standing eddy in the olfactory area. The flow was found to be laminar at a flow rate of 125 ml/s. Turbulent flow was detected downstream of the nasal valve at a flow rate of 208 ml/s.

There are three motivations for this study. First, a detailed flow structure is modeled to increase the drug delivery. Second, there was no conclusive result on the effect of particle size which will be revealed more in this research. Third, there is lack of real nasal cavity modeling. In this part, a realistic human nasal cavity was obtained to investigate the above motivations. Few assumptions were made in this research. First, a human nasal cavity consists of two identical mirrored cavities, so that the flow modeling and particle deposition investigation can be performed on one side and assumed identical result with the other side to save computational costs. Second, once the particle touches the wall of nasal cavity, it is stuck there and considered as collected.

## 2.5 Flow in Double Bifurcation

The trachea is a cylindrical tube with 10 to 12 cm long, about half of which is extrathoracic and half intrathoracic. According to Weibel's [60] measurement, the diameter of the trachea is about 1.5 to 1.8 centimeters. 16 to 20 incomplete (C-shaped) rings of cartilage composed the trachea wall with fibrous and muscular tissue.

The trachea divides into the two primary bronchi at the level of the fifth thoracic vertebra. There is an internal cartilaginous ridge at the point of bifurcation, called the carina. The right bronchus is a shorter, wider tube than the left and the angle of branching from the trachea is only 20-30˚. Weibel [60] measured the main bronchus to be 0.9 to 1.5 cm in diameter and 4 to 6 cm in length. Consequently any foreign bodies that enter the trachea are more likely to be inhaled into the right main bronchus. This may also influence the distribution of aerosol delivery to the lungs.

Initial research conducted on the physics of aerosols and airflow in the human upper airway has been mainly based on experimental and theoretical studies. The velocity profile and deposition efficiency had been the focus of previous studies. The experimental approach had been used to obtain either velocity profile or deposition efficiency. Generally, experimental studies can be categorized into two major approaches, using human cadaver replicate airway models to study deposition efficiency and idealized airway models (e.g. made of smooth plastic tubes) to study velocity profile using pressure probe or dye tracing. Due to the nature of the complex setup involved in the experimental study, these two issues were often investigated separately and the interaction between fluid (airflow) and particles (aerosols) was rarely explored in experimental studies. Many of these in vitro experiments although provided important information, limitations were unavoidable. From a velocity profile perspective, the method of inserting the probe into a model to measure the flow can often affect the flow downstream and the measurement point [61]. This is especially noticeable when the cross-section of the airway tube was small. Moreover, only limited sample readings were extracted due to the cost and time in the experimental setup. Thus, the amount of information provided by experimental technique is not only restricted, but the accuracy of the results can be difficult to control. The more advanced method of using laser Doppler anemometry have been applied recently in more recent research [62, 63]. This has resulted in improved accuracy for velocity profiles along occluded tubes without influencing the flow inside. However, a disadvantage of this method still exists. Despite the costly equipment, the complexity in preparing the equipment and the long process time in acquiring and standardizing the results remain unavoidable. Also, some crucial information, such as the boundary

layer region (near wall region) of flow velocity, is extremely difficult to capture in which this factor is one of the major influences in particle deposition on the wall of the model. In terms of measuring deposition efficiency, there are two major approaches. Zhou and Cheng [64] introduced one of the methods which involved injecting a range of polystyrene latex fluorescent particles into a hollow silicone rubber cast of human airways, and then the cast was cut into segments. Fluorescent material in the particles that deposited in the cast was extracted using ethyl acetate. The resultant solution was then filtered using a nylon membrane and the fluorescence content of the filtered solution is measured using a florescence spectrometer. The deposition efficiency in each airway segment is calculated from this measurement. Another method (Schlesinger et al. [65]) was to inject ferric oxide particle tagged with short-lived radio isotopic tag, then deposition activities within the cast were measured in a scintillation detector system. Similarly, these experimental techniques required expensive equipments and extensive time of setup. The major disadvantage in this type of approach was that the casts of the airway were replicated from a cadaver in which the shape and the angle of bifurcation of the airway were very likely to be distorted compared to living human subject after the airway was taken out from a cadaver. The loss of geometrical details can also happen during the replication process. Another limitation was also declared by Schlesinger et al. [66] where the large number of bronchi within the cast and limitations imposed by use of a short-lived isotope tag made a complete investigation of deposition within all branches of the cast impractical. Measurements were, therefore, made within a selected sample of bronchi.

The study of air flow fields and particle deposition in tracheobronchial airways are very important for investigating the risks of air pollutants and determining drug-aerosol delivery inside the lung tissues [9]. The intention of improving the delivery of aerosol drug in the lung cavity needs the understanding of aerosol transport mechanisms in tissue. However, it is impossible to clearly measure the aerosol particles deposition in human lung experimentally, thus computational fluid dynamics (CFD) is a better solution to this problem provided the model is validated. Over the

last decades, a number of studies of flow simulation and particles deposition in human airway have been conducted in CFD.

Inhaled particle pollutants can be considered as a potential cause of respiratory diseases [67-69]. In addition, currently marketed inhalation therapies can only deliver 10-20% of a drug load into the lung with an effective inhalation [70] and Roland el al. [71] reviewed that the extra drug load 80-90%, the rest of the drug) for certain types of drug can cause side effects to patient. Understanding the distribution of inhaled aerosols in the human airways is very important in asthma treatment and also to improve risk assessments of ambient contaminants [72]. Accurate prediction of local and regional pattern of inhaled particle deposition in the human airway should provide useful information to clinical researchers in assessing the pathogenic potential and possibly lead to innovation in inhalation therapies. Many researchers have investigated the fluid dynamics in the lower bifurcation airways to characterize the particles behavior related to aerosol particles [1, 10, 13, 73]. Nowak [74] conducted CFD simulations of airflow and particle deposition in geometries representing the human tracheobronchial tree. Van Ertbruggen *et al.* [75] studied gas flow and particle deposition in a realistic three-dimension of the bronchial tree, extending from the trachea to the segmental bronchi using CFD; it is explained in detail that particle deposition efficiency increases with particle size and is minimal for $\approx 12 L/\min$ $\left(\text{Re} \approx 2000\right)$ inspiratory flow. Weibel [60] introduced the structure of human bronchial airways as a repeatedly bifurcating tubes network with significant decreasing of sizes and flowrates.

The human inhalation flow rate in trachea was studied from light breathing (10 L/min) to heavy breathing (100 L/min) [10]. Nielsen [76] studied the Diskus™ (Accuhaler™; Glaxo Wellcome, UK) inhaler delivering a consistently fine particle dose of salmeterol used with the size ranging from $1\,\mu m$ to $6\,\mu m$ at flow rates of 28 and 60 L/min. Kim & Fisher [14] conducted experiment with double bifurcation tube models with two different branching geometries: one with in-plane and another with $90°$ out-of-plane bifurcation to study deposition efficiencies and deposition patterns of aerosol particles. Weibel's symmetric model A has been widely utilized by

investigators of human airway study. The model was developed by Weibel in 1963 based on the measurement on the major conducting airway branches from a plastic cast of a pair of human lungs. Weibel analyzed and found the correlation on diameter and length of branches as well as distribution correlations of diameter and length in every generation. Although only first four generations and 10% of the rest of the generation were measured precisely, due to the difficulty in measuring the small bronchioles, regular dichotomy and a mean branch length to diameter ratio were assumed and from these measured data, Weibel's symmetric model A with regular dichotomy and fixed length to diameter ratio was developed.

The trachea is designated as generation 0 and every three subsequent generations are called "unit 1", "unit 2", "unit 3", and so on. The separating edges between two continuous generations were called "carina ridges", and in this study it is assumed to be sharp. With the assumption of identical tissue size in same generation, the velocity magnitude of each tissue can be calculated since the flow volumetric magnitude of each tissue is twice that of the subsequent generation. The velocity field in generation 3 from unit 1 is used as the inlet velocity for unit 2, and the whole process is repeated. It is very important to identify the relationship between velocity profiles of adjacent generation, since Comer *et al.* [10] showed that after first bifurcation, the flow becomes quite complex and significant number of vortices appeared.

It is assumed that a symmetrical Weibel planar model is used in this study due to user-friendly and generally comparable characteristics [9, 10, 13]. The geometry is found as generation 3, 4 and 5 employing Weibel's lung scheme [60] as shown in Fig. 2.3. All diameters are in centimeters.
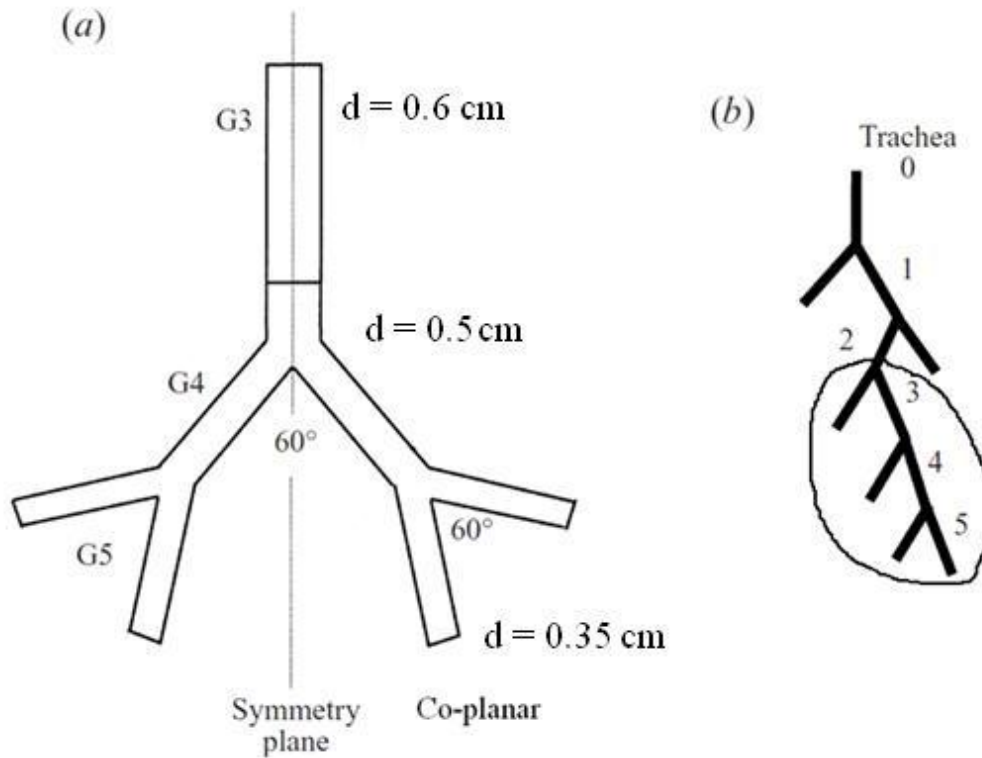
Figure 2.3: Double bifurcation geometry: (a) schematics of generations 3, 4 and 5; (b) Weibel's lung classification model

Past analysis showed that there are 10000 – 15000 elements of lung tissues would be required to successful simulate of the entire geometry containing 107 branches of the lung [74]. The required memory to simulate such a structure is estimated excess 200 GB of RAM. Therefore, it is decided to perform the simulation on a small section of the airways, 3.5 generations of Weibel human lungs model from generation 3 to generation 5 in this research.

## 2.6 Grid Independence Test

In preparation of simulations, geometry has to be meshed by meshing software. In this research, ANSYS FLUENT GAMBIT (ver. 2.4.6) was employed to perform meshing procedure. The computational mesh topology hierarchy used in GAMBIT [77] includes: vertex, line, face and volume as shown in Fig. 2.4.

vertex points  lines  faces  volumes

Lowest topology ⎯⎯⎯⎯⎯⎯⎯⎯⎯⎯⎯⎯⎯⎯→ Highest topology
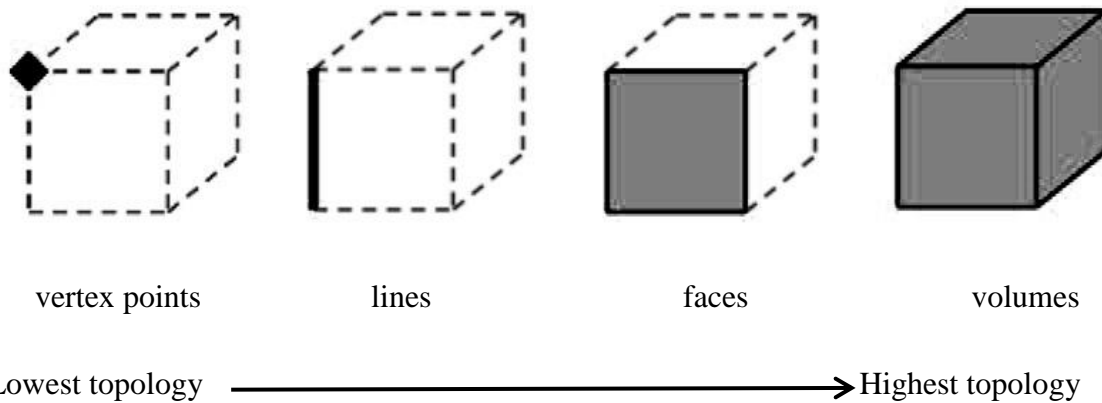
Figure 2.4: Mesh topology used in GAMBIT

A higher topology assumes the existence of the topologies underneath it (Fig. 2.4). For example, the creation of volume cell automatically inherits the lower topologies (i.e. a volume cell contains faces, face contains lines and line contains vertex structures). For a complex geometry such as the nasal cavity, double bifurcation, an unstructured mesh was used as it is very time consuming if not impossible to achieve as a structured mesh. Unstructured meshes may involve the use of hexahedral, tetrahedral, pyramid, and wedge cells (Fig. 2.5) in combination, whereas a structured mesh is more reliant on hexahedral cells or the use of block-structured grids [77].



Tetrahedron  Hexahedron

Prism/Wedge  Pyramid
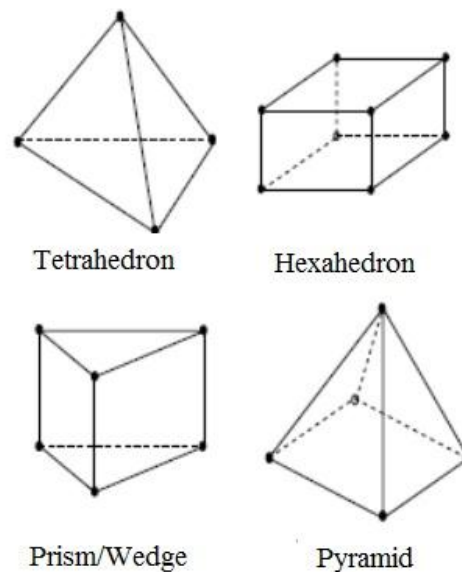
Figure 2.5: Three dimensional unstructured mesh cell types

## 2.7 Numerical Solver Procedures

The equations given in Chapter 3 are converted into their corresponding integral form which is a requirement for control volume based CFD solvers such as FLUENT. The domain is then discretized into control volumes based on the designed mesh. The governing equations are rearranged into an integral form to allow integration of the equations on each individual control volume cell within the mesh. A set of algebraic equations for dependent variables such as velocities, pressure and temperature are then set up and solved. The segregated solver within FLUENT was chosen which solved the governing equations sequentially. The flow chart of the procedure is shown in Fig. 2.6.
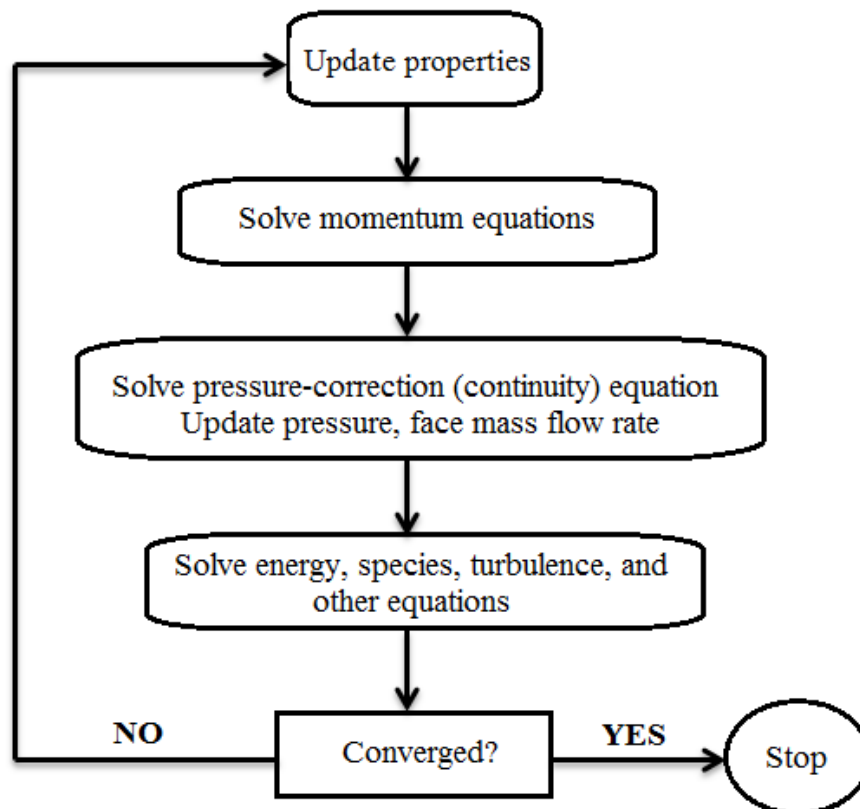


Figure 2.6: Flowchart of segregated solver solution steps

CHAPTER 3

METHODOLOGY

Based partly on the physical properties of pharmaceutical aerosols and partly on the mathematical modeling effort required, there are certain reasonable assumptions made to describe the pharmaceutical aerosol transport in a fluid medium as follows,

- *The pharmaceutical aerosol is assumed to be spherical*: This is reasonable assumption, especially for the liquid based inhaled pharmaceutical droplets, since the small liquid droplets are spherical.

- *The ratio of particle to fluid density is very large*: The density of pharmaceutical compounds is much higher when compared to the fluid medium which is air. Typically, the density of aerosols is $\sim 1550$ $kg/m^3$ as opposed to $\sim 1.2$ $kg/m^3$ for air breathed in.

- *Drag force is the dominant point force*: This is a direct result of the previous assumption. Since the density of the aerosols are much higher than the density of the fluid medium, several force such as the lift force, buoyancy force can be readily discarded as they have negligible effect on the aerosol transport.

**3.1 Governing Equations in Blocked Channel**

**3.1.1   Flow Equations**

In this study, air is considered as incompressible fluid, flows in y-direction along the channel. The equations governing the unsteady incompressible gas flow are the continuity equation (Eqn. 1) and Navier-Stokes equations (Eqn. 2, 3), which can be written in the nondimensional form as

$$\frac{\partial u}{\partial x} + \frac{\partial v}{\partial y} = 0 \tag{1}$$

$$\frac{\partial u}{\partial t} + u\frac{\partial u}{\partial x} + v\frac{\partial u}{\partial y} = -\frac{\partial p}{\partial x} + \frac{1}{Re}\left(\frac{\partial^2 u}{\partial x^2} + \frac{\partial^2 u}{\partial y^2}\right) \tag{2}$$

$$\frac{\partial v}{\partial t} + u\frac{\partial v}{\partial x} + v\frac{\partial v}{\partial y} = -\frac{\partial p}{\partial y} - Fr^{-2} + \frac{1}{Re}\left(\frac{\partial^2 v}{\partial x^2} + \frac{\partial^2 v}{\partial y^2}\right) \tag{3}$$

The governing equations were descretized using a control-volume approach with a staggered grid system [78], where $u, v$ are flow in $x, y$ direction, respectively, The numerical solution employs the marker-and-cell (MAC) methodology developed by Hirt et al. [79]. Here Re and $Fr$ (dimensionless) are the Reynolds and Froude numbers defined, respectively, as $Re = \frac{B.u_m}{v}$ and $Fr = \frac{u_m}{\sqrt{B.g}}$, where $g$ is the gravitational acceleration $(m/s^2)$, $v$ is the dynamic viscosity $(m^2/s)$ and $u_m$ is the velocity at the channel entrance $(m/s)$. The equations are normalized by using $B$ as the length scale $(m)$, $u_m$ as the velocity scale $(m/s)$ and $B/u_m$ as the time scale (dimensionless). At the channel exit, a continuous outflow condition is prescribed by setting $\frac{\partial u}{\partial y} = \frac{\partial v}{\partial y} = 0$. On walls of channel, as well as on the square cylinder boundaries, the fluid will have zero velocity relative to the boundaries. At the outflow boundary, owing to the extremely large integration domain behind the cylinder, no influence is expected for the solution in the vicinity of the cylinder.

The stream function, $\psi$ $(kg/s)$, is defined for two-dimensional flows of various kinds. One way to define the stream function $\psi$ for a two dimensional flow such that the flow velocity can be expressed as

$$U = \nabla \times \psi \tag{4}$$

where $\psi = (0,0,\psi)$ if the velocity vector $U = (u,v,0)$.

In fluid dynamics, vorticity is the curl of the fluid velocity. It can also be considered as the circulation per unit area at a point in a fluid flow field. It is a vector quantity whose direction is along the axis of the fluid's rotation. For a two-dimensional flow, the vorticity vector is perpendicular to the plane.

In Cartesian coordinates, the stream function can be found from vorticity using the following Poisson's equation:

$$\nabla^2 \psi = -\omega \qquad \text{or} \qquad \nabla^2 \psi' = +\omega \tag{5}$$

Where $\vec{\omega} = (0, 0, \omega)$ and $\vec{\omega} = \vec{\nabla} \times \vec{v}$.

### 3.1.2   Particle Governing Equations

Throughout this research, anthracite particle (coal-like) was employed as the injected particle. Due to the fact that anthracite dust can be found easily at the coalmine, the probability for coalminers in breath anthracite is very high, thus taking anthracite as particle type for this research is reasonable.  Injected particles under consideration traverse a complex transient flow field containing regions of stagnation flow, separating flow, recirculation, and vortex structures. By definition, the stream function in two-dimensional flows can be used to plot streamline, which represent the trajectories of particles in a steady flow and vorticity is the curl of velocity. Particles with prescribed Stokes numbers were injected in uniform distribution form at the inlet of the channel and their trajectories were calculated in the presence of gravity in reverse y-direction. A group of 40 anthracite particles with uniform size and equally distributed was injected at the entrance of channel at position right at the bottom of the cylinder (from $x/B = -1/2$ to $x/B = 1/2$) in Fig. 3.1. Consequently, a detailed particle dynamics model based on the modified Basset-Bousinesq-Oseen equation [80] is applied to calculate particles trajectories. The general equation of motion of a small spherical particle suspended in fluid is given as Basset-Bousinesq-Oseen equation is used to account for the high Reynolds number effects.

31

$$\frac{du_p}{dt} = C_A \frac{1}{2}\frac{1}{\varepsilon}\frac{d}{dt}(u-u_p) + \frac{1.2C_H}{(\varepsilon Stk)^{\frac{1}{2}}}\int_{t_0}^{t}\frac{d(u-u_p)/dt}{\sqrt{t-t^*}}dt^* + \frac{0.47}{(\varepsilon Stk)^{\frac{1}{2}}}\frac{d_{jk}(u-u_p)}{(d_{lm}d_{ml})^{\frac{1}{4}}} + C_{Ds}\frac{u-u_p}{Stk} + \left(1-\frac{1}{\varepsilon}\right)Fr^{-2}$$

$$\underbrace{\hspace{3cm}}_{1} \quad \underbrace{\hspace{1.5cm}}_{2} \quad \underbrace{\hspace{0.5cm}}_{3} \quad \underbrace{\hspace{0.5cm}}_{4}$$

(6)

The equation is written in a vector form where $u$ and $u_p$ represent, respectively, the gas and particle velocity vectors. The instantaneous particle location $x(t)$ is obtained from Eqn. (7)

$$\frac{dx}{dt} = u_p$$

(7)

Eqn. (6) and Eqn. (7) are normalized using $B$ and $u_m$ as the length and velocity scales, respectively. The terms on the right-hand side of Eqn. (6) represents the Basset history term (term 1), Saffman lift term (term 2), steady state drag (term 3), and gravity term (term 4), in that order, respectively. More detailed discussion of these terms can be found in Aggarwal, and Maxey [78, 81].

The nondimensional Basset-Bousinesq-Oseen Eqn. (6) highlights two key parameters, namely, the Stokes number ($St$) and the density ratio ($\varepsilon$). The density ratio ($\varepsilon$) is defined as $\varepsilon = \rho_p/\rho$ where particle density ($\rho_p$) and gas density ($\rho$). The Stokes number is defined as in Eqn. (8)

$$Stk = \frac{t_p}{t_f} = \frac{d_p^2 \varepsilon \, \mathrm{Re}}{18B^2}$$

(8)

where $d_p$ is particle diameter. $C_{Ds}$ in Eqn. (6) is a correction factor that accounts for the high Reynolds number effect on the steady state drag coefficient and is given by Eqn. (9)

$$C_{Ds} = 1 + \frac{\text{Re}_p^{2/3}}{6}$$

(9)

The particle Reynolds number is defined as $\text{Re}_p = u_p d_p \rho_p / \mu$, where $u_p$ is the magnitude of relative particle velocity. Further, $C_A$ and $C_H$ in Equation (6) are the correction factors accounting for the high Reynolds number effects in the added mass and Basset history terms. Following [78, 81, 82], $C_A$ and $C_H$ are expressed by Eqn. (10) and (11), respectively.

$$C_A = 1.05 - \frac{0.066}{A_C^2} + 0.12$$

(10)

$$C_H = 2.88 + \frac{3.12}{\left(1 + A_C\right)^3}$$

(11)

where $A_C$ is the relative acceleration factor defined by Eqn. (12)

$$A_C = \frac{v_r^2 / d_p}{dv_r / dt}$$

(12)

Finally, $d_k$ in the Saffman lift term is the deformation rate tensor defined by Eqn. (13)

$$d_k = \frac{\partial u}{\partial x_k}$$

(13)

### 3.1.3 Computational Model

A 2D laminar flow around a square cylinder with square side ($B$) is located centrally in a channel with height ($H$) and length ($L$) (Fig. 3.1). The blockage ratio was fixed at Br = 1/4. In order to reduce the influence of inflow and outflow boundary conditions, the length of the channel was set to $L/B$ =24. The cylinder is axially located 8B downstream of the channel inlet and an inlet flow condition is prescribed at the channel entrance.
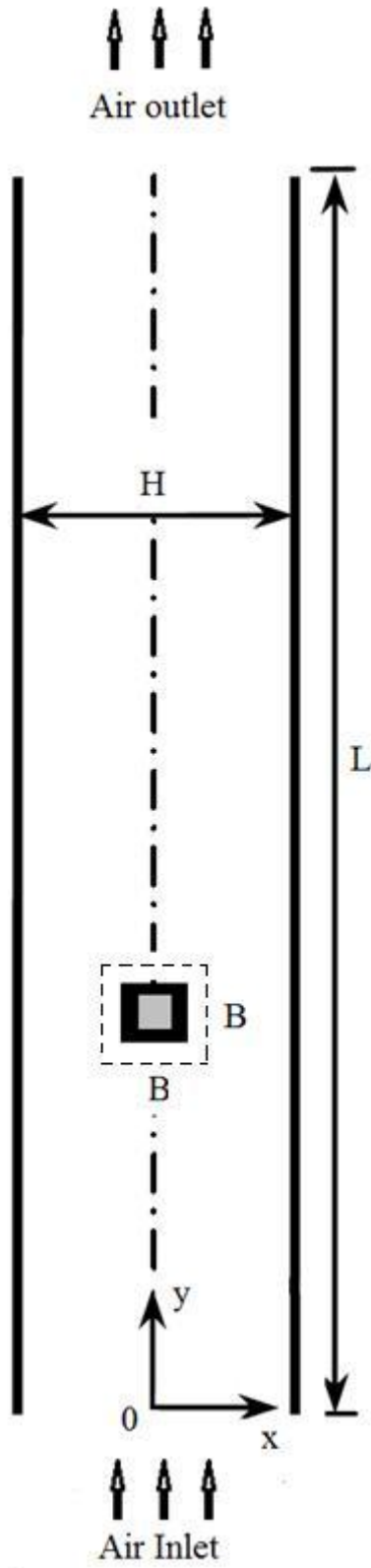
Figure 3.1: Physical domain of the square blockage in the channel

The channel with built-in square cylinder was modeled with two dimension geometry with the square cylinder cut through the channel. A channel with dimensions of 0.24 m long and width of 0.04 m, with a square cylinder of 0.01 m side, was introduced in this simulation. A structured mesh and the zoom-in area near the square cylinder area (surrounded by dotted lines in Fig. 3.1) were used as shown in Fig. 3.2. This mesh was extra-refined at the square cylinder area to give accurate results. The finest mesh contained total 486,400 quadrilateral elements and 488,100 nodes with 971,100 interior faces.
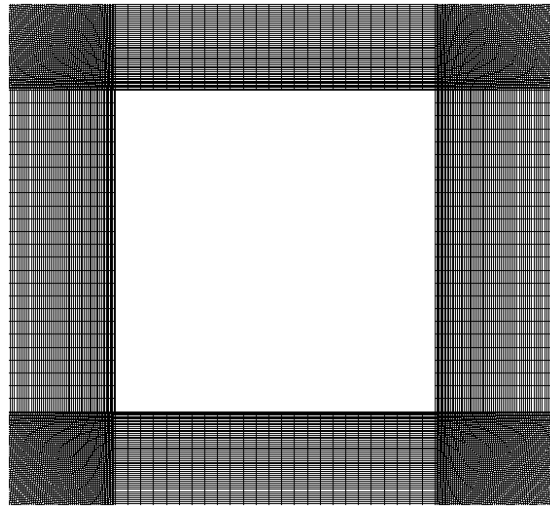


Figure 3.2: Refined mesh of the zoom-in area near the square cylinder

A list of major test cases studied in the current investigation is shown in the Table 3.1 with detailed Reynolds number, Stokes number (if available) and total flow time with time step size. Test case 1 and test case 4 are employed to study the mechanism of flow inside channel without injecting particles (indicated as N/A in Stokes number column). In test case 5, the "massless" indicates that the particle size used in the injection is extremely small.

Table 3.1: Table of the major test cases studied in the current investigation

| Test case ID | Mesh quality | Reynolds number (uniform inlet velocity) | Stokes number (particle diameter) | Total flow time (time step size) |
|---|---|---|---|---|
| Test case 1 | Refined mesh | 150 (0.055 m/s) | N/A | 25 sec (0.01sec) |
| Test case 2 | Refined mesh | 300 (0.1096 m/s) | 0.1 ($42.3\mu m$) | 25 sec (0.01sec) |
| Test case 3 | Refined mesh | 600 (0.22 m/s) | 0.1 ($30\mu m$) | 25 sec (0.01sec) |
| Test case 4 | Refined mesh | 900 (0.329 m/s) | N/A | 25 sec (0.01sec) |
| Test case 5 | Refined mesh | 1200 (0.45 m/s) | 0 (massless) | 25 sec (0.01sec) |
| Test case 6 | Refined mesh | 1200 (0.45 m/s) | 0.01 ($6.6\mu m$) | 25 sec (0.01sec) |
| Test case 7 | Refined mesh | 1200 (0.45 m/s) | 0.1 ($21\mu m$) | 25 sec (0.01sec) |
| Test case 8 | Refined mesh | 1200 (0.45 m/s) | 0.5 ($47\mu m$) | 25 sec (0.01sec) |
| Test case 9 | Refined mesh | 1200 (0.45 m/s) | 1.0 ($66\mu m$) | 25 sec (0.01sec) |
| Test case 10 | Refined mesh | 1200 (0.45 m/s) | 2.0 ($95\mu m$) | 25 sec (0.01sec) |

## 3.2 Governing Equations in Human Nasal Cavity

In order to investigate the flow dynamics and particle deposition in human nasal cavity for various in breath rates, several tests were performed with different inlet velocities. Light breathing rates (7.5 L/min and 15 L/min) were assigned to laminar flow and heavy breathing rates (30 L/min and 60 L/min) were assigned to turbulent flow. The solution is obtained using commercial CFD software ANSYS FLUENT (version 12.0.6) by solving the Navier-Stokes and continuity equations with appropriate boundary conditions.

### 3.2.1   Laminar Flow

In this study, air is considered as incompressible fluid. In steady state laminar incompressible flow in human airway, the continuity and momentum equations [77] with the absence of gravitational and external forces are given as in Eqn. (14) and Eqn. (15).

$$\nabla \cdot \left( \rho \vec{v} \right) = 0 \tag{14}$$

and

$$\nabla \cdot \left( \rho \vec{v} \vec{v} \right) = -\nabla p + \nabla \cdot \left( \overline{\overline{\tau}} \right) \tag{15}$$

where $p$ is the static pressure (Pa), $\overline{\overline{\tau}}$ is the stress tensor (Pa) given in Eqn. (16)

$$\overline{\overline{\tau}} = \mu \left[ \left( \nabla \vec{v} + \nabla \vec{v}^{T} \right) - \frac{2}{3} \nabla \cdot \vec{v} I \right] \tag{16}$$

where $\mu$ is molecular viscosity (Pa.s), $I$ is the unit tensor (dimensionless), and the second term on the right hand side is the effect of volume dilation.

### 3.2.2 Turbulent Flow

In turbulent case, the realizable $k-\varepsilon$ model was employed to solve the flow in nasal cavity (discussed in 2.1.2.2). The realizable $k-\varepsilon$ [77] is relatively recent development and differs from the standard $k-\varepsilon$ model in two important ways: the realizable $k-\varepsilon$ model contains a new formulation for the turbulent viscosity, and a new transport equation for the dissipation rate, $\varepsilon$, has been derived from an exact equation for the transport of the mean-square vorticity fluctuation. This model more accurately predicts the spreading rate of both planar and round jets. It is also likely to provide superior performance for flows involving recirculation.

The modeled transport equations [77] for $k$ and $\varepsilon$ in the realizable $k-\varepsilon$ are shown in Eqn. (17) and Eqn. (18)

$$\frac{\partial}{\partial x_j}\left(\rho k u_j\right) = \frac{\partial}{\partial x_j}\left[\left(\mu+\frac{\mu_t}{\sigma_k}\right)\frac{\partial k}{\partial x_j}\right] + G_k + G_b - \rho\varepsilon - Y_M + S_k \tag{17}$$

and

$$\frac{\partial}{\partial x_j}\left(\rho\varepsilon u_j\right) = \frac{\partial}{\partial x_j}\left[\left(\mu+\frac{\mu_t}{\sigma_\varepsilon}\right)\frac{\partial\varepsilon}{\partial x_j}\right] + \rho C_1 S_\varepsilon - \rho C_2 \frac{\varepsilon^2}{k+\sqrt{\upsilon\varepsilon}} + C_{1\varepsilon}\frac{\varepsilon}{k}C_{3\varepsilon}G_b + S_\varepsilon \tag{18}$$

In these equations, $C_1$ is the constant (dimensionless) is shown in Eqn. (19)

$$C_1 = \max\left[0.43, \frac{\eta}{\eta+5}\right] \tag{19}$$

where $\eta$ is the effectiveness factor (dimensionless) is shown in Eqn. (20)

$$\eta = S\frac{k}{\varepsilon} \tag{20}$$

where $G_k$ represents the generation of turbulence kinetic energy due to the mean velocity gradients is shown in Eqn. (21)

$$G_k = \mu_t S^2 \tag{21}$$

$S$ is the modulus of the mean rate-of-strain tensor is shown in Eqn. (22)

$$S = \sqrt{2 S_{ij} S_{ij}} \tag{22}$$

$G_b$ is the generation of turbulence due to buoyancy (zero in this case) is shown in Eqn. (23)

$$G_b = \beta g_i \frac{\mu_t}{\mathrm{Pr}_t} \frac{\partial T}{\partial x_i} \tag{23}$$

where $\mathrm{Pr}_t$ is the turbulent Prandtl number for energy (dimensionless) and $g_i$ is the component of the gravitational vector in the $i$th direction ($m/s^2$). $Y_M$ represents the contribution of the fluctuating dilatation in compressible turbulence to the overall dissipation rate, $Y_M = 2\rho \varepsilon M_t^2 \left( kg/m.s^3 \right)$, where $M_t = \sqrt{\dfrac{k}{a^2}}$ is the Mach number (dimensionless), $a \equiv \sqrt{\gamma R T}$ is the speed of sound ($m/s$). $C_2 = 1.9$ and $C_{1\varepsilon} = 1.44$ are constant (dimensionless). $\sigma_k = 1.0$ and $\sigma_\varepsilon = 1.2$ are the turbulent Prandtl numbers for $k$ and $\varepsilon$ (dimensionless), respectively. $S_k$ and $S_\varepsilon$ are user-defined source terms (dimensionless) (zero in this case).

### 3.2.3   Particle Governing Equations

Based on Stokes' law, gravity force, $\vec{F}_{grav}$, and drag force, $\vec{F}_{drag}$, are the only forces acting on the particle as shown in Eqn. (24). Brownian force is negligible since all the particles sizes injected greater than $1\ \mu m$.

$$\vec{F} = \vec{F}_{drag} + \vec{F}_{grav} \quad \text{or} \quad \frac{du_p}{dt} = F_d \left( u - u_p \right) + g_i \left( \rho_p - \rho \right)/\rho_p \tag{24}$$

where $u$ is the fluid velocity $(m/s)$ and $u_p$ is the particle velocity $(m/s)$, $g_i = 9.81(m/s^2)$ taken in the y-axis, $F_d(u-u_p)$ is the drag force per unit mass and $F_d$ is given in Eqn. (25)

$$F_d = \frac{18\mu}{\rho_p d_p^2} \frac{C_D \, \text{Re}}{24} \tag{25}$$

where $\mu$ is the fluid viscosity $(Pa.s)$, $\rho$ is the fluid density $(kg/m^3)$, $\rho_p$ is the particle density $(kg/m^3)$ and $d_p$ is the particle diameter $(m)$. With assumption all the particles are in spherical shape, the drag coefficient, $C_D$ (dimensionless), is defined as

$$C_D = \begin{cases} \dfrac{24}{\text{Re}}\left(1+\dfrac{1}{6}\text{Re}^{2/3}\right) & \text{Re} \leq 1000 \\ 0.424 & \text{Re} > 1000 \end{cases} \tag{26}$$

### 3.2.4 Nasal Cavity Reconstruction Methods

*3.2.4.1 Geometry*

Generally, there are three common methods to investigate gas and gas- particle in human nasal cavity: i) testing on human lungs, ii) replicate casts, iii) numerical CFD simulations [12]. Due to the lack of resources and health risks to volunteers, and meanwhile CFD method has repeatability, opportunity to have a controlled flow, and offers a quick solution with details; it is decided to study the gas flow and particle deposition in human nasal cavity numerically.

The procedure of reconstructing a human nasal cavity model can be described in four steps: image acquisition, data conversion, segmentation and reconstruction (Fig. 3.3) in following sections.
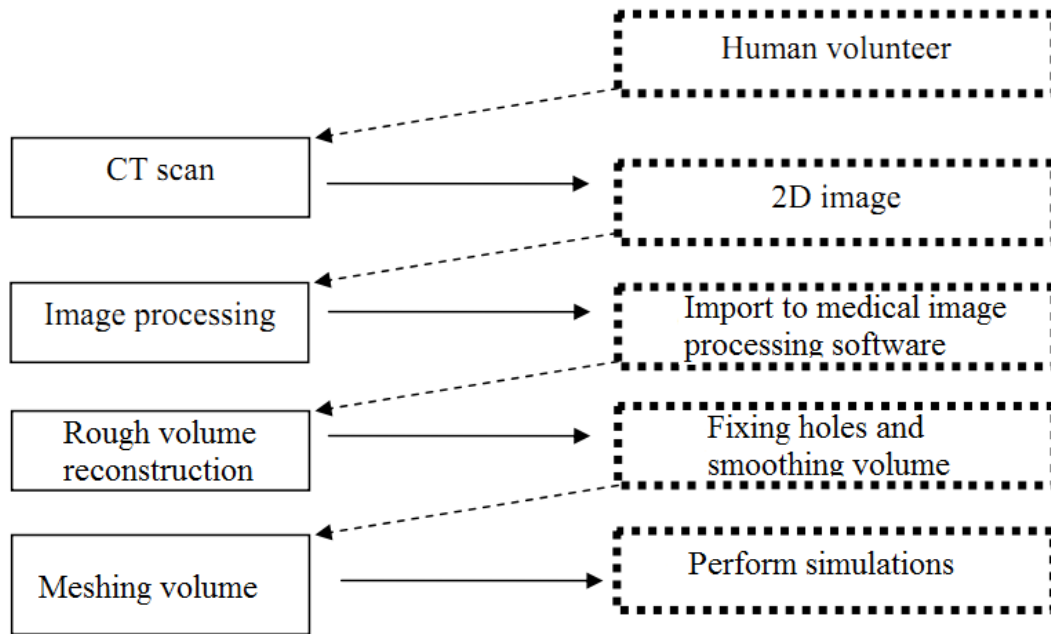
Figure 3.3: Procedure of human nasal cavity geometry reconstruction

The development of a computational model of the human nasal cavity begins firstly with medical imaging taken from the human volunteer. Medical images can be obtained from various sources, yet all provide essentially similar information: a 3D matrix (or series of 2D matrices) of volume elements (voxels), in which tissues and structures are distinguished from one another by differences in brightness or grey-scale. Visualization and reconstruction of morphological structures contained within these images is an area of active research. Computed tomography (CT) is the combination of mechanical and computer engineering which was first developed in 1972. During a typical CT procedure, the patient is placed on a table. The table then moves the patient through the gantry (a donut-shaped device), which houses an X-ray tube and detector array. For each image acquired, the X-ray tube rotates around the patient and the X-rays pass through the patient to the detector array, and thousands of X-ray measurements are acquired. The computer then processes this information and displays the corresponding images on a computer screen. This imaging technique avoids any superimposition of organs or tissues upon one another that might occur during other types of X-ray tomographic studies. The CT exam creates images analogous to a single slice of bread from a whole loaf or a slice from an orange. Hence, the word 'slice' is often used to describe a view of patient anatomy. Each CT

image consists of large number of small picture elements (pixels). Each pixel is assigned a numerical value (gray scale), based on the degree to which the tissue corresponding to that pixel attenuates the X-Ray beam. In this research, a nasal cavity geometry was obtained through CT scans of the nose (Fig. 3.4) from a shared source online. The scans captured outlined slices in the x-y plane at different positions along the z axis from the entrance of the nasal cavity to just anterior of the larynx at interval of 1 mm.
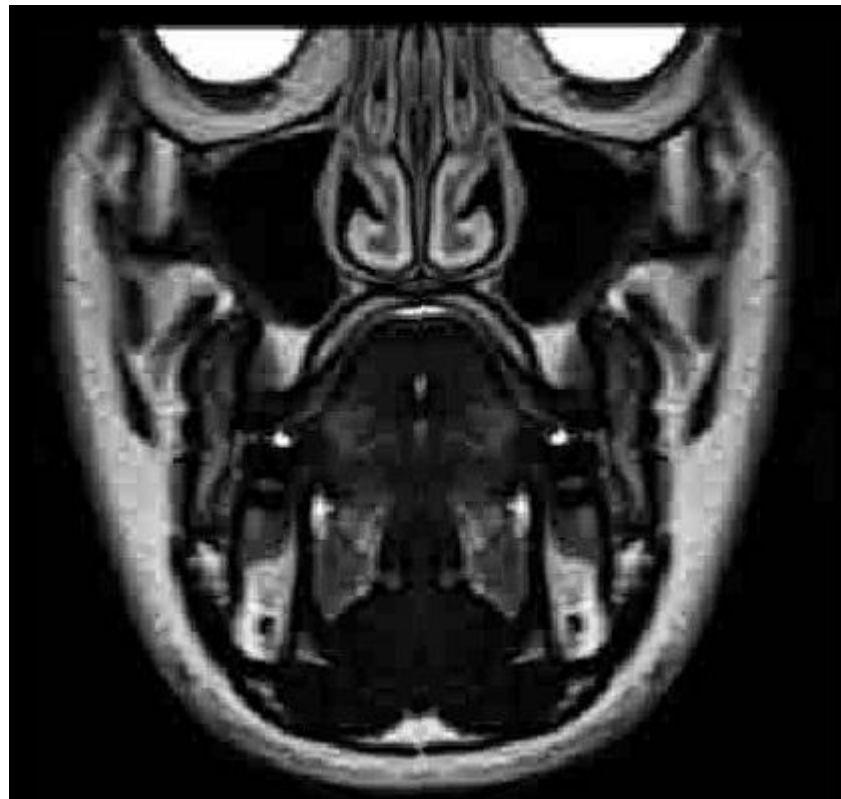


Figure 3.4 CT scan of the middle turbinate region (Source: www.imaios.com)

The data obtained from 2D CT scan was a series of cross sectional images which contains different gray scale information with respect to different organs or tissues. The original set of CT images is converted into a file format compatible with the software 3D Doctor®, a 3D imaging software that generates and modifies surface 3D models from stacked medical images such as CT through image segmentation done in the stereo-lithography (STL) format, which describes only the surface geometry of a 3D object without any representation of color, texture or other common attributes. Then a smoothing, holes fixing is performed and meshing is done in commercial

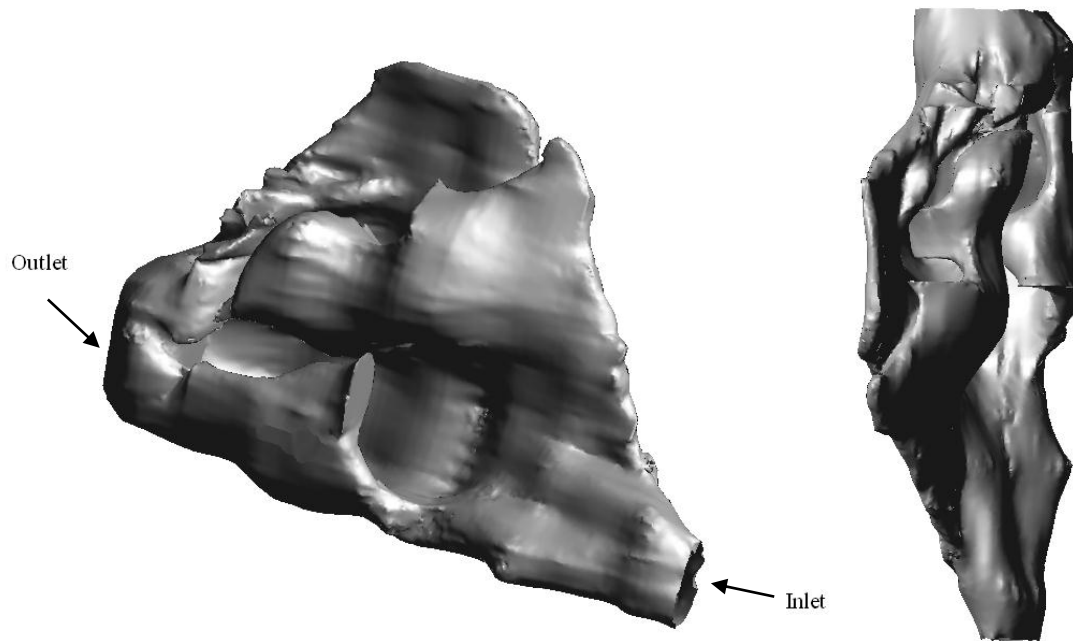meshing software, FLUENT GAMBIT [77]. The left hand side of nasal cavity and top view are shown in Fig. 3.5.



Figure 3.5: Reconstructed model of left hand-sided nasal cavity: (a) Human nasal cavity model (b) top view
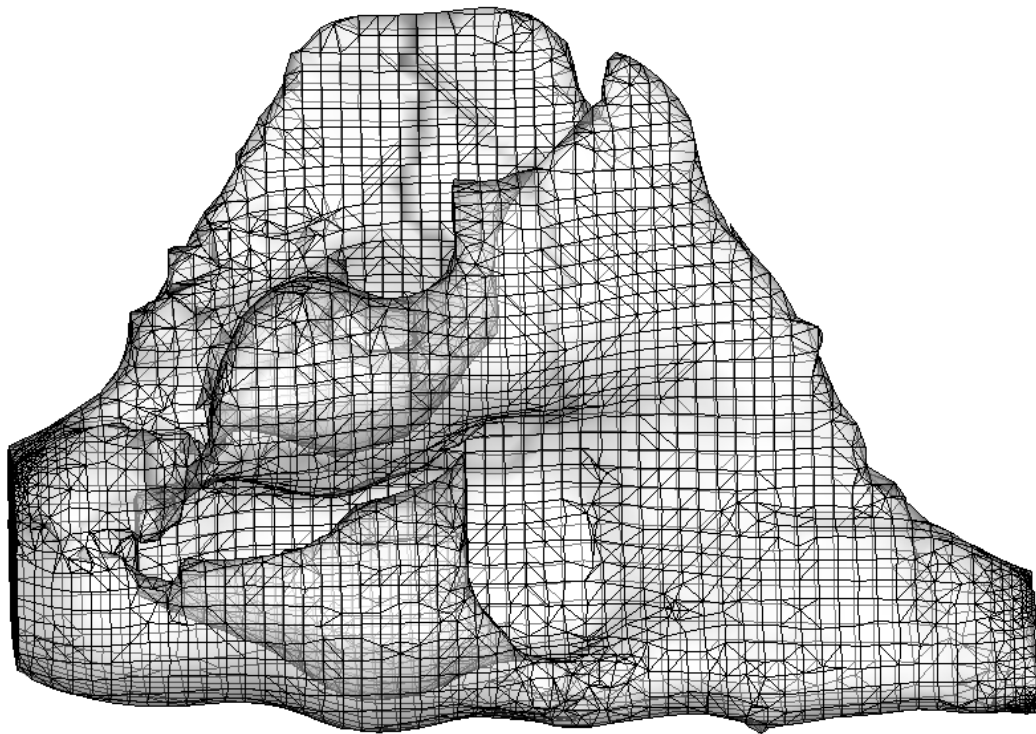
### 3.2.4.2 Grid Independence Test

As discussed in section 2.6, for a complex geometry such as the nasal cavity, an unstructured mesh was used as it is very time consuming if not impossible to achieve as a structured mesh. Unstructured meshes may involve the use of hexahedral, tetrahedral, pyramid, and wedge cells in combination, whereas a structured mesh is more reliant on hexahedral cells or the use of block-structured grids. The mesh was generated in mostly hexahedral and this is done with tons of experience with commercial software. An advantage in using an unstructured mesh for complex geometries is that the use of tetrahedral cells allows far fewer cells than an equivalent mesh consisting of hexahedral elements since the tetrahedral cells can be controlled in terms of clustering them in regions of the flow domain where they are needed. In contrast structured hexahedral cells will generally force cells to be placed in regions where they are not needed. However, one problem with tetrahedral cells is that their grid designs are prone to high aspect ratios which affect the skewness of the cell.

Additionally tetrahedral cells can never be aligned with the flow direction. These two problems can impede convergence and lead to numerical diffusion. Numerical diffusion is a common source of error and is also called false diffusion because it is a product of numerical error and does not represent a physically occurring phenomenon. A few techniques may be applied to minimize the likelihood of false diffusion such as choosing higher order discretization schemes and increasing the resolution of the mesh [77].
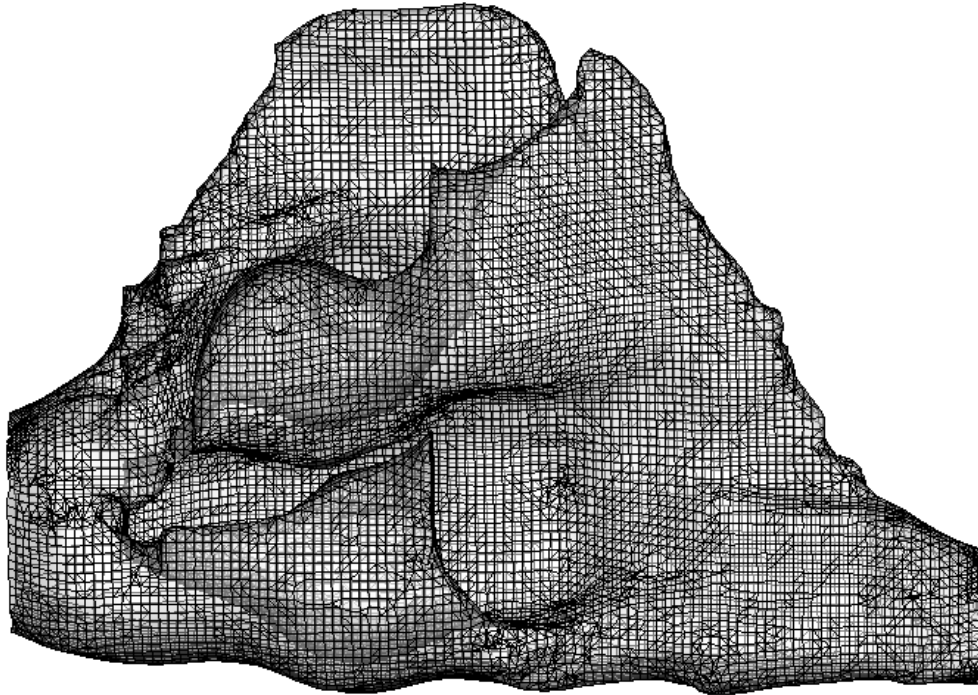
The grid independence test was conducted with three different mesh qualities as shown in Fig. 3.6. The mesh details are displayed in Table 3.2.

Table 3.2: Mesh details for grid independence test
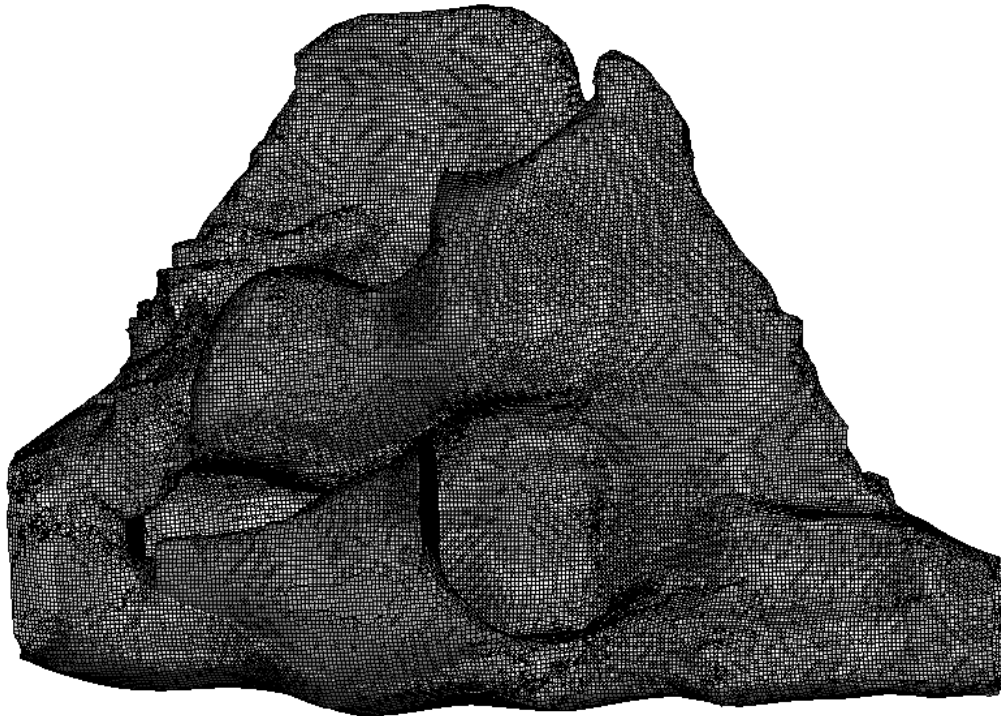
|  | Mesh I | Mesh II | Mesh III |
|---|---|---|---|
| Number of mixed cells (mostly hexahedral) | 25,225 | 109,840 | 568,801 |
| Number of faces at inlet | 184 | 366 | 783 |



(a) Mesh I of 25,225 cells

(b)    Mesh II of 109,804 cells



(c) Mesh III of 568,801 cells

Figure 3.6: Grid independence tests were carried out on 3 meshes. Mesh II was chosen to perform simulation

### 3.2.5 Boundary and Operating Conditions

The representative inertial parameter range, Reynolds numbers and associated parameter values of all test cases are shown in Table 3.3.

Table 3.3: Representative modeling parameter

| Reynolds number, $\mathrm{Re} = \dfrac{\rho u d_{inlet}}{\mu}$ | Re ~1,500 $(7.5 L/\min)$ | Re ~ 3000 $(15 L/\min)$ | Re ~ 4000 $(20 L/\min)$ | Re ~ 6000 $(30 L/\min)$ |
|---|---|---|---|---|
| Inertial parameter $I = d_{ae}^2 Q$ ( $\mu m^2 cm^3/s$ ) | $10^2 - 10^5$ | $10^2 - 10^5$ | $10^3 - 10^6$ | $10^3 - 10^6$ |
| Particle diameter, $d_p (\mu m)$ | 1 - 30 | 1 - 20 | $2 - 55$ | 2 - 45 |
| Particle density, $\rho_p \left( kg \cdot m^{-3} \right)$ | 1550 | 1550 | 1550 | 1550 |

The numerical simulations were carried out using commercial software ANSYS FLUENT (version 12.0.6) [83]. The velocities were initialized to inlet values for whole domain. In this model configuration, the constant inflow boundary condition was applied at the inlet surface. The internal walls were set to "enhanced wall treatment" function to consider the no-slip condition of airflow; and "trap" in Discrete Particle Model, meaning that particles touching a wall and deposit at that position. The flow at the exit assumes a fully developed condition and zero normal gradients exist for all flow variables except pressure $(P = 0)$. This type of outflow boundary condition is convenient as it allows the modeling of flow exits where details of the flow velocity and pressure are not known prior to solution of the flow problem. For stable and accurate iterative process, the relaxation factors for pressure and momentum were both set to 0.1, while the discrete phase source was set to 0.5 during the particle tracking. In FLUENT, at the end of each solver-iteration, the residual sum for each of the conserved variables was computed and stored, thus recording the

convergence history. The residuals for each of equations (each component of Navier-Stokes and continuity equations) rapidly reached convergence. The slope of the residual history curves was examined and the solution was considered converged when all residuals were less than $10^{-6}$. Convergence for steady state for both laminar and turbulent flow cases were achieved within 6500 iterations with current configuration.

Uniform distribution of anthracite particle entered the model with same inlet velocity; approximately 400 particles were injected from the inlet. It is reasonable to assume a particle hitting a wall sticks on it since airway walls are covered with mucus.

In this study, the overall percentage of particle deposition efficiency in the double bifurcation, $\eta$, was expressed as the ratio of number of particles deposited to the total number of particles injection:

$$\eta = \frac{N_{totaldep}}{N_{totalin}} \times 100$$

(27)

Here, $N_{totaldep}$ is the total number of particles deposited in the whole nasal cavity while $N_{totalin}$ is the total number of particles entered the nostrils.

The simulations were performed on the 6 Hewlett-Packard workstations with 8 GB of RAM and two 2.0 GHz CPUs each in Universiti Teknologi PETRONAS Simulation Laboratory. Typical run times for the fluid flow simulations on double processor were approximately 2 hours. Each particle tracking simulations, which consumed whole processing, took 2 minutes.

## 3.3 Governing Equations in Double Bifurcation

Similar to the investigation of fluid flow and particle deposition in human nasal cavity, the study of flow and particle dynamics in double bifurcation also consists of normal breathing rate (laminar flow) and heavy breathing rate (turbulent flow). The solution is obtained using commercial CFD software ANSYS FLUENT (version 12.0.6) by solving the Navier-Stokes and continuity equations with appropriate boundary conditions.

### 3.3.1 Laminar Flow

In this part, the governing equations resemble section 3.2.1.

### 3.3.2 Turbulent Flow

For turbulent inlet flow, large eddy simulation (LES) method was applied. LES is employed to study the effects of turbulent airway flow on particle deposition. The LES governing equations are obtained by filtering the time-dependent Navier-Stokes. In LES, momentum, mass are transported mostly by large eddies large eddies and resolved directly, while small eddies are modeled. The filtering operation for a variable $\bar{\phi}(x)$, is provided in Eqn. (28)

$$\bar{\phi}(x) = \frac{1}{V} \int_V \phi(x')G(x,x')dx' \tag{28}$$

where $V$ is the volume of a computational cell, and the filtered function $G(x,x')$ is defined in Eqn. (29)

$$G(x,x') = \begin{cases} 1 & for & x' \in V \\ 0 & otherwise \end{cases} \tag{29}$$

Hence the filtered Navier-Stokes equations are presented in Eqn. (30) and Eqn. (31)

$$\frac{\partial \overline{u_i}}{\partial x_i} = 0 \tag{30}$$

and

$$\frac{\partial}{\partial t}\left(\rho \overline{u_i}\right) + \frac{\partial}{\partial x_j}\left(\rho \overline{u_i}\,\overline{u_j}\right) = \frac{\partial}{\partial x_j}\left(\sigma_{ij}\right) - \frac{\partial \overline{P}}{\partial x_i} \tag{31}$$

where $\sigma_{ij}$ is the stress tensor due to molecular viscosity defined in Eqn. (32)

$$\sigma_{ij} \equiv \left[\mu\left(\frac{\partial \overline{u_i}}{\partial x_j} + \frac{\partial \overline{u_j}}{\partial x_i}\right)\right] - \frac{2}{3}\mu\frac{\partial \overline{u_l}}{\partial x_l}\delta_{ij} \tag{32}$$

where $\delta_{ij}$ is the Kronecker delta function, defined such that $\delta_{ij} = 1$ if $i = j$, and $\delta_{ij} = 0$ otherwise.

### 3.3.3 Particle Governing Equations

The particle tracking equation is referred to section 3.2.3.

### 3.3.4 Computational Model

*3.3.4.1 Geometry*

This geometry is based on the glass tube model employed in the experiment conducted by Kim & Fisher [84]. In this work, the geometry was sketched using Autodesk AutoCAD software and exported to ANSYS FLUENT Gambit to generate mesh and boundary settings. The system dimensions are shown in Fig. 3.7 with data sets summarized in Table 3.4. The cross-sections $2-2'$, $10-10'$ and $15-15'$ that aligned with bifurcation plane were referred to Zhao & Lieber [85] to perform validation (as shown in Fig. 3.7). Cross-section $10-10'$ is chosen as the inlet of the second generation tube.

Table 3.4: Geometric parameters for double-bifurcation models (see Figure 3.7). All dimensions in millimeters

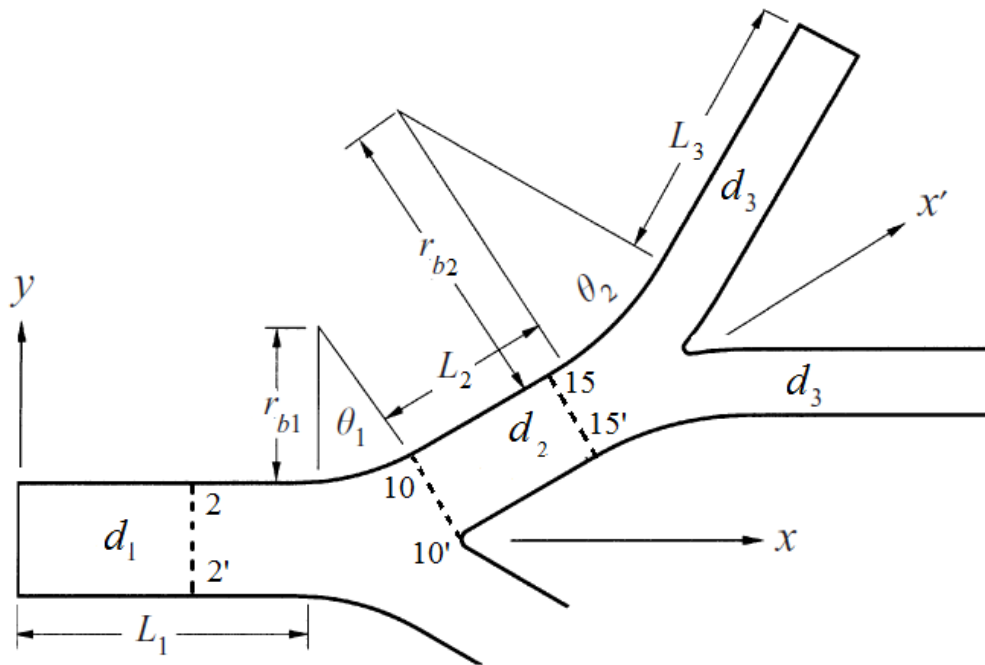| Bifurcation | First | Second |
|---|---|---|
| Parent duct diameter (mm) | $d_1 = 0.6$ | $d_2 = 0.5$ |
| Daughter duct diameter (mm) | $d_2 = 0.5$ | $d_3 = 0.35$ |
| Bifurcation radius of curvature | $r_{b1} = 2.7d_2$ | $r_{b2} = 4.7d_3$ |
| Length of ducts (mm) | $L_1 = 2.4$ | $L_3 = 3.367$ |
| | $L_2 = 0.836$ | |
| Bifurcation half-angle | $\theta_1 = 30°$ | $\theta_2 = 30°$ |



Figure 3.7: Planar symmetry plane as Comer et al. (2001) and Kim & Fisher (1994) for z=0. (Referred to Table 3.4 for data)

In order to investigate the final particles deposition locations, the walls of computational domain were divided into zones. The wall including the two frustums that generated a bifurcation was assigned "bifurcation" zone, while the rest of the

walls were assigned the "generation tube" zone. The illustration of computational domain is shown in Fig. 3.8. The detail size of the domain is shown in Table 3.4.
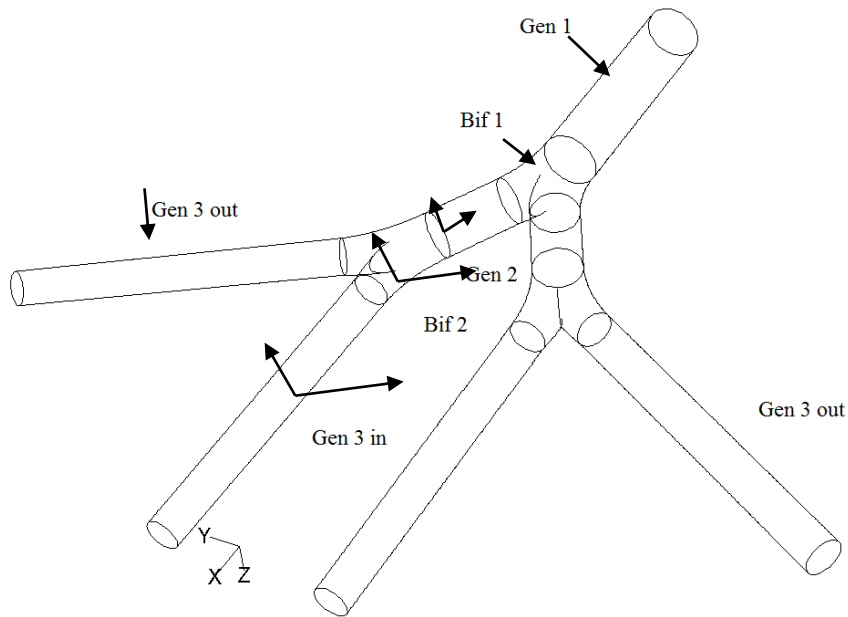
.



Figure 3.8: Computational domain was specified as bifurcations and generation tubes to differentiate the particles deposition locations
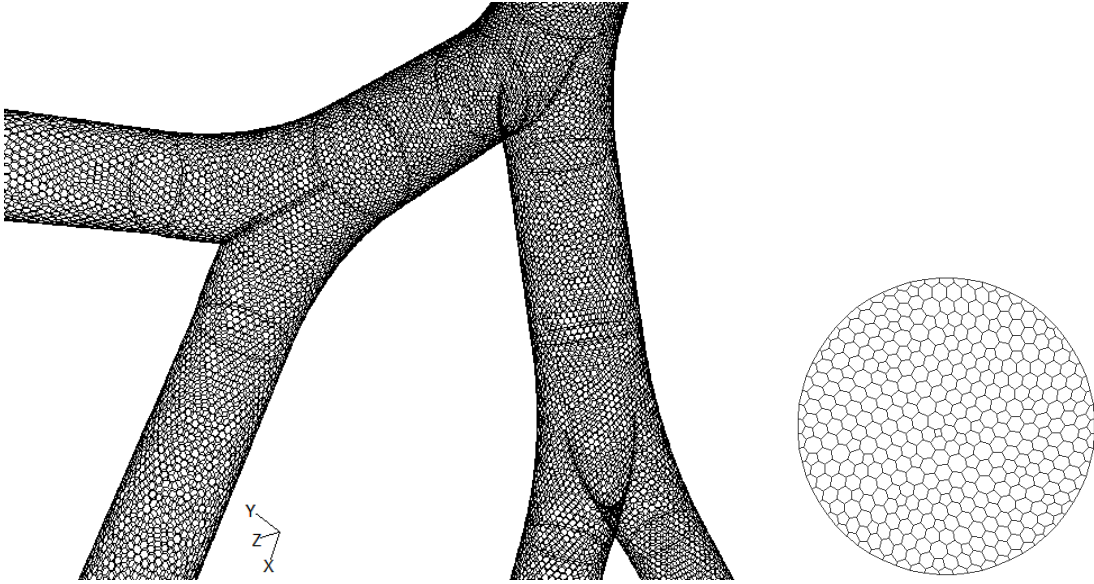
*3.3.4.2 Grid Independence Test*

The mesh was generated in polyhedra based on the surface information obtained from the Gambit models with geometric parameters for double-bifurcation models as in Comer *et al.* [9]. The grid independence test was conducted with three different mesh qualities as shown in Fig. 3.9. The mesh details are displayed in Table 3.5.
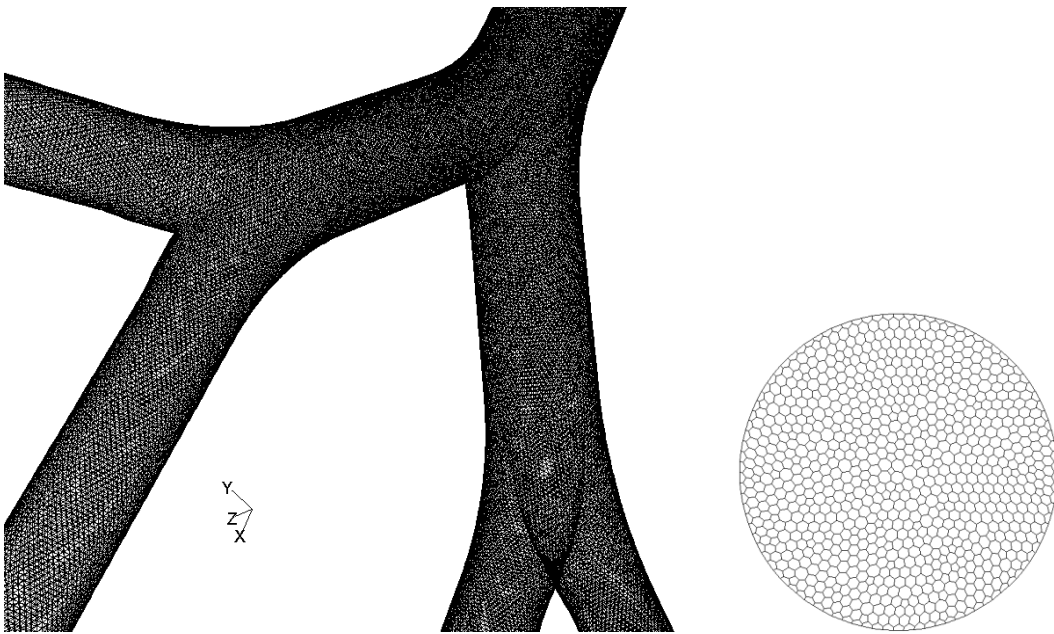
Table 3.5: Mesh details for grid independence test

|  | Mesh I | Mesh II | Mesh III |
| --- | --- | --- | --- |
| Number of cells (polyhedral) | 34,661 | 143,102 | 421,525 |
| Number of faces at inlet | 156 | 564 | 859 |
| Typical distance of the cell to the wall (mm) | 0.05 | 0.03 | 0.02 |
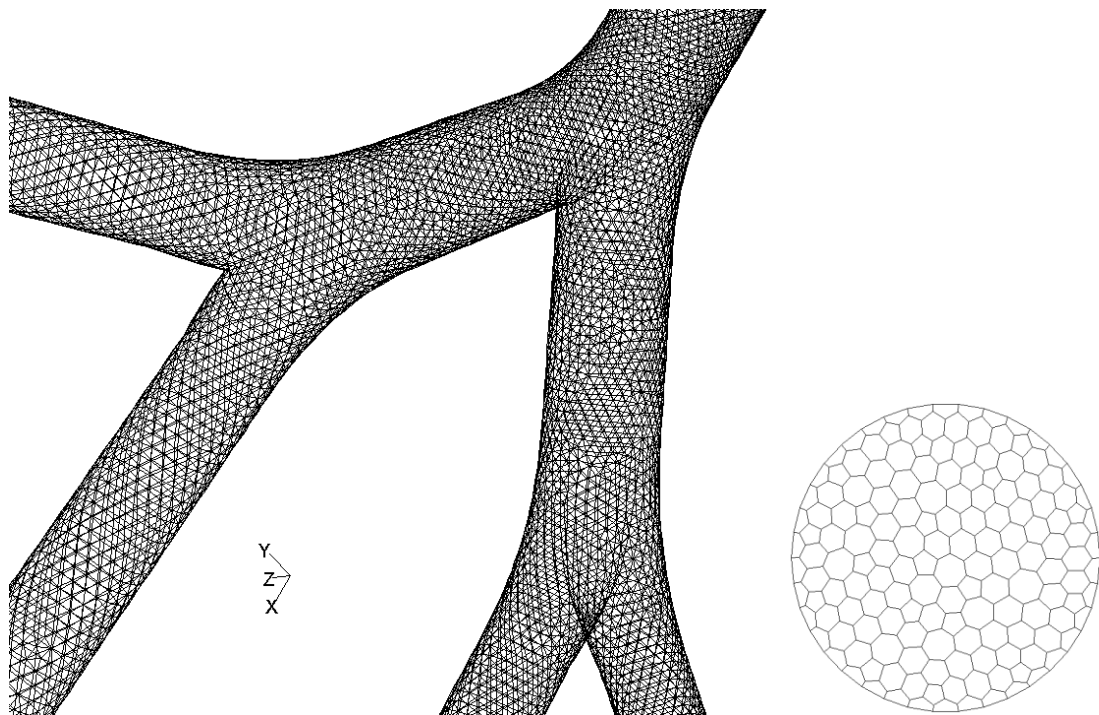


(a) Mesh I of 34,661 cells (left) and inlet boundary mesh (right)

(b) Mesh II of 143,102 cells (left) and inlet boundary mesh (right)



(c) Mesh III of 422,808 cells (left) and inlet boundary mesh (right)

Figure 3.9: Grid independence tests were carried out with 3 mesh qualities. Mesh II was chosen to perform simulation

### 3.3.5 Boundary and Operating Conditions

Velocity fields are converged using the finite volume method of FLUENT. For this model configuration, the inflow boundary condition was applied at the inlet surface. The reason of using constant entrance velocity profile rather than parabolic velocity profile as Kim & Fisher [14] introduced was that seems to be closer to reality, is that the length of larynx is much shorter than the length of tube employed in experiment, which could not produce parabolic entrance velocity. No-slip boundary conditions were applied for all wall surfaces. There are two possibilities for boundary conditions of the outlets for this double bifurcation configuration: (i) pressure conditions, where the outlet pressure was set to $P = 0$; and (ii) outflow conditions where the outlet volumetric flow is a fraction to inlet volumetric flow. Nowak [74] compared the results from both outlet boundary conditions and found out that the velocity profiles, particles deposition were virtually identical, the differences were no more than 0.5% deposition at any zone. Therefore, it was decided to use the outflow boundary conditions in this double bifurcation model. In addition, for stable and accurate iterative process, the relaxation factors for pressure and momentum were both set to 0.2.

The representative Stokes number range, Reynolds numbers and associated parameter values of all test cases are shown in Table 3.6. The simulations were applied for both laminar (Re = 500, 1,036 and 2,000) and turbulent (Re = 7,264 and 14,528) flows and the particle tracking simulations were applied for only 4 cases with Stokes number ranging from 0.02 – 0.12, while in the case Re = 1036, it was simulated for flow without injecting particles (indicates with N/A).

Table 3.6: Representative modeling parameters

| Reynolds number, $Re = \dfrac{\rho u d_{inlet}}{\mu}$ | Re =500 | Re=1036 | Re = 2000 | Re = 7264 $(30L/s)$ | Re = 14528 $(60L/s)$ |
|---|---|---|---|---|---|
| Stokes number $Stk = \dfrac{\rho_p d_p^2 u}{18\mu_p}$ | 0.02 – 0.12 | N/A | 0.02 – 0.12 | 0.02 – 0.12 | 0.02 – 0.12 |
| Particle diameter, $d_p (\mu m)$ | 3 - 7 | N/A | 3 - 7 | 1 – 6 | 1 - 6 |
| Particle density, $\rho_p \left( kg \cdot m^{-3} \right)$ | 3000 | N/A | 800 - 1500 | 1500 | 1500 |

The velocities were initialized to inlet values for whole domain. The residuals for each of equations (each component of Navier-Stokes and continuity equations) rapidly reached convergence. The slope of the residual history curves was examined and the solution was considered converged when all residuals were less than $10^{-6}$. Convergence for steady state laminar flow cases were achieved within 5000 iterations with current configuration. When in two turbulent flow cases, a transient simulation was applied with time step of 0.01 second and run for 1.5 second as average inhalation period for heavy breathing [86].

Uniform distribution of particle entering the model with same velocity as set inlet rate, approximately 409 particles were injected from inlet. It is reasonable to assume a particle hitting a wall sticks on it since airway walls are covered with mucus. The overall percentage of particle deposition efficiency in the double bifurcation, $\eta$, was expressed as ratio of number of particles deposited to total number of particles injected.

The simulations were performed on the 6 Hewlett-Packard workstations with 8 GB of RAM and two 2.0 GHz CPUs. Typical run times for the fluid flow simulations on double processor were approximately 5 hours. Each particle tracking simulations, which consumed whole processing, took 5 minutes.

CHAPTER 4

RESULTS AND DISCUSSIONS


**4.1 Flow in Blocked Channel**


**4.1.1   Stream Function Plots**

The stream function can be used to plot streamlines, which represent the trajectories of particles in a steady flow [87] (referred to Eqn. (4)). Streamlines are perpendicular to equipotential lines. In most cases, the stream function is the imaginary part of the complex potential, while the potential function is the real part. Considering the particular case of fluid dynamics, the difference between the stream function values at any two points gives the volumetric flow rate (or volumetric flux) through a line connecting the two points. Since streamlines are tangent to the velocity vector of the flow, the value of the stream function must be constant along a streamline. If there were a flux across a line, it would necessarily not be tangent to the flow, hence would not be a streamline. The usefulness of the stream function lies in the fact that the velocity components in the $x$- and $y$- directions at a given point are given by the partial derivatives of the stream function at that point. A stream function may be defined for any flow of dimensions greater than or equal to two, however the two dimensional case is generally the easiest to visualize and derive.

Fig. 4.1 shows the mean streamlines profile near the cylinder for Re = 150 and Br = 1/4 (Test case 1 of Table 3.1). For low Reynolds numbers, the creeping stream flows around the cylinder without forming any vortices in the end of the cylinder as shown in Fig. 4.1. The streamline is straight and symmetrical in shape. The legends of stream function (SF) were displayed with unit of $kg/s$.

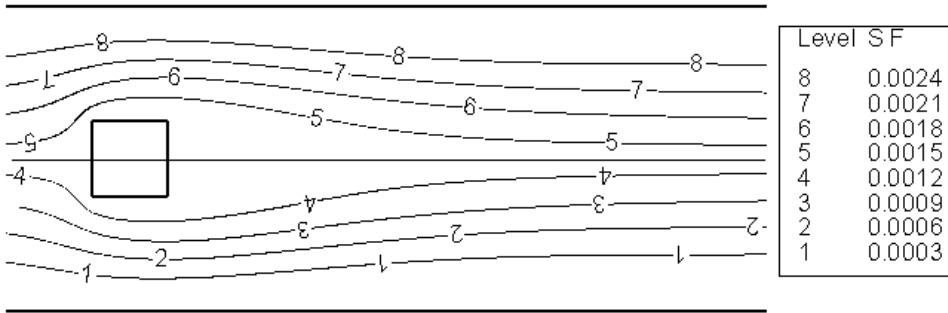| Level | S F |
|-------|--------|
| 8 | 0.0024 |
| 7 | 0.0021 |
| 6 | 0.0018 |
| 5 | 0.0015 |
| 4 | 0.0012 |
| 3 | 0.0009 |
| 2 | 0.0006 |
| 1 | 0.0003 |

Figure 4.1: Mean streamlines of flow in the channel with built-in square cylinder for Re = 150 (Test case 1 of Table 3.1)

An instantaneous zoom-in image of the transient flow field at Re = 900 is presented in Fig. 4.2. The plot clearly depict the regions of stagnating region right before the cylinder, then flow separation along the top ($x/B = 2$) and bottom ($x/B = -2$) walls of the cylinder, and asymmetric vortex shedding in the cylinder fluid-wake. Two asymmetrical recirculation regions were formed back of the cylinder. These are depicting the Von-Karman vortex sheet and the unsteady fluid-wake structure as discussed by Davis et al. [34]. Further downstream in the fluid-wake, the flow unsteadiness is weakened by the channel walls and the stream makes a curve due to accelerating velocity behind the cylinder.



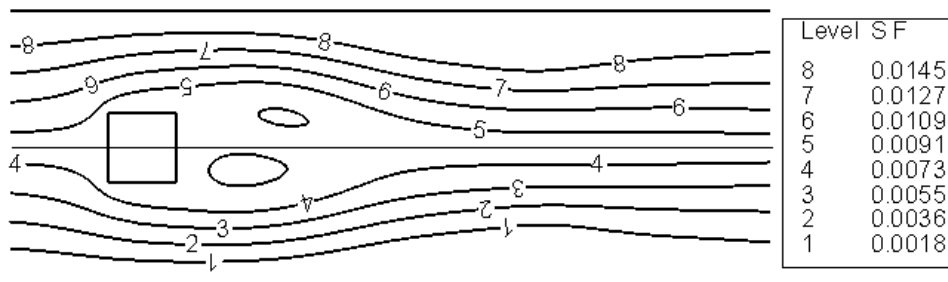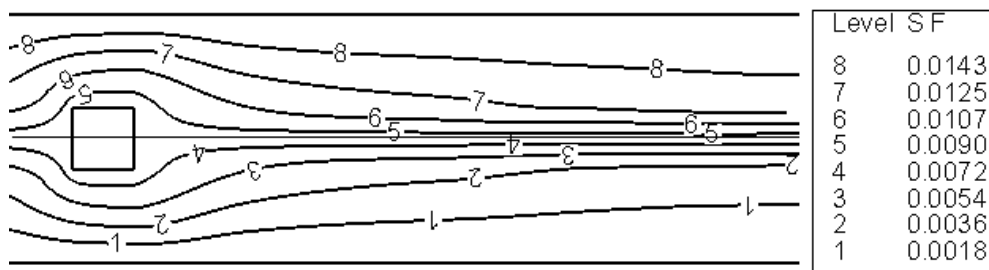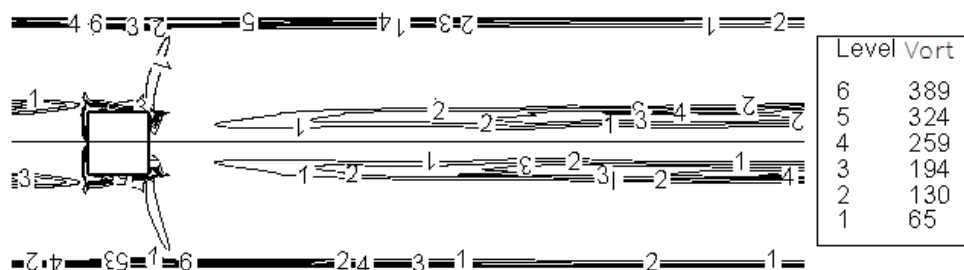| Level | S F |
|-------|--------|
| 8 | 0.0145 |
| 7 | 0.0127 |
| 6 | 0.0109 |
| 5 | 0.0091 |
| 4 | 0.0073 |
| 3 | 0.0055 |
| 2 | 0.0036 |
| 1 | 0.0018 |

Figure 4.2: Instantaneous zoom-in streamline near the cylinder image of the unsteady state flow field showing periodic, asymmetric vortex shredding at t=25s (Test case 4 of Table 3.1)

## 4.1.2　Relationship Between Streamlines and Vorticity

Fig. 4.3[(a) − (g)] show the streamlines and vorticity contours at different instants of time for $Re = 900$ at different instants of flow (Test case 4 of Table 3.1). The close interaction of the vortical flow developed in the fluid-wake region of the cylinder with the walls of the channel. The asymmetric periodic vortex shedding was depicted more clearly in Fig. 4.3, which contains seven instantaneous images of the flow field. The stream function (SF) was with unit of *kg/s* and vorticity (vort.) was with unit of number of circulation/$m^2$.
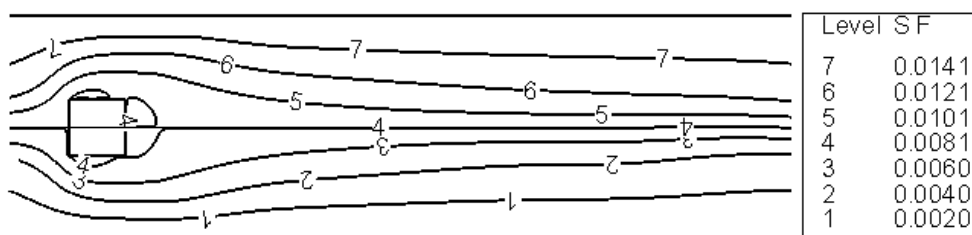
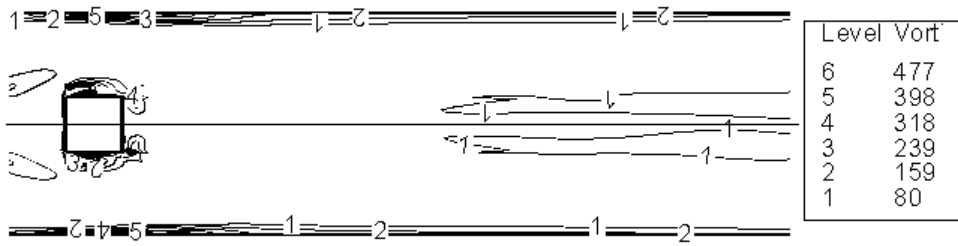| Level | S F |
|---|---|
| 8 | 0.0143 |
| 7 | 0.0125 |
| 6 | 0.0107 |
| 5 | 0.0090 |
| 4 | 0.0072 |
| 3 | 0.0054 |
| 2 | 0.0036 |
| 1 | 0.0018 |

(i)　　　Streamline plot

| Level | Vort |
|---|---|
| 6 | 389 |
| 5 | 324 |
| 4 | 259 |
| 3 | 194 |
| 2 | 130 |
| 1 | 65 |

(ii)　　　Vorticity plot

(a) t = 1.25 s

| Level | S F |
|---|---|
| 7 | 0.0141 |
| 6 | 0.0121 |
| 5 | 0.0101 |
| 4 | 0.0081 |
| 3 | 0.0060 |
| 2 | 0.0040 |
| 1 | 0.0020 |

(i)　　　Streamline plot

Level Vort
| | |
|---|---|
| 6 | 477 |
| 5 | 398 |
| 4 | 318 |
| 3 | 239 |
| 2 | 159 |
| 1 | 80 |

(ii)     Vorticity plot

(b) t = 3.75 s



Level S F
| | |
|---|---|
| 7 | 0.0141 |
| 6 | 0.0121 |
| 5 | 0.0101 |
| 4 | 0.0081 |
| 3 | 0.0060 |
| 2 | 0.0040 |
| 1 | 0.0020 |

(i)     Streamline plot



Level Vort
| | |
|---|---|
| 6 | 488 |
| 5 | 407 |
| 4 | 325 |
| 3 | 244 |
| 2 | 163 |
| 1 | 81 |
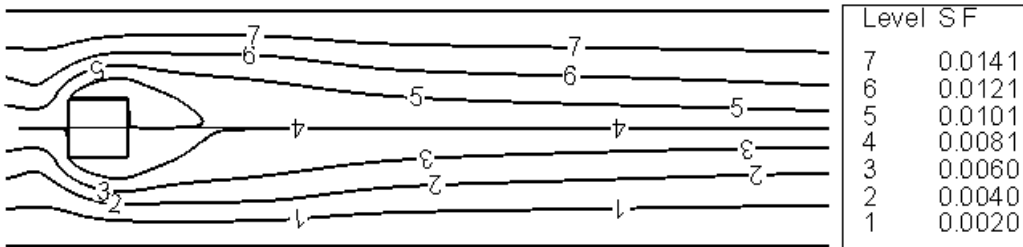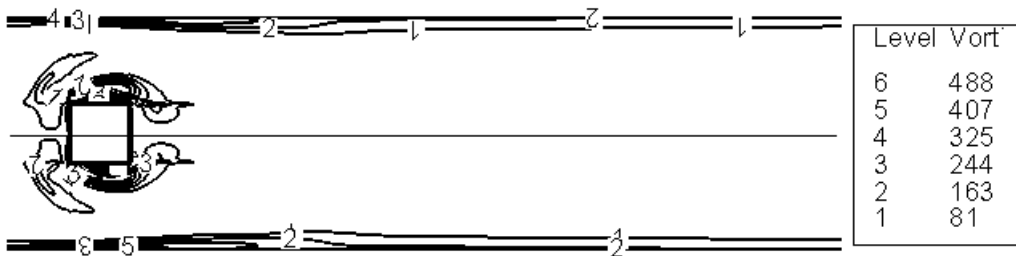
(ii)     Vorticity plot

(c) t = 7.50 s



Level S F
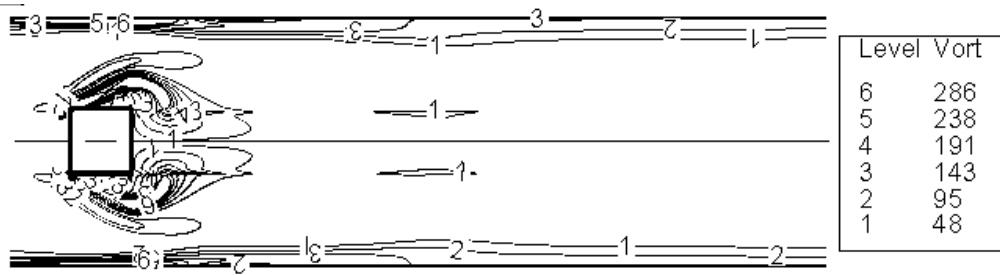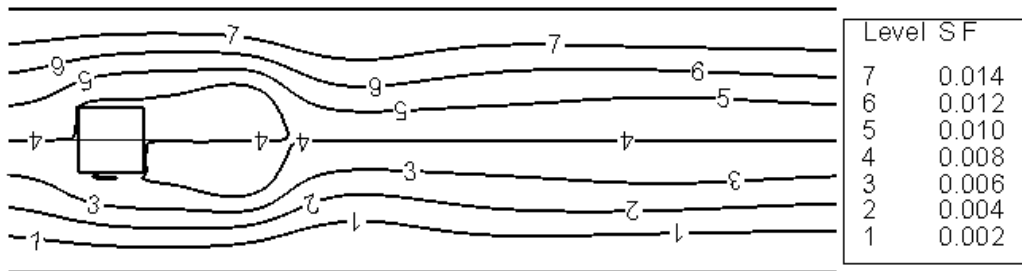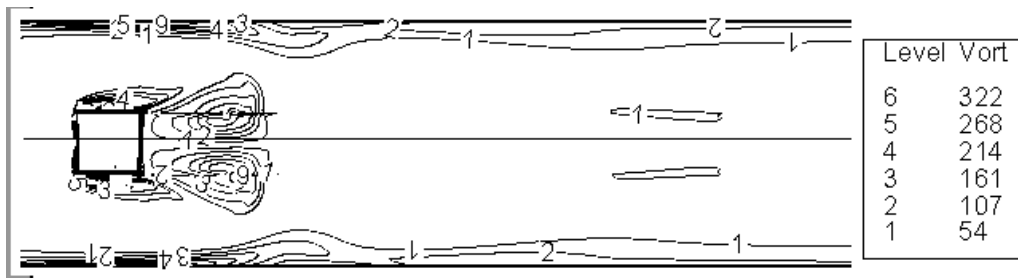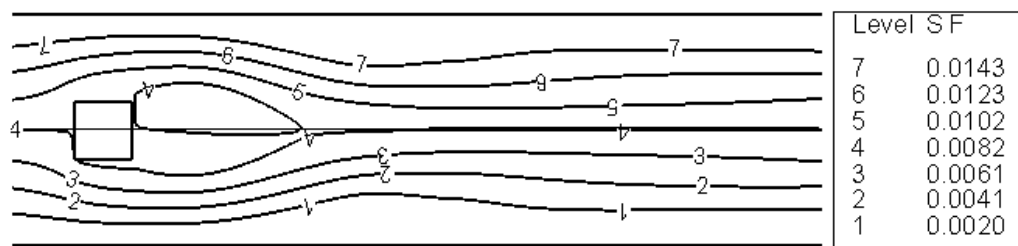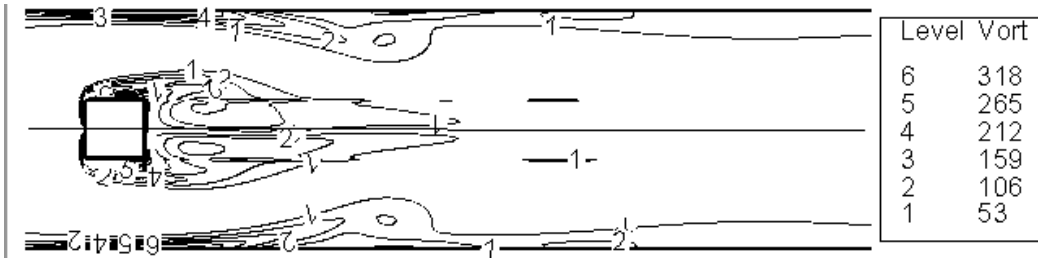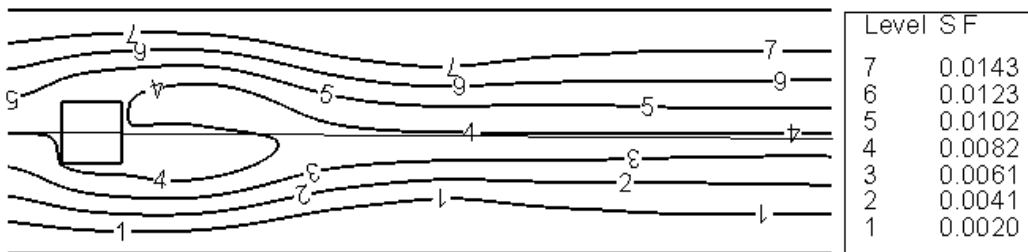| | |
|---|---|
| 7 | 0.0141 |
| 6 | 0.0121 |
| 5 | 0.0101 |
| 4 | 0.0081 |
| 3 | 0.0060 |
| 2 | 0.0040 |
| 1 | 0.0020 |
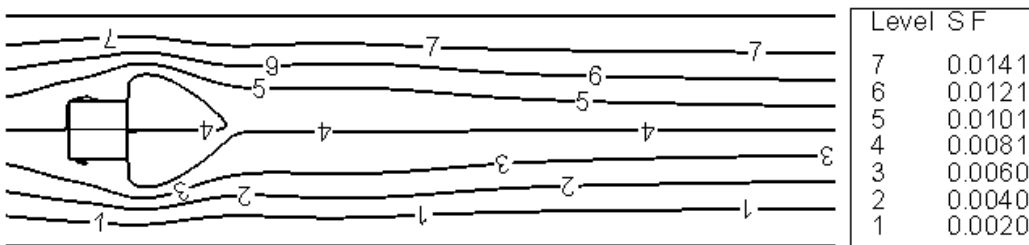
(i)     Streamline plot

(ii)    Vorticity plot

   (d) t = 11.25 s



(i)    Streamline plot



(ii)    Vorticity plot

   (e) t = 16.25 s



(i)    Streamline plot

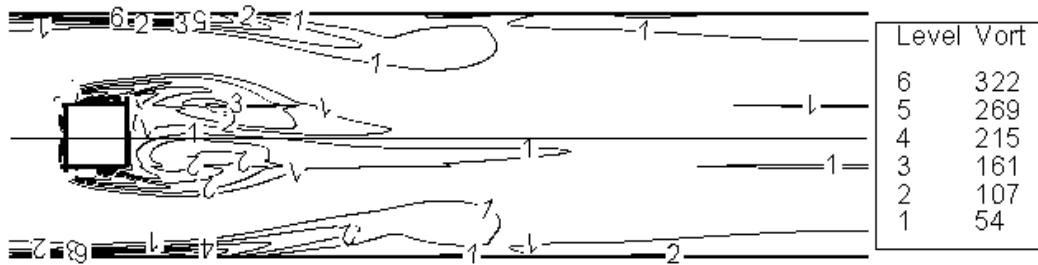| Level | Vort |
|---|---|
| 6 | 318 |
| 5 | 265 |
| 4 | 212 |
| 3 | 159 |
| 2 | 106 |
| 1 | 53 |

(ii)    Vorticity plot

(f)  t = 21.25 s



| Level | S F |
|---|---|
| 7 | 0.0143 |
| 6 | 0.0123 |
| 5 | 0.0102 |
| 4 | 0.0082 |
| 3 | 0.0061 |
| 2 | 0.0041 |
| 1 | 0.0020 |

(i)    Streamline plot



| Level | Vort |
|---|---|
| 6 | 322 |
| 5 | 269 |
| 4 | 215 |
| 3 | 161 |
| 2 | 107 |
| 1 | 54 |

(ii)    Vorticity plot

(g) t = 25 s

Figure 4.3: Streamlines and vorticity plots near blockage zoom-in vorticity contour at different instants of time for the flow past a square cylinder in a channel at Re =900 (Test case 4 of Table 3.1)

The presence of the cylinder (bluff body) creates an unsteady or periodic flow field characterized by the presence of shedding vortices and recirculation in the fluid-wake region of the cylinder. In addition, the flow contains a stagnation region in front of the cylinder, as well as regions of flow acceleration and deceleration around it.

- At t = 1.25 sec, the streamline shows the creeping flow past the square cylinder persists without separation and long vortices were formed before and after the cylinder, vortex strength at sidewalls of cylinder and channel walls were gentle in process of being shed from the top wall. (Fig. 4.3a)

- At t = 3.75 sec, in streamline plot, a pair of vortices was formed at sides and behind the cylinder and attached to the body; in vorticity plot, the vortex in front of cylinder shrank and moved towards the cylinder. The vortex behind the cylinder weakens and tends to exit of channel, vorticity at sidewall of channel and cylinder becomes stronger. (Fig. 4.3b).

- From t = 7.50 sec to t = 16.25 sec, the pair of vortex gets elongated, bigger and stronger. At sidewall of cylinder, the fluid-wakes grew in size and convect downstream, creating a vortical area right after the cylinder. On the channel's walls, whirls grew stronger, causing the asymmetrical flow in the channel (Fig. 4.3c, d, e).

- From t = 16.25 sec to 25 sec, the whirl expanded and weakened moving to the exit. At this time, the velocity became unstable since many vortices shredding (Fig. 4.3f, g).

### 4.1.3 Effects of Reynolds number on the Flow Regime

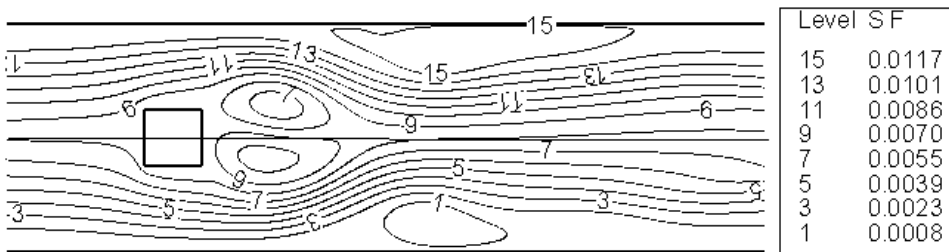Fig. 4.4 shows computational results in the vicinity of the cylinder by streamlines at four different flow Reynolds numbers (Re = 150; 300; 600 and 1200), each characterizing a totally different flow regime. Stream function (SF) was presented with unit of $kg/s$. Particles were not injected in this section.
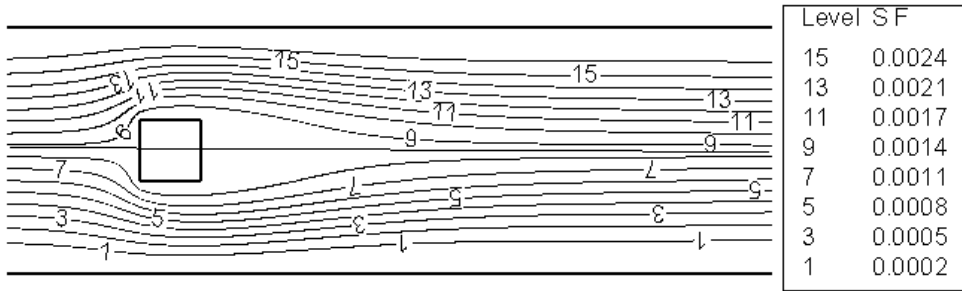
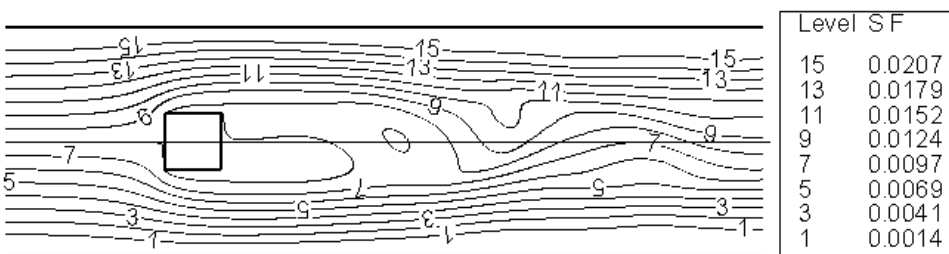(a) Re = 150
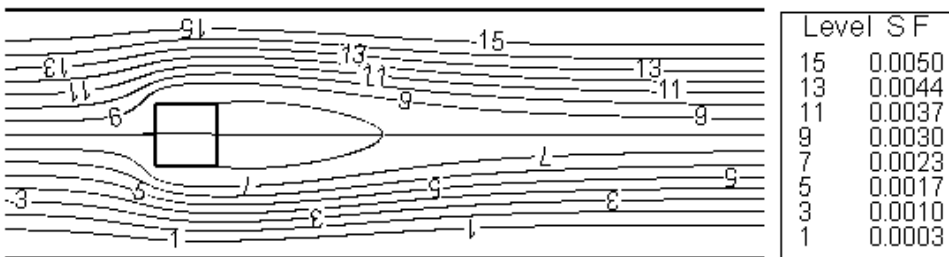


(b) Re = 300



(d) Re = 600



(e) Re = 1200

Figure 4.4: Streamlines plot of flow regime: (a) Re = 150 (Test case 1); (b) Re = 300 (Test case 2); (c) Re = 600 (Test case 3) and (d) Re = 1200 (Test case 5 of Table 3.1)

At low Re = 150, the fluid-wake was not formed any recirculation region after the cylinder, as shown in Fig. 4.4a. The magnitude of viscous forces decreased with increasing Re until it reaches to the critical Reynolds number, in this study which was $\text{Re}_{crit} = 300$, the flow comprised a steady recirculation region of two symmetrically placed vortices on each side of the fluid-wake separation of the laminar flow boundary layers occurs. As shown for $\text{Re} = 300$, owing to the sharp corners, the separation point is fixed at the railing edge. The steady, elongated and closed near fluid-wake became unstable when $\text{Re} > \text{Re}_{crit} = 300$ (Fig. 4.4b). At Re = 600, the oscillation was slightly formed near the outlet which led to a curve (Fig. 4.4c), and in Fig. 4.4d, at Re = 1200, the transverse oscillation was formed at the end of the near fluid-wake, and wave along the trail was initiated. Another important change in the flow structure was observed in the range $\text{Re} = 600$ and 1200, where separation already started at the leading edge of the cylinder (Fig. 4.4c and Fig. 4.4d). At Re = 1200, this strongly influenced the frequency of vortex shredding.

## 4.1.4 Effects of Stokes Numbers on Particle Injection

To characterize the effects of Reynolds number and Stokes number on particle distribution in the unsteady flow over a cylinder, the unsteady flow over a cylinder placed in a channel was simulated by solving the gas-phase equations. Once the effect of starting transient became negligible and the flow exhibited periodic behavior, particles of given Stokes number and velocity were injected from several transverse locations $x / B = 1 / 2$ to $x / B = -1 / 2$ at the channel inlet, right below the location of the cylinder. Secondly, the primary flow was frozen and switched to steady state before particles injection. Forty particles were injected into the channel to observe the behavior. The particles trajectories are computed by solving Eqn. (6) and Eqn. (7). The qualitative deposition behavior as a function of the particle Stokes number is depicted in Fig. 4.5, which shows instantaneous images of the particles injected from 21 locations upstream of the cylinder. The case $St = 0$ corresponds, to the fluid or tracer particles. The flow Reynolds number was Re = 1200. The magnitude of all the secondary terms in Eqn. (6) was negligible compared to that of the Basset history

term (the first two terms in Eqn. (6)). Consequently, the trajectories were computed by using only the steady state viscous term.
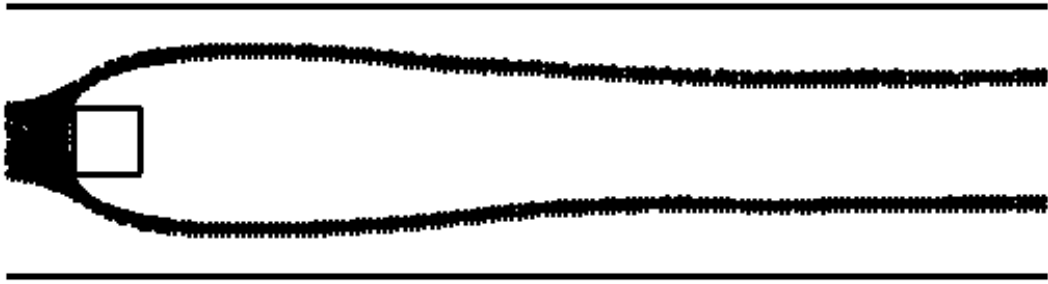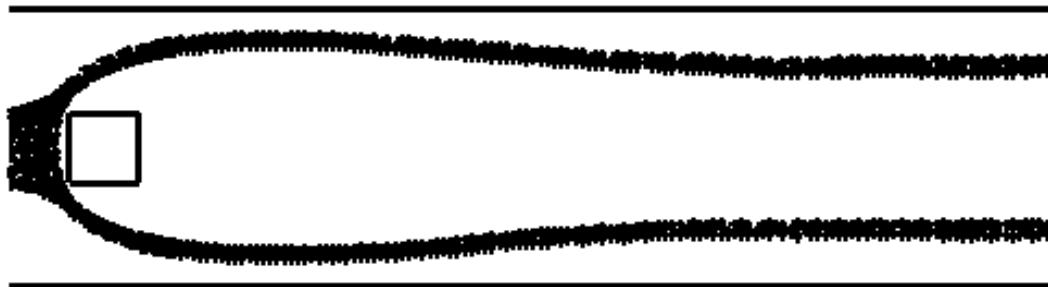


(a) Test case 5: $St = 0$ (massless particles)



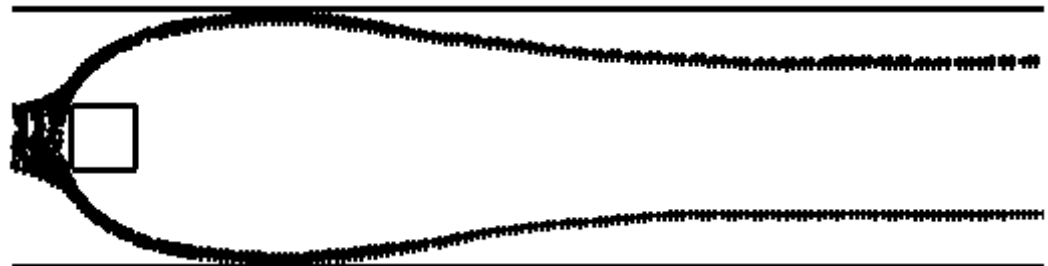(b) Test case 6: $St = 0.01$ ( $d_p = 6.6 \mu m$ )



(c) Test case 7: $St = 0.1$ ( $d_p = 21 \mu m$ )

(d) Test case 8: $St = 0.5$ ($d_p = 47 \mu m$)



(e) Test case 9: $St = 1$ ($d_p = 66 \mu m$)



(f) Test case 10: $St = 2$ ($d_p = 95 \mu m$)

Figure 4.5: Instantaneous images of particles injected from inlet of the channel for different Stokes numbers and Re = 1200 as Test case 5 to Test case 10 of Table 3.1

The particle distributions in Fig. 4.5 exhibit various dispersion behaviors. Particles with $St < 0.1$ behave like fluid particles, whereas those particles with $0.1 \leq Stk \leq 0.5$ exhibit intermediate $St$ behavior, i.e., they are dispersed more than the fluid particles. On the other hand, particles with $Stk \geq 1.0$ exhibit large $St$ behavior, i.e., they are essentially unaffected by the flow in the near fluid-wake region.

### 4.1.5 Effects of Stokes and Reynolds Number on Particles Injections

Fig. 4.6 shows particles distribution and vorticity stream at Stokes number of 0.1 for different Reynolds number: Re = 300, 600 and 12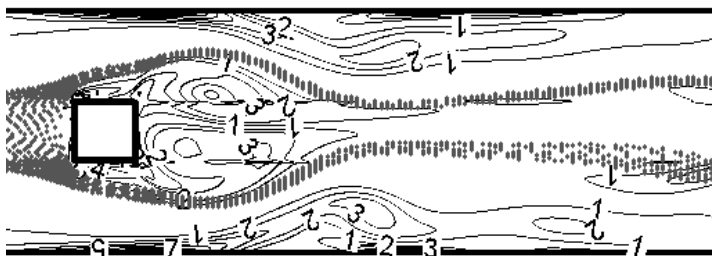00. The particle distributions were illustrated for $St = 0.1$ (in grey color) with the plot of corresponding vorticity contour (in black color) of the primary flow at three Reynolds numbers to investigate the mechanism of particle movement with Reynolds number.
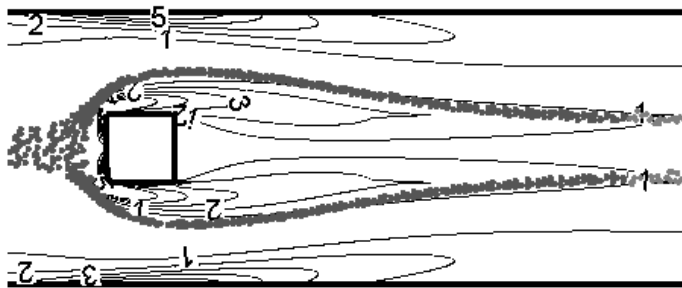


| Level | Vort |
| --- | --- |
| 7 | 75 |
| 6 | 70 |
| 5 | 64 |
| 4 | 51 |
| 3 | 39 |
| 2 | 26 |
| 1 | 13 |

(a) Test case 2: $St = 0.1$, Re = 300



| Level | Vort |
| --- | --- |
| 7 | 266 |
| 6 | 228 |
| 5 | 190 |
| 4 | 152 |
| 3 | 114 |
| 2 | 76 |
| 1 | 38 |

(b) Test case 3: $St = 0.1$, Re = 600
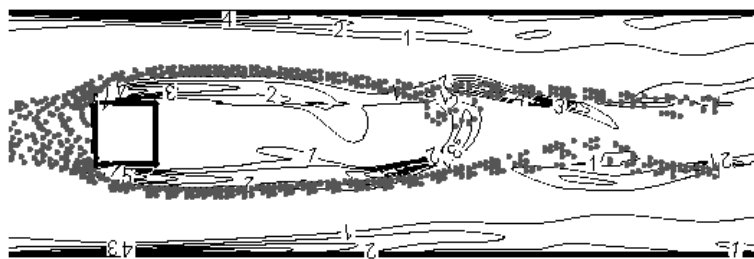


| Level | Vort |
| --- | --- |
| 7 | 550 |
| 6 | 471 |
| 5 | 393 |
| 4 | 314 |
| 3 | 236 |
| 2 | 157 |
| 1 | 79 |

(c) Test case 7: $St = 0.1$, Re = 1200

Figure 4.6: Particle distribution and vorticity contour plot for $St = 0.1$ and Re = 300, 600 and 1200 at $t = 25$ sec (Test case 2, 3 and 7 of Table 3.1)

For *St* = 0.1, particles were affected by both inertial force and drag force equally, therefore particles stream tend to form a curve between the vortices after the cylinder and near the channel walls. The particles stream was slightly deflected by few small vortices near the outlet and escape. Thus, the vorticity of the stream was the decisive factor to the particles distribution formation in the channel flow. In addition, while the majority of small size particles are distributed in the core of each vortex, the majority of intermediate size particles are distributed around the vortex periphery. These observations regarding particle distribution and dispersion in the presence of large vortex structures corresponded with those reported by many experimental and numerical studies [88] dealing with particle dispersion in shear flows. The above observations remain qualitatively similar as the Reynolds number is varied in the range $150 < \mathrm{Re} < 1200$. Within this range, as Re increases the size of vortex structures in the transverse direction become larger and, consequently, the particle dispersion increases. When the vorticity is symmetrical, the particle dispersion is symmetrical as shown in Fig. 4.8a and when the vorticity gets asymmetrical, the particle dispersion becomes asymmetrical also (Fig. 4.6b, c). For Re = 600, the vortices after the cylinder make a big periphery but short in length which lead the particle stream to a curly shape as shown in Fig. 4.6b, while for Re = 300 and 1200, the vortices after the cylinder are thin and long, thus the particle stream shape is straighter as shown in Fig. 4.6a, c.

## 4.2 Flow and particle movement in human nasal cavity

### 4.2.1   Verification and Validation

Three models with different mesh quality were employed to investigate the laminar flow with inlet flowrate of 7.5 L/min in human nasal cavity with length in z-direction of $0.081m$. The normalized velocity profiles ($u_i / u_{max}$) were plotted at the end of anterior (at distance $x_{max} = 0.038\,m$ from the inlet) and end of posterior – outlet (at distance $x_{max} = 0.081\,m$ from the inlet) for the grid independence test; where $u_i$ is the average velocity of the cross-sectional area at extracted   Mesh II and Mesh III

produced the results virtually identical as shown in Fig. 4.7. Thus the final mesh of the geometry was chosen as Mesh II (109,804 cells) to perform the rest of the simulations.
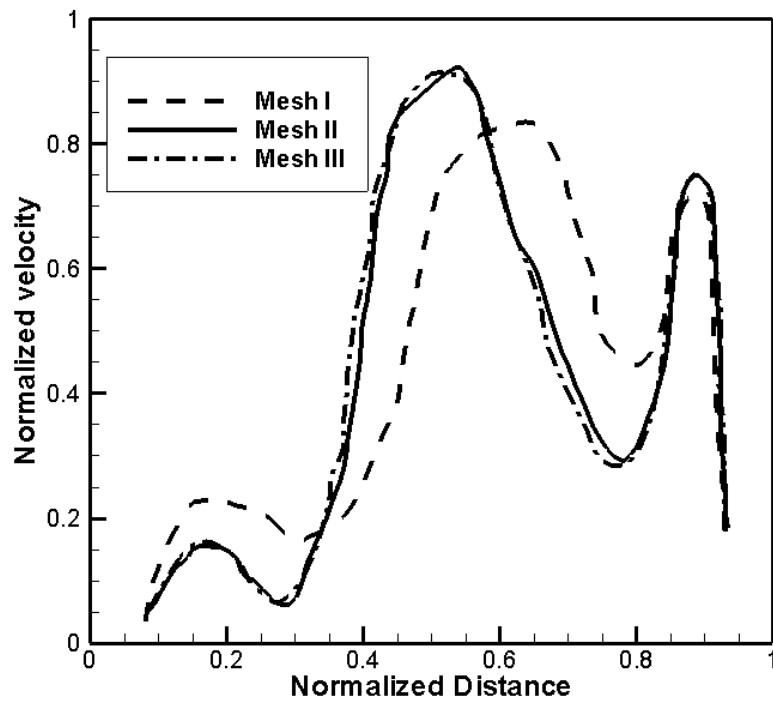


a)  Normalized velocity at end point of anterior, $u_{max} = 2m/s$, $x_{max} = 0.038m$
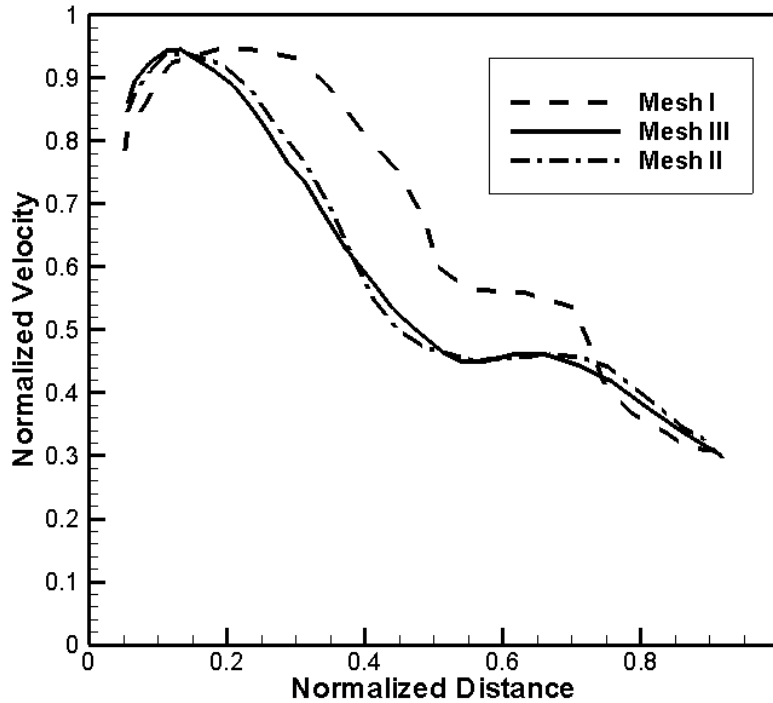
b)  Normalized velocity at end point of anterior, $u_{max} = 0.95m/s$, $x_{max} = 0.081m$

Figure 4.7: Grid independence test based on velocity profile lines taken at the anterior and posterior ends of the nasal cavity

Fig. 4.8 shows the comparison of the predicted total deposition efficiency in relation to inertial parameter with other experimental data [89, 90] and numerical data [12, 76]. An inertial parameter, $I = d_{ae}^2 Q$, is ideal to present the collection efficiency. The inertial parameter is a representation of the combined effect of Reynolds number and particle Stokes number. The total deposition efficiency of particles in a range of $1-28\mu m$ was investigated and this inertial parameter was changed by changing the diameter of the particle.
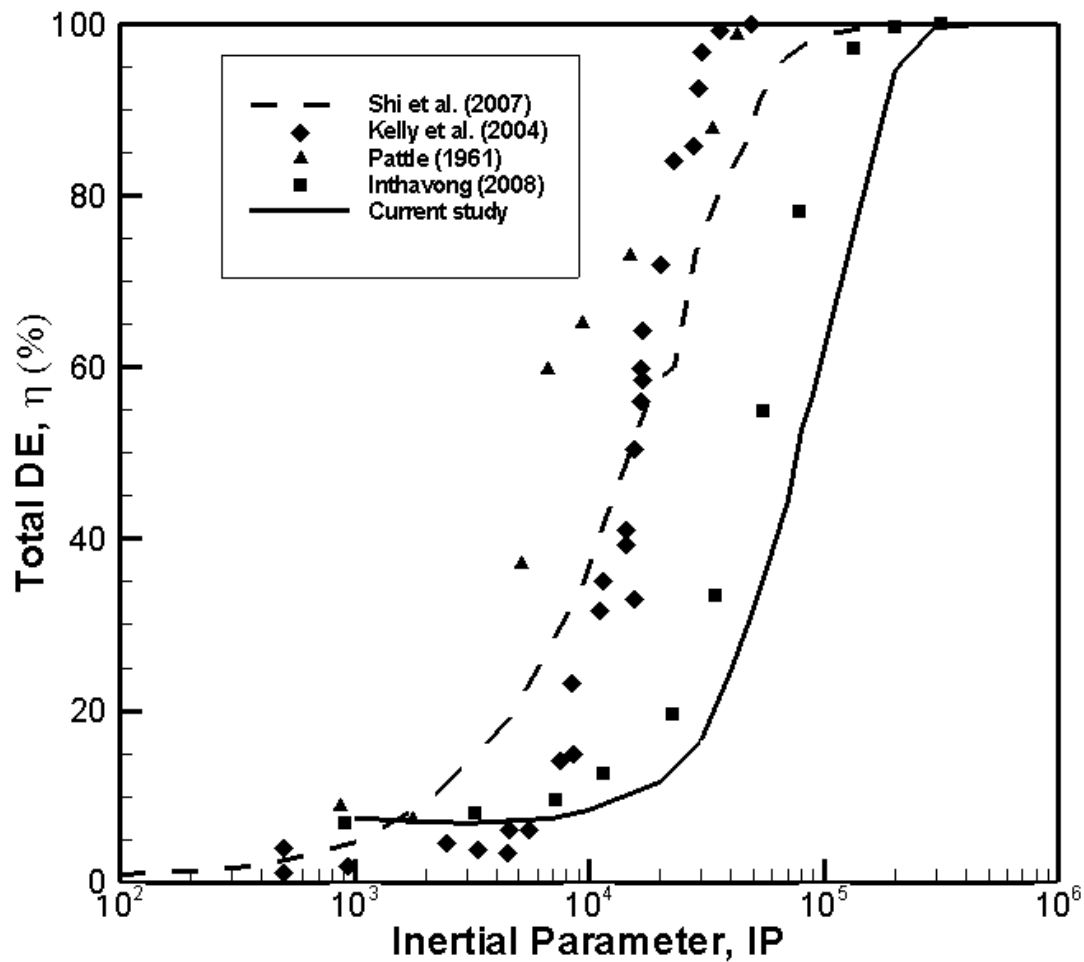
Figure 4.8: Total deposition efficiency of particles compared with other experimental data (Kelly et al., 2004; Pattle, 1961) and numerical data (Shi et al., 2007; Inthavong, 2008)

The experimental data of Kelly et al. [89] is different from the data of Pattle [46] explaining the uncertainty in the experiments. Also none of the set of the experiment data is smooth, rather scattered. This sudden jump and randomness also raise the question of repeatability and reliability. The CFD results of Inthavong [76] is far away from the Shi et al. [9] showing again the unpredictability and uncertainties in the simulation based on the individual's assumption in the simulation. The current CFD results do follow the trend of total deposition efficiency by predicting the curve reasonably. The differences in results may be caused by the different in geometries employed; Kelly et al [89] used 53 year-old non-smoking Caucasian male and

Inthavong et al. [76] used 25 year-old Asian male, while current study employed a shared resource CT scans to reconstruct the nasal cavity model. Certainly the smoothing does introduce error. Furthermore, according to Kelly et al. [89], inertial parameter considerations with different modeling geometry may result in differences in total deposition efficiencies.

Fig. 4.9 shows the quantitative similar trend between the current turbulent flow of 20 L/min and 30 L/min and results of Zhang [91] and Inthavong [76]. Inthavong [76] used a CT scan of the nose of a healthy 25 year old, non-smoking Asian male to reconstruct the nasal cavity geometry; then simulate the deposition of monodisperse pine particles in the range of $3-55 \mu m$ with the airflow inlet flowrate of 7.5 and 15 L/min. Meanwhile, Zhang [91] introduced an idealized mouth-throat to investigate the aerosols with mass median diameters of approximately 2.5, 5.0 and 6.0 $\mu m$ for steady inhalation flowrates of 30, 60 and 90 L/min. The effect of flow rate or inlet Re is also shown in Fig. 4.9. It shows that there is little difference of efficiency with the flow rate of 20 and 30 L/min. Inthavong [76]'s results are too random to be acceptable for inertial parameter lower than $10^4$, the current investigation show close to results of Inthavong [76], whereas, above this value, the result does differ a lot. The reason is being the different computational models (shapes) of the nasal cavity used.
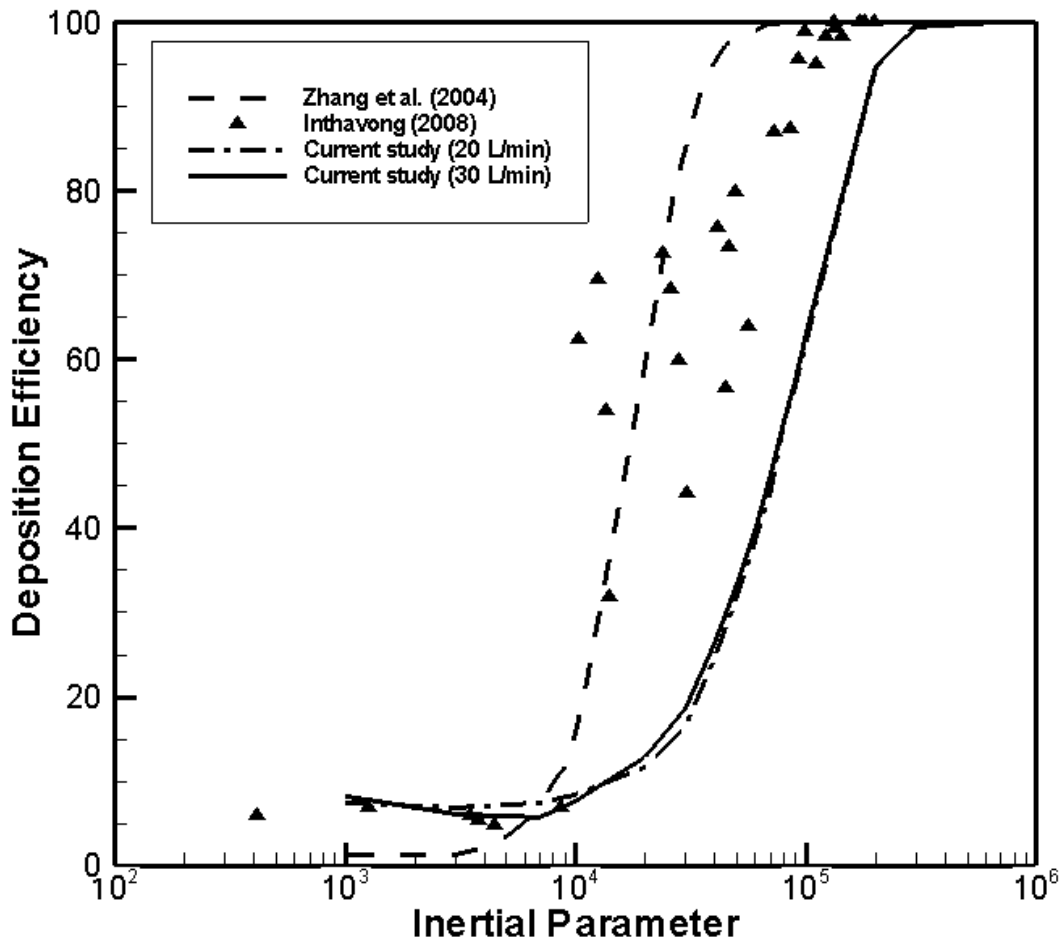
Figure 4.9: Comparison of deposition efficiency of current CFD with Zhang [91] and Inthavong [76] for particles released for turbulent flow

In conclusion, when neglecting the experiment uncertainties and differences in geometries, the current CFD methods produced an acceptable results and suitable to investigate the flow in nasal cavity.

### 4.2.2   Cross-Sectional Flow Velocity Profile Contour Plot

Fig. 4.10a shows 8 cross-sectional slides of the velocity profile in z-direction from the inlet to the outlet of human nasal left cavity. The slices considered are at S1, S2, S3, S4, S5, S6, S7 and S8 non-dimensional distance from the inlet referring to a cross-section which is 0.2 mm, 10 mm, 20 mm, 30 mm, 40 mm, 50 mm, 60 mm 70 mm and 80 mm away from the inlet of an 80 mm nasal cavity, respectively. Fig. 4.10b shows

the detailed contour of the velocity of magnitude at eight different cross-sections along the length of the nasal cavity. Fig. 4.10 is a case for 7.5 L/min flow rate (please refer to Table 3.3 for details). From the contour level of velocity profile (shown in legend bottom down), it can be seen that the velocity does vary significantly along the length of the nasal cavity.
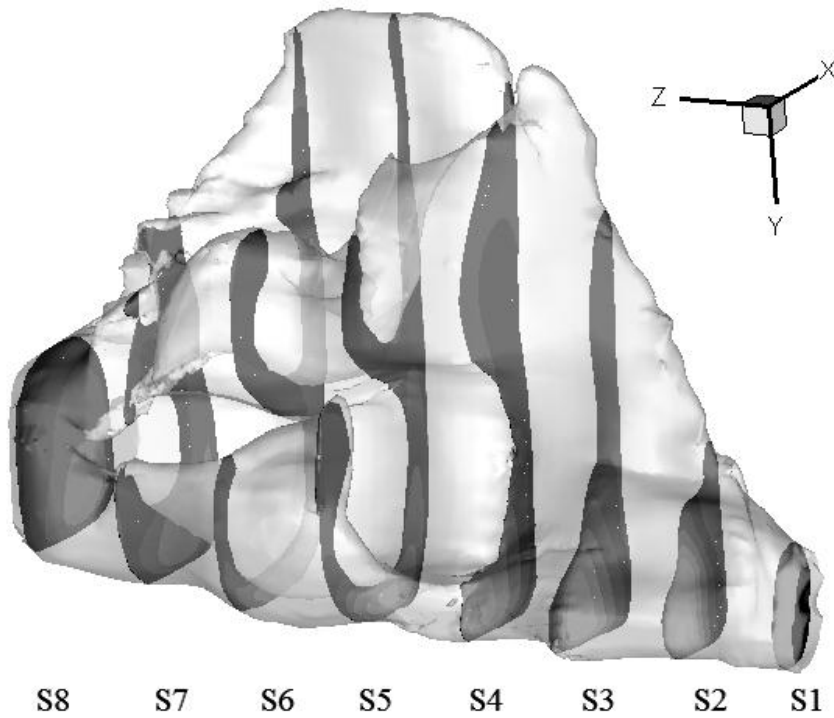


a) Contour level of velocity profile in nasal cavity for 8 cross sectional slides from inlet to outlet
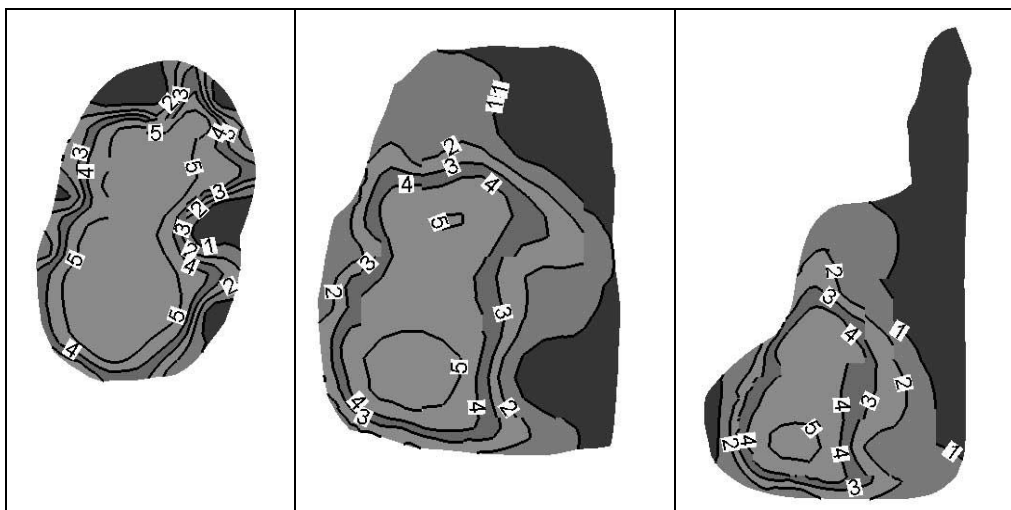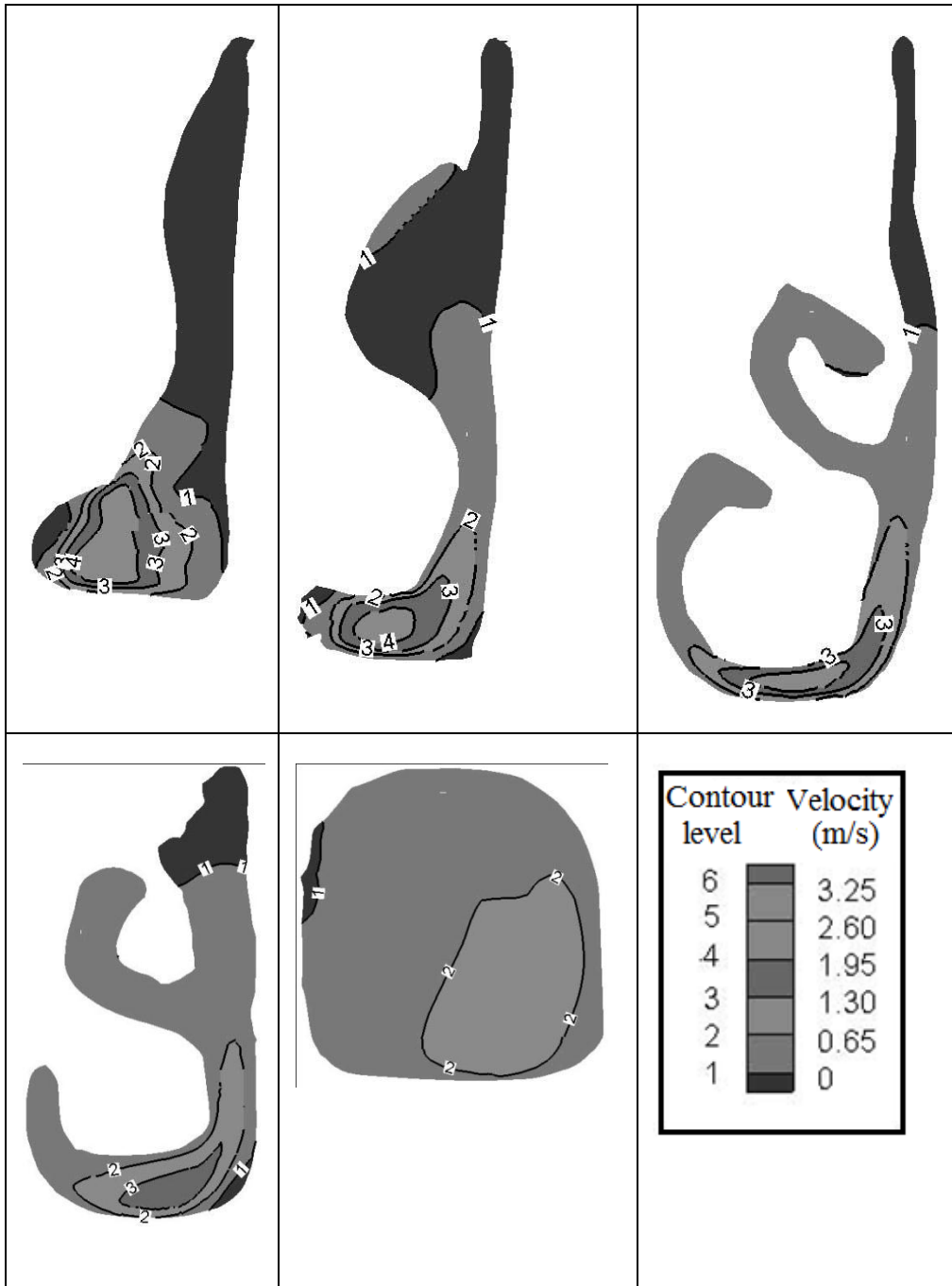
b)    Detailed contour level plot for cross-sectional slide

Figure 4.10: Contours of axial velocity (z-direction) for 8 cross-sectional slides of nasal cavity for inlet flowrate of 7.5 L/min at S1, S2, S3, S4, S5, S6, S7 and S8 (from right to left and top to bottom) nondimensional distance from the inlet

At S1, just 0.2 mm inside from the inlet, the contour velocity magnitude has a magnitude of 2.60 m/s in the core zone. At S2, the area is increased and so there is decrease in the area of higher core velocity. The shape and size of the nasal cavity changes significantly from S3 to S7 cross-sections and there develops a very complex flow in these zones and this will have effect on the deposition on the nasal cavity. The lower area of those slides represented with dark color (low velocity) will influent the deposition since not many vortices appeared. Meanwhile, the lower area of nasal cavity cross-sectional slides showed various changes in velocity contour, the flow was strong causing circulation and led particle to the outlet. The presence of the wall along that exists in nasal cavity produced circulation near the wall and forming vortices. This can be observed in the study of flow in a blocked channel discussed previously. For the nasal drug delivery, the desirable zone is from S2 to S6 (Inthavong et al. [76]) as will be discussed more in the particle modeling presented next. There are few recirculation zones developed in the nasal cavity because of the step change in the area.

## 4.2.3   Effects of Particle Size on Particle Deposition

Fig. 4.11 shows the location of the 400 particles after being deposited with 7.5 L/min injected rate case for a) Stoke number 0.15, b) Stoke number 2. The particle tracking was modeled using the particle modeling described in the modeling section. Before the injection of particles the primary flow was solved for 7.5 L/min and then the particles were injected from the inlet. Please note that the symbols of the spherical dots are not scaled, rather to make them visible, it was intentionally made bigger. This is a typical case which is presented out of many cases to show the location of the particles. Around 40% particles escaped the nasal cavity; some are trapped in the turbinate area. A significant amount of particle was trapped at the interior zone.
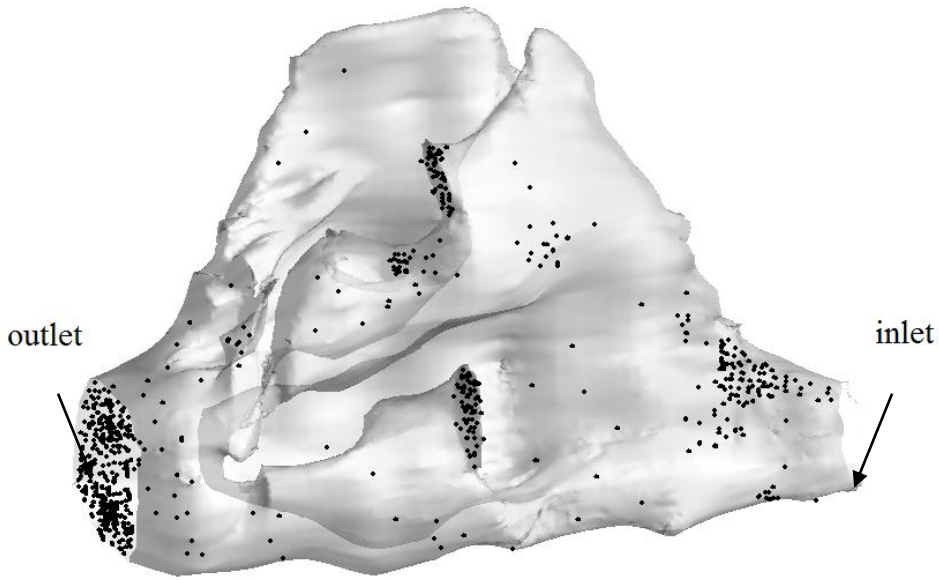
**(a)** *St* = 0.15
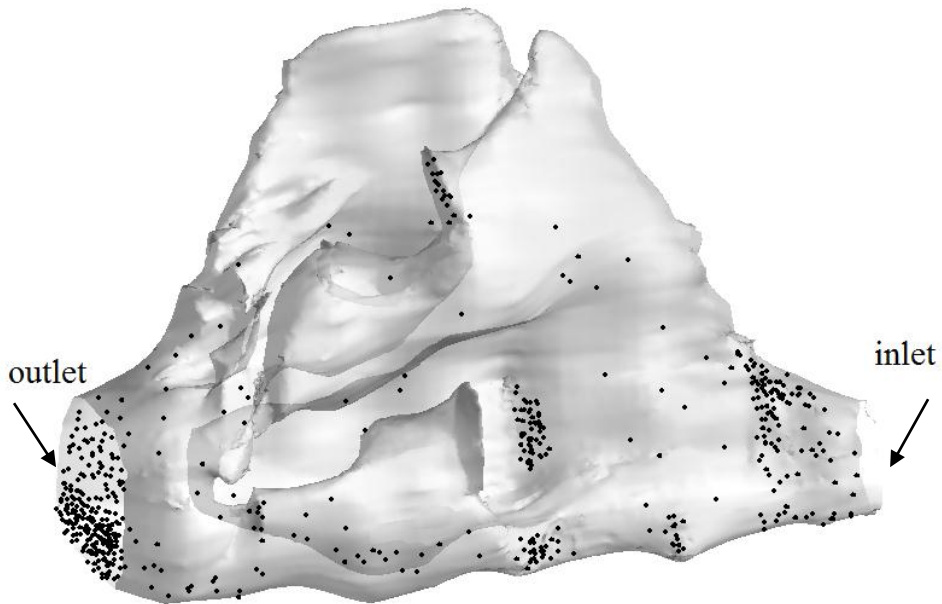


**(b)** *St* = 2.0

Figure 4.11: Final location of the particle for $Q = 7.5 \, \text{L/min}$, a) Stoke number 0.15, b) Stoke number 2.0

Fig. 4.12 shows the local $St$ along the z-direction of nasal cavity as function of non-dimensional distance the for different flow rates (four). Local $St$ is calculated based on the local average velocity at different cross-sections, which can be obtained from the FLUENT software. The corresponding distances from the entrances is divided by the total length of the nasal cavity to calculate the non-dimensional distance. The local $St$ decreases as the non-dimensional distance for all the flow rates. The cross-sectional area does changes so is the average velocity at that cross-section. The plots are not smooth in the nasal cavity partially because of smoothing software used. The $St$ does not vary that much for non-dimensional 0.40 to 0.90 confirming that the local cross-sectional average velocity in this zone does not change that much. As the flow rate increases, the local $St$ increases at the same location. However, the local $St$ vs. distance plots remain similar. Fig. 4.12 describes that for the same nasal cavity, the local $St$ can be varied five times for the same flow rate. This explains why the particle deposition in the nasal cavity is complex as shown in Fig. 4.11 previously.
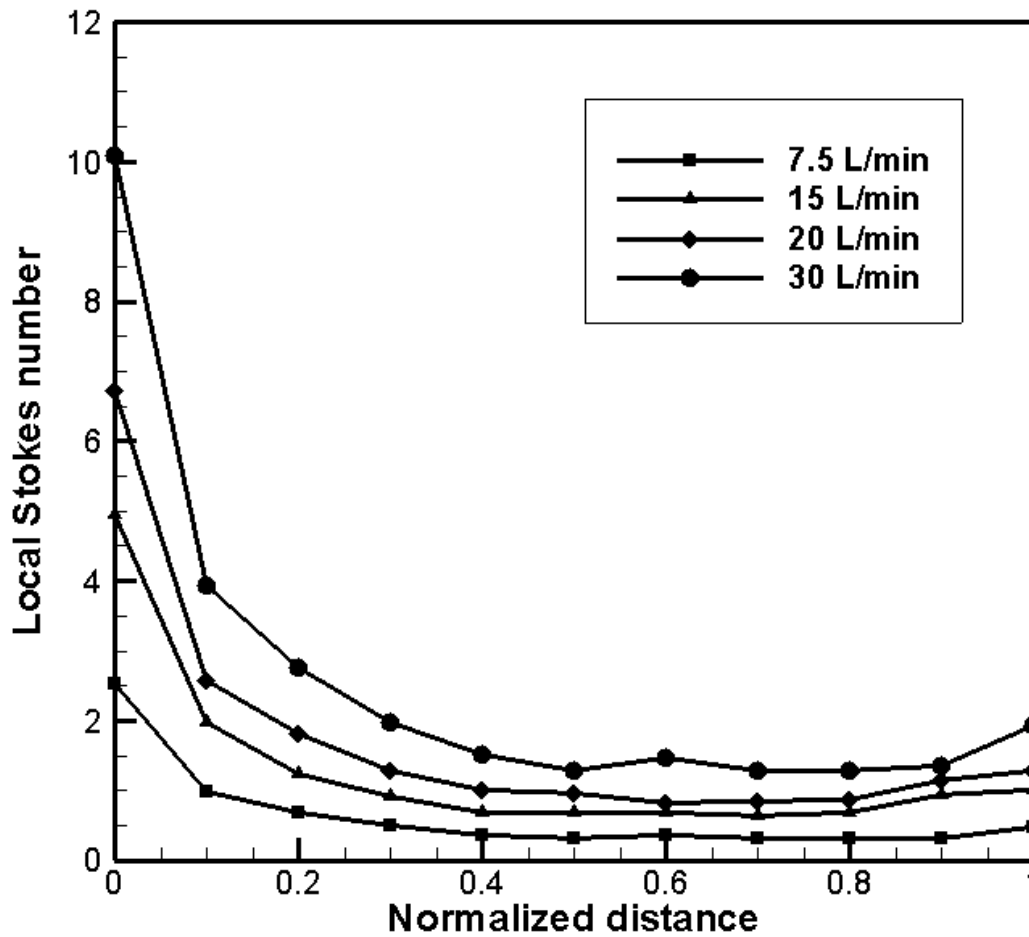
Figure 4.12: Local Stoke number vs. normalized distance from the entrance for a real human nasal cavity

Fig. 4.13 and Fig. 4.14 show the $\eta$ vs. $I$ and the $\eta$ vs. $St$ plots as a function for four different flow rates shows as function for four different flow rates. The inertial parameter, $I$, was calculated based on the inlet flowrate. The corresponding deposition was calculated on the whole wall of the nasal cavity. $St$ was calculated based on the inlet velocity. The corresponding deposition is calculated on the whole wall of the nasal cavity.
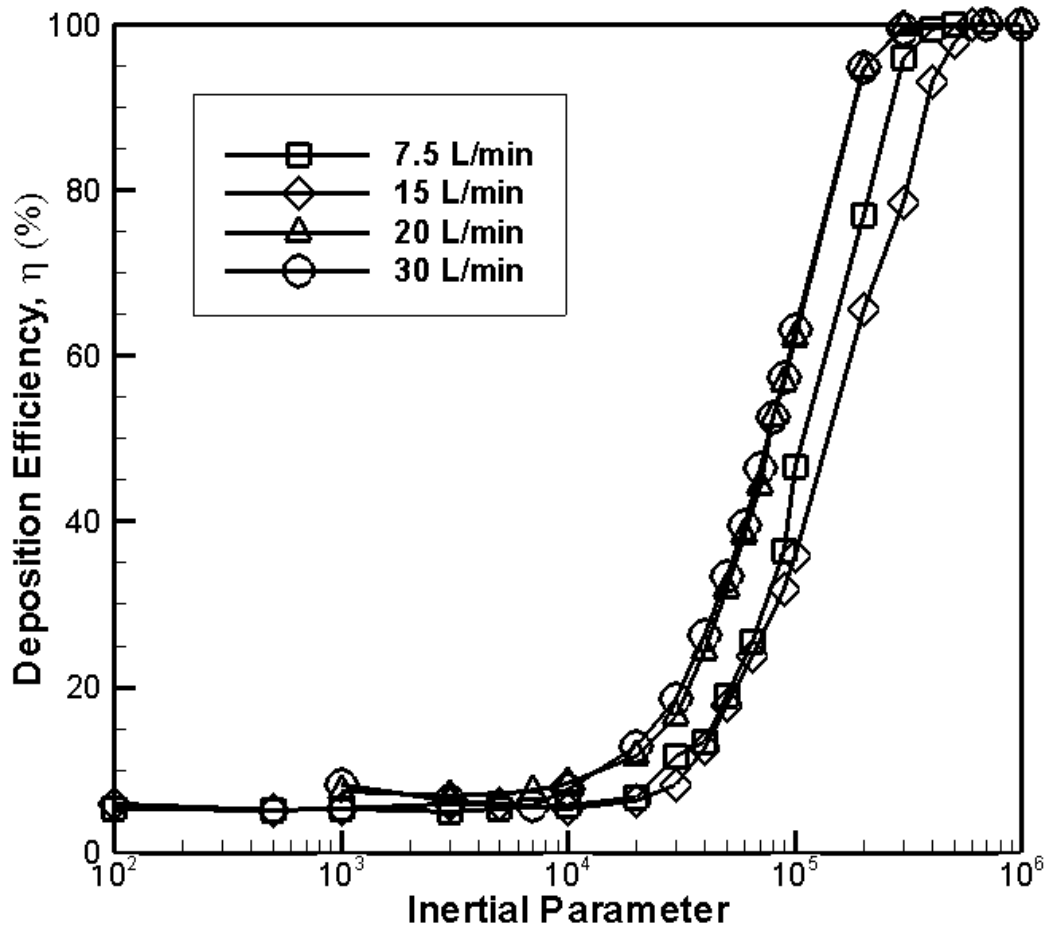
Figure 4.13: Deposition efficiency versus inertial parameter for different fluid flow rate in the real human nasal cavity
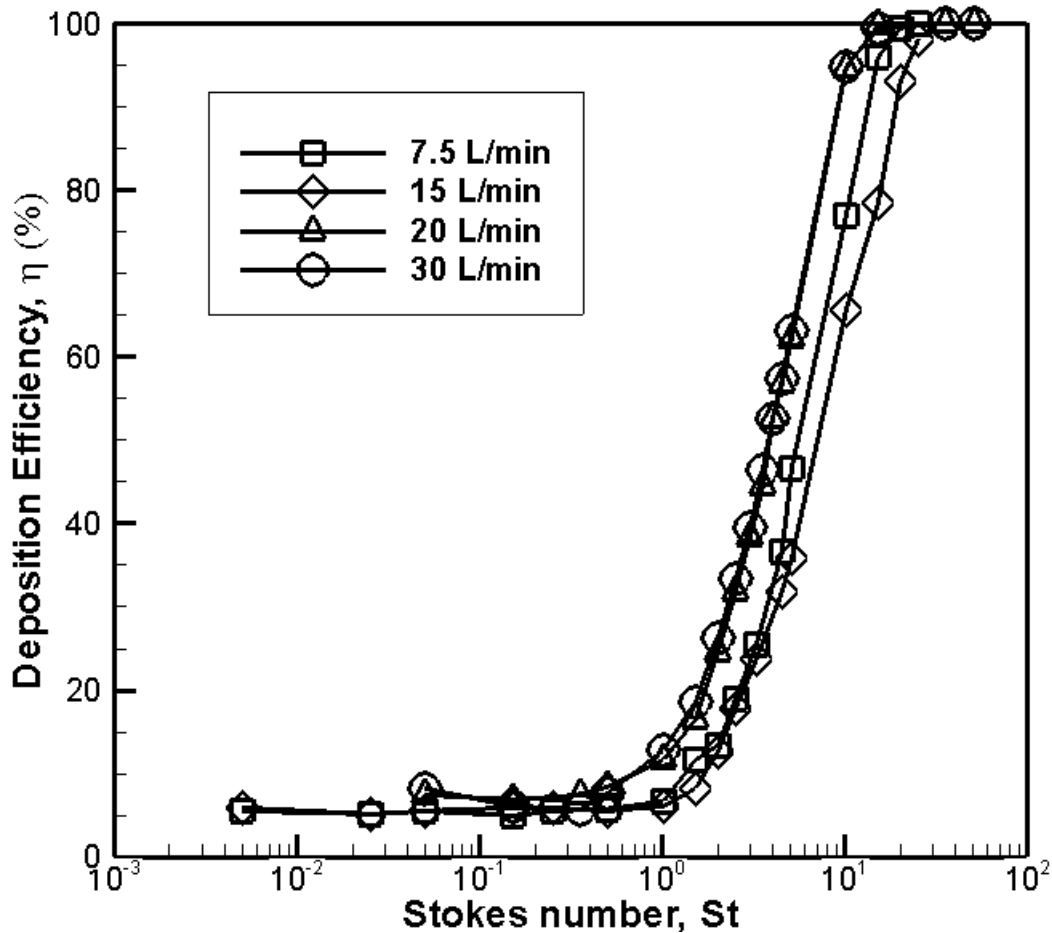
Figure 4.14: Deposition efficiency versus Stoke number for different fluid flow rate in the real human nasal cavity

Fig. 4.13 and Fig. 4.14 show a similar trend of plots for inertial parameter and Stokes number. This is reasonable since both $St$ and $I$ were essentially calculated from particle size. Collection efficiency increases as the $I$ increases for all the flow rates. From $I \sim 10^4 - 3 \times 10^5$, there was a difference in $\eta$ for the 7.5 and 15 L/min and for 20 and 30 L/min, it shows a similar trend in collection efficiency. From 15 L/min to 20 L/min, there was a substantial increase in the $\eta$, however, $\eta$ vs. $I$ showed similar trend for all flow rates. Fig. 4.13 suggested that for $I \sim 10^4 - 3 \times 10^5$, the collection can be increased significantly by changing the flow rate, for other inertia parameter it does not alter. Collection efficiency increases as the $St$ increases for all the flow rates. From $St = 4 - 12$, there is difference in $\eta$ for the 7.5 and 15 L/min. there is no significance difference in collection efficiency for 20 and 30 L/min. From 15 L/min to 20 L/min, there is a substantial increase in the $\eta$. However $\eta$ vs. $St$

remains similar for all flow rates. Fig. 4.14 states that for $St = 1-12$, the collection can be increased significantly by changing the flow rate, for other stokes number it does not alter. Nasal cavity is a complex structure, it is very difficult to explain precisely the effect of various flow rate on the $\eta$ vs $St$, however, the general trend for $\eta$ vs. $St$ states that there is a limited range of $St$ for which the collection efficiency will change for a particular flow rate.

### 4.2.4 Effect of Reynolds Number on Collection Efficiency

Fig. 4.15 shows the $\eta$ vs Re for $St =0.15$, 1, 2 and 4.5. The corresponding Re was taken from the test cases as shown in Table 3.3.
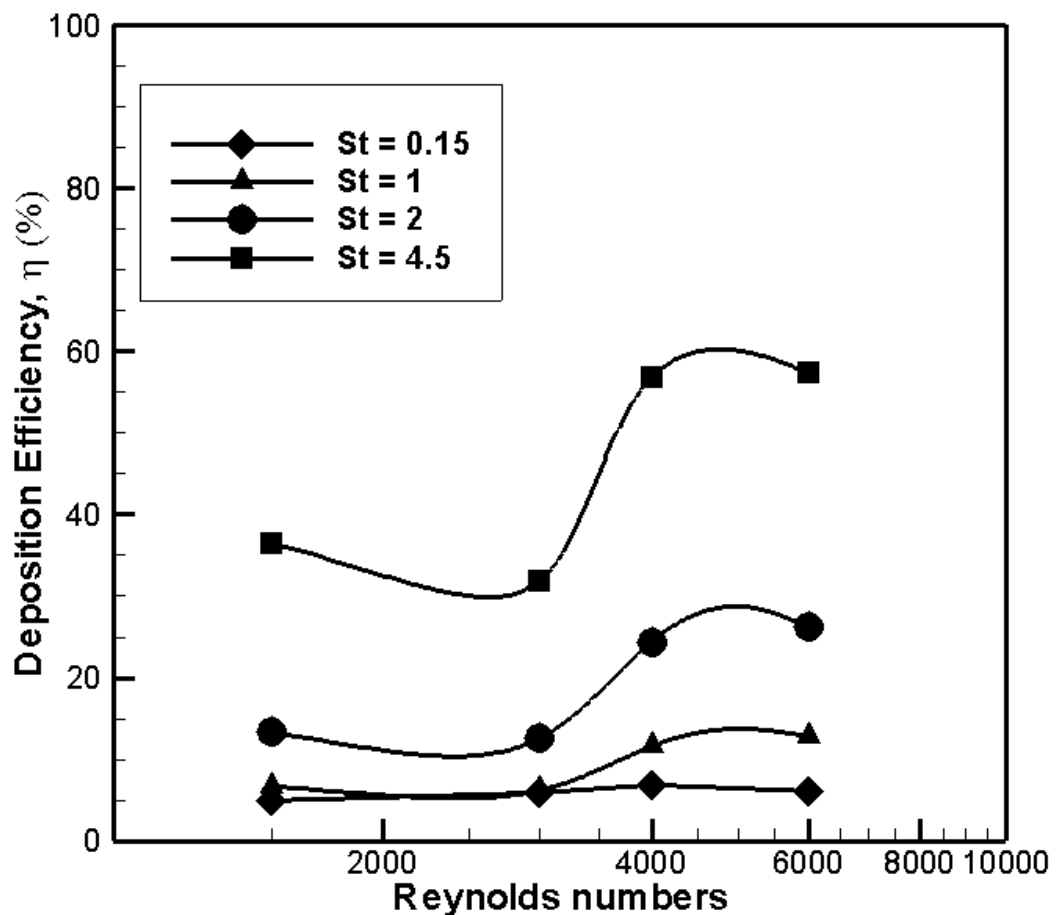


Figure 4.15: Deposition efficiency versus fluid Reynolds number on the real human nasal cavity

Fig. 4.15 shows that up to $\text{Re} = 3000$, the $\eta$ plots showed no significant differences for $St < 1.0$, but from $\text{Re} > 3000$ showed a significant increment in collection efficiency. Most of the cases, there were peak value of $\eta$ at $\text{Re} \approx 5000$. The peak of collection efficiency was sharper for higher Stoke numbers. The collection efficiency increases with Stoke number for the same Reynolds number which was discussed in flow in blocked channel. However, the increase of collection efficiency with Stoke number is faster for higher Reynolds numbers and there is a sharper jump of collection efficiency at $\text{Re} = 3000$ for $St = 4.5$, from 32% to 56%. Earlier researchers did not quantify the effect of Re so precisely. With increasing Re, the $\eta$ can be increased as high as ~20%, however this result is limited to 20% only, since human in breathe rate cannot exceed a certain flowrate.

## 4.3 Flow and particle movements in double bifurcation

### 4.3.1 Verification and Validation

- Verification

The computational simulation was performed at Re = 1036 (Table 4.3) to compare the axial velocity in cross-section, $2 - 2'$, $10 - 10'$ and $15 - 15'$ of Fig. 3.7 with experimental data of Zhao & Lieber [85] and Comer *et al.* [10]. Mesh II was considered to generate all the detailed comparisons in Fig. 4.16.
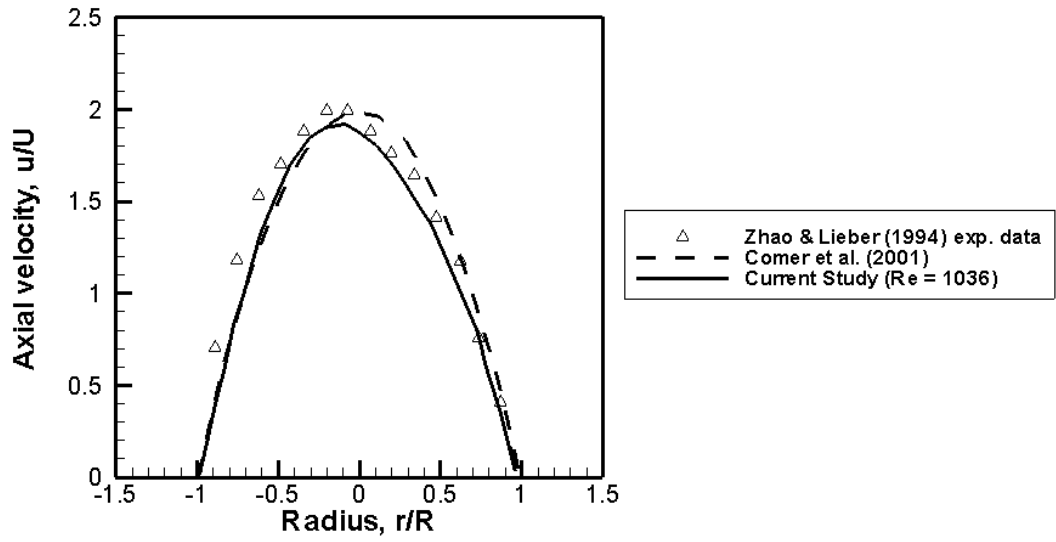
(a) Cross-section $2-2'$



(b) Cross-section $10-10'$

(c) Cross-section $15-15'$

Figure 4.16: Comparison of axial velocity at Re = 1036 with experimental data of Zhao & Lieber (1994) and computational data of Comer et al. (2001)
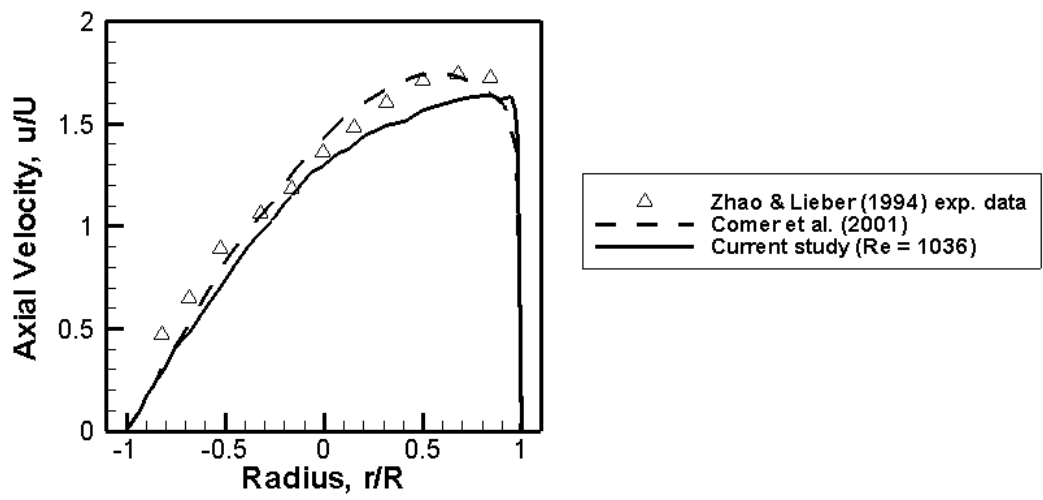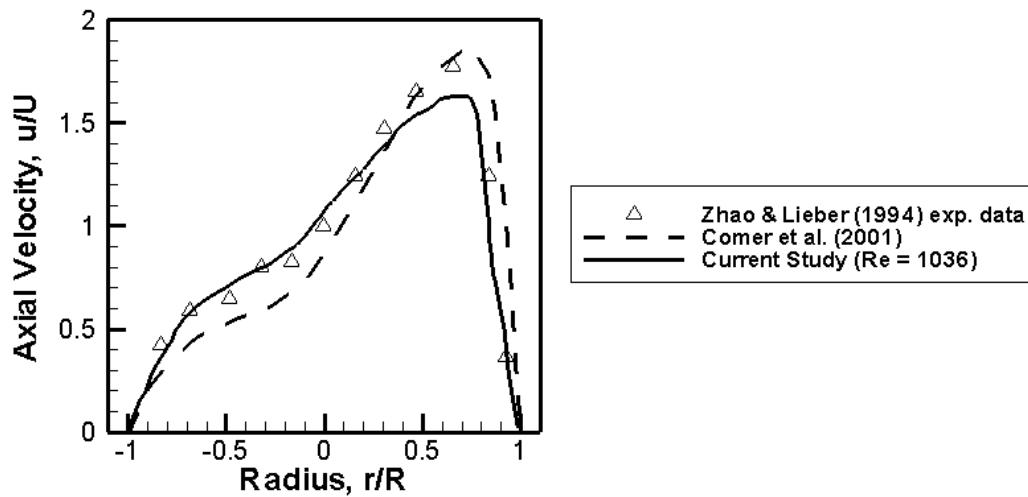
At cross-section $2-2'$, the velocity was found to be parabolic shape with slightly asymmetrical, this might be explained as blockage effects in generation tube of the geometry referred to Fig. 3.8. Current study's velocity showed a smaller peak compared to the other data but made more resemble curve to experimental data compared to data of Comer *et al.* [9]. At beginning of daughter tube, cross-section $10-10'$, the flow was separated by the carina ridge (the separating edge between two adjacent generation tubes) and skew towards the inner wall of generation tube 2 and due to the effect of shear stress of the wall, the flow at cross-section $15-15'$ gradually becomes the shape in Fig. 4.16c. The curves showed that the maximum velocity magnitudes of current study are smaller than data of Zhao & Lieber [85] and Comer *et al.* [9], it is presumably that Comer *et al.* [10] used a rounded carina ridge geometry to calculate these data while current study geometry has sharp carina ridge as displayed in Fig. 3.7.

- Validation

The particle deposition efficiency has been validated for Re = 500 and Re = 2000 in the range of St = 0.02 − 0.12 compared with Comer *et al.*[10] and experimental data [14] and displayed in Fig. 4.17 and Fig. 4.18.
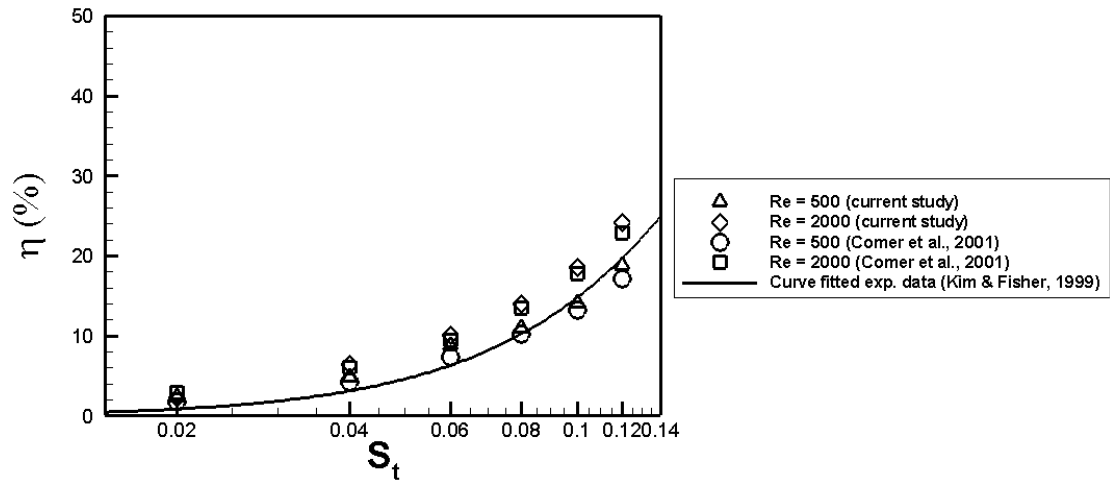
Figure 4.17: Deposition on first bifurcation with Re = 500 and Re = 2000 for different Stokes number, $St = 0.02 - 0.12$
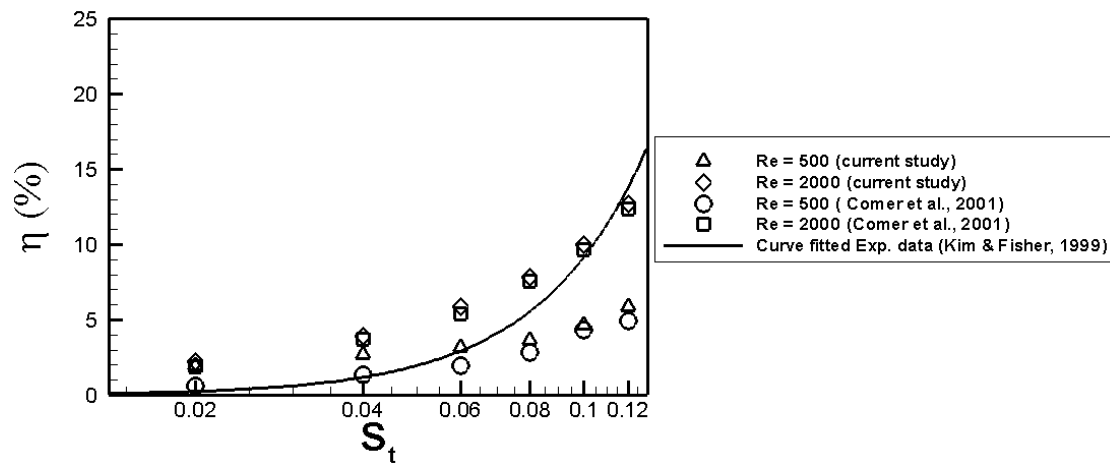


Figure 4.18: Deposition on second bifurcation with Re = 500 and Re = 2000 for different Stokes number, $St = 0.02 - 0.12$

A great agreement was achieved between current model, [10] and [14] for deposition in bifurcation 1 and bifurcation 2 areas. The excellent comparison between three models proves that this configuration model is sufficiently accurate to analyze the particle deposition in turbulent flow. The difference between current results and Comer's result might be explained as Comer *et al.* (2001) used user-enhanced, commercial finite-volume-based program CFX 4.2 while in current study, FLUENT solver was used.

### 4.3.2 Grid Independence Test

The grid independence test was performed for laminar flow simulations with Mesh II and mesh III producing the results virtually identical as shown in Fig. 4.19a,b,c,d. Thus the final mesh of the geometry was chosen as Mesh II (143,102 cells) to perform the rest of the simulations.
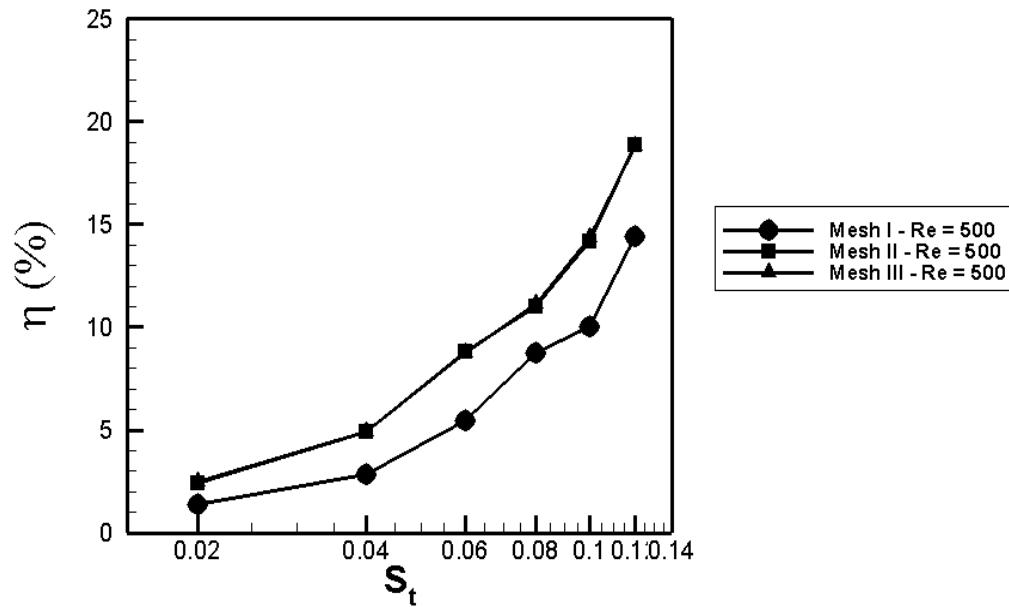


(a) Deposition Efficiency in bifurcation 1 at Re = 500
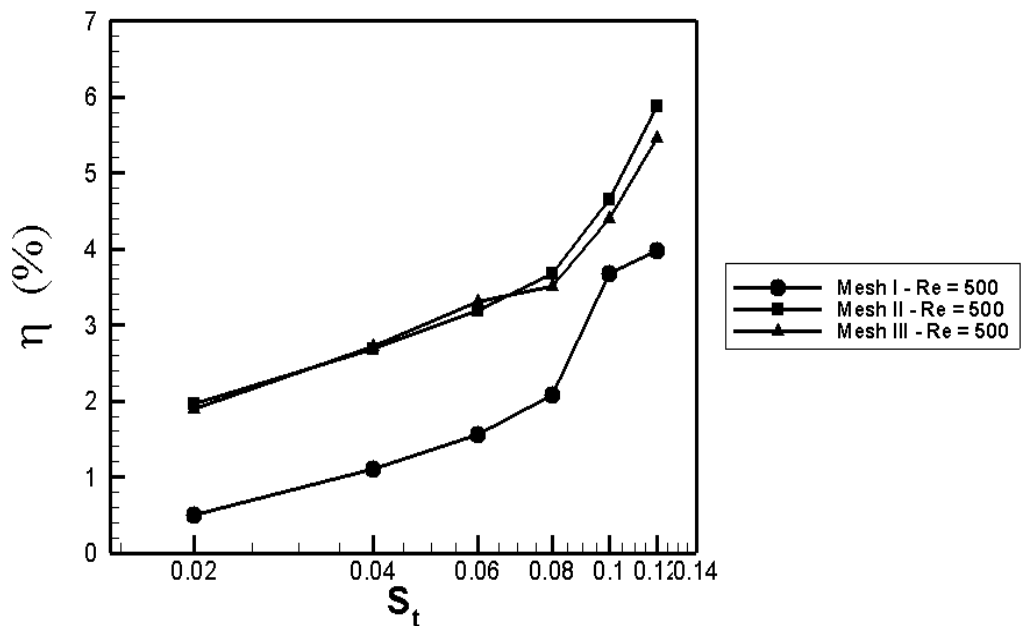


(b) Deposition Efficiency in bifurcation 2 at Re = 500
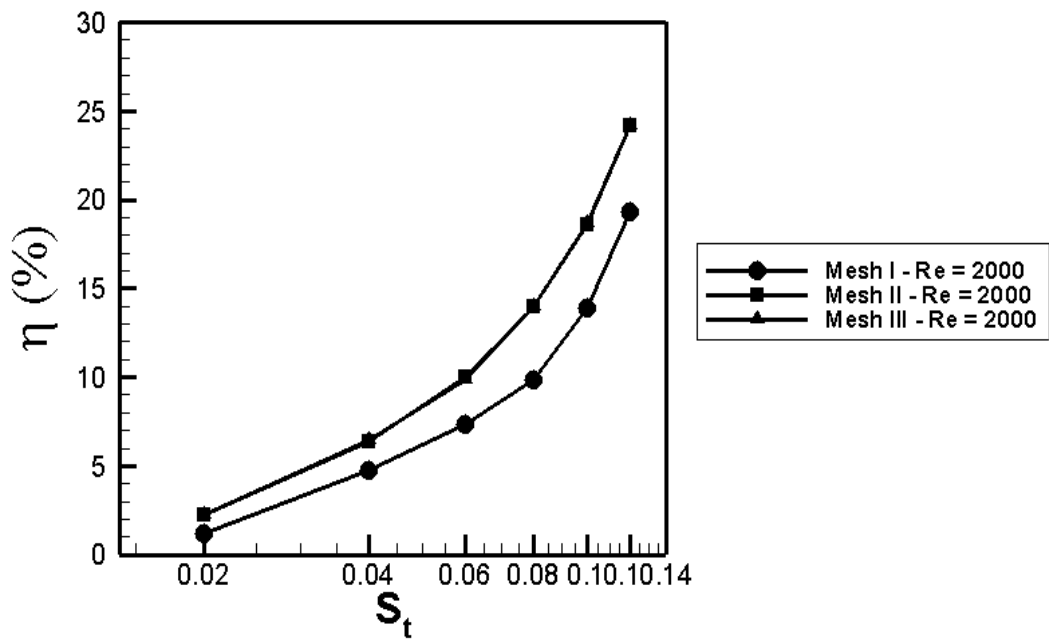
(c) Deposition Efficiency in bifurcation 1 at Re = 2000
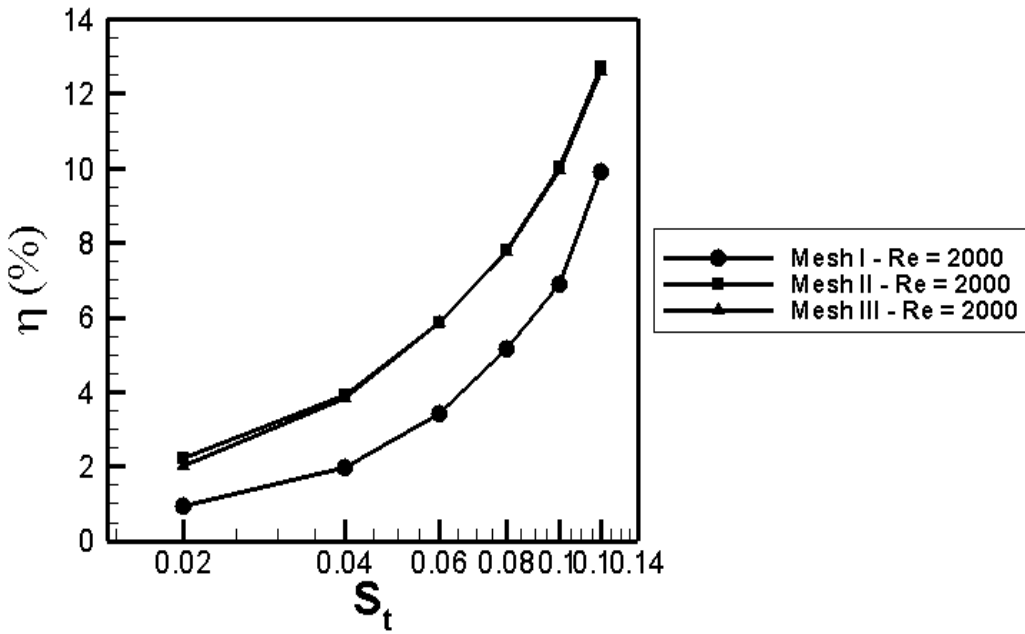


(d) Deposition Efficiency in bifurcation 2 at Re = 2000

Figure 4.19: Grid independence test for Mesh I, Mesh II and Mesh III at bifurcation 1 & 2 for Re = 500 and Re = 2000

Fig. 4.19(a) shows the effect of mesh on the $\eta$ in bifurcation 1 for Re = 500. Mesh II and Mesh III offered same collection efficiency meaning to say that Mesh II is suffice to predict $\eta$ for Re = 500. The detail of the $\eta$ vs. *St* will be discussed further later on. The plots are also shown in Fig. 4.19a where the correlation coefficients are R= 0.9506, 0.9949, 0.9955 for the Mesh I, Mesh II and Mesh III, respectively. That results proved as the mesh was refined, the $\eta$ became smoother of ln *St*.

Fig. 4.19b shows collection efficiency on the three meshes on bifurcation 2 at Re = 500. The $\eta$ curve plot of Mesh I is not smooth, especially at $St = 1$, it can be explained that on Mesh I, the quality of the mesh is coarse which produced imprecise results that resulting in not smooth curve. The error is overcome on Mesh I and Mesh II as shown in Fig. 4.19b. Actually, when the primary flow prediction is erroneous, nothing conclusive can be predicted. It is noted that in all cases an inlet velocity is used for verification purpose. In the results section, it is shown how much that has effect on the collection efficiency. Also in the validation which will be presented in section, this feature of assuming inlet velocity profile will be analyzed more.

Fig. 4.19c and Fig. 4.19d show the collection efficiency for Re = 2000 on bifurcation 1 and bifurcation 2, respectively. The plots also show the best fit polynomial for all three meshes. The $\eta$ vs. *St* behavior will be further addressed in results section. These figures (Fig. 4.19c, 4.19d) clearly show that Mesh II is suffice to present $\eta$ as no further changes occur.

In general, the results of mesh independence test show that the Mesh II and Mesh III produced approximately identical results (the difference is less than 0.2% of deposition efficiency), while Mesh I with coarser quality has an effect to the particle collection. In Mesh I, bigger cell size affects the particle distribution at the inlet injection; while the volume size of the Mesh I is also bigger that may reduce the particle-wall collision, resulting in smaller collection efficiency of Mesh I compared to other meshes as shown in Fig. 4.19. In conclusion, from Fig. 4.19, Mesh II was chosen to perform the simulation for turbulent flow.

### 4.3.3 Velocity Contour Plots

In this work, large eddy simulation (LES) is used to investigate turbulent airway flow in particle deposition. Mesh II is used for all LES calculations with Re > 2000. Two flow rates are simulated in turbulent inlet flow simulation $Q_{in} = 30L/s$ and $Q_{in} = 60L/s$ with Reynolds number, Re = 7264 and Re = 14528, respectively. Fig. 4.20 and Fig. 4.21 show the contour plots of velocity respectively at central plane of double bifurcation for inlet flow rates of 30 L/min and 60 L/min.



| Velocity Magnitude | |
|---|---|
| 1 | 18.60 |
| 2 | 17.40 |
| 3 | 16.10 |
| 4 | 14.90 |
| 5 | 13.70 |
| 6 | 12.40 |
| 7 | 11.20 |
| 8 | 9.93 |
| 9 | 8.69 |
| 10 | 7.45 |
| 11 | 6.21 |
| 12 | 4.97 |
| 13 | 3.73 |
| 14 | 2.48 |
| 15 | 1.24 |
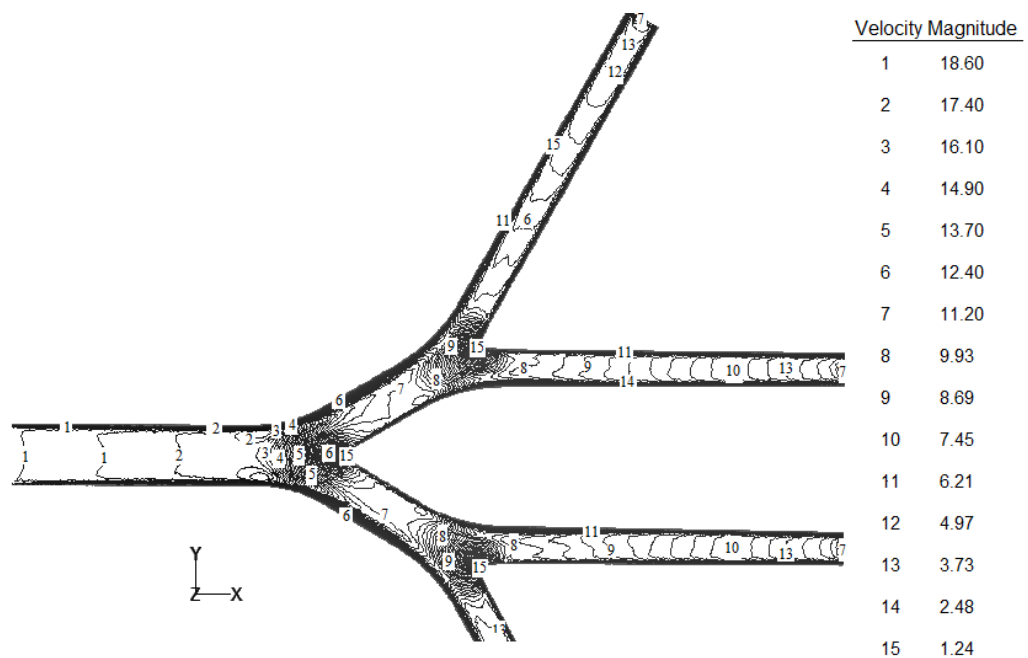
Figure 4.20: Central planar contour plot of velocity profile of flow in double bifurcation for inlet flow rate of 30L/min
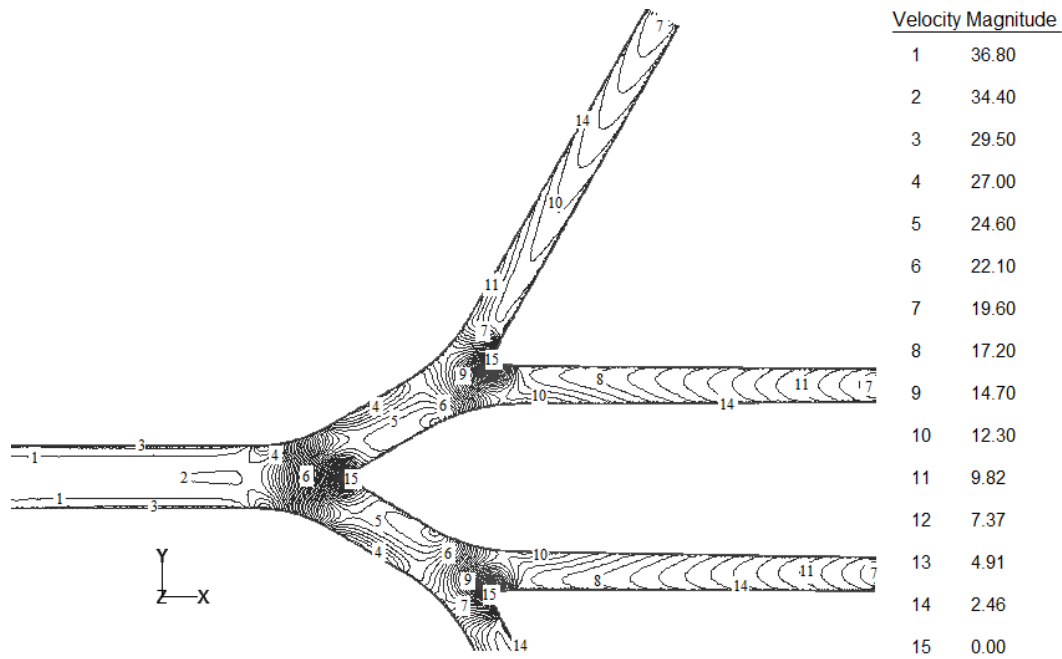
Figure 4.21: Central planar contour plot of velocity profile of flow in double bifurcation for inlet flow rate of 60L/min

Both flow fields of Fig. 4.20 and Fig. 4.21 are symmetrical, causing swirling areas near the carina and tend to disappear when move away from bifurcating zones. The velocity magnitudes at the carina reach the minimum because the flow changes direction and the edge seem to act as an obstacle to the flow and the hit angle is 30 degree (refer to level 15 of Fig. 4.20 and Fig. 4.21). The incoming flow split at the stagnant point (the first carina ridge) generated a weak circulation zone along the outer wall as well as a symmetric pair of vortices perpendicular to the axial flow. This complex vortical flow was split again at second carina ridge, resulting in slower but highly 3D velocity fields in next generation tube [10] and causing velocity field in second generation unstable and tend to slant to outer side of the tubes. In Fig. 4.20, after second bifurcating carina, the flow field presents an asymmetrical M-shape with peaks near the outer wall of the tube; the flow gradually becomes stable and tends to make a normal parabolic shape near the outlet. Whereas, in Fig. 4.21, the flow field shows an asymmetrically parabolic shape at beginning of third generation tubes with peaks near the inner side, it also becomes stable and makes a nearly-parabolic shape

at near end of the tubes; this is due to the effects of flow inside a pipe with an insufficient length.

Fig. 4.22 shows the velocity vector plots at mid-plane for flow rate of 30L/min of the double bifurcation. The arrow mark length is set as same size for clarity. In addition, at 5 different sections, the average velocity are showing in the top left of Fig. 4.22. It is clearly observed that velocity is equally distributed after the first bifurcation, velocity magnitudes at cross-sections 2-2' and 3-3' are identical. But since the length of second generation is insufficiently long to stabilize flow, the flow in second generation is undeveloped which causes the unequal distribution of velocity to third generation. Velocity magnitude at 4-4' (8.67 *m/s*) is smaller than at 5-5' (12.50 *m/s*) proving the explanation in Fig. 4.19 above. Comer *et al.* [9] found that at higher air flow rate the distinct shear layer along the inside wall after the first carina is thinner and the recirculation zone at the outer wall across from the carina ridge area is larger when compared to corresponding flow pattern for laminar flow.
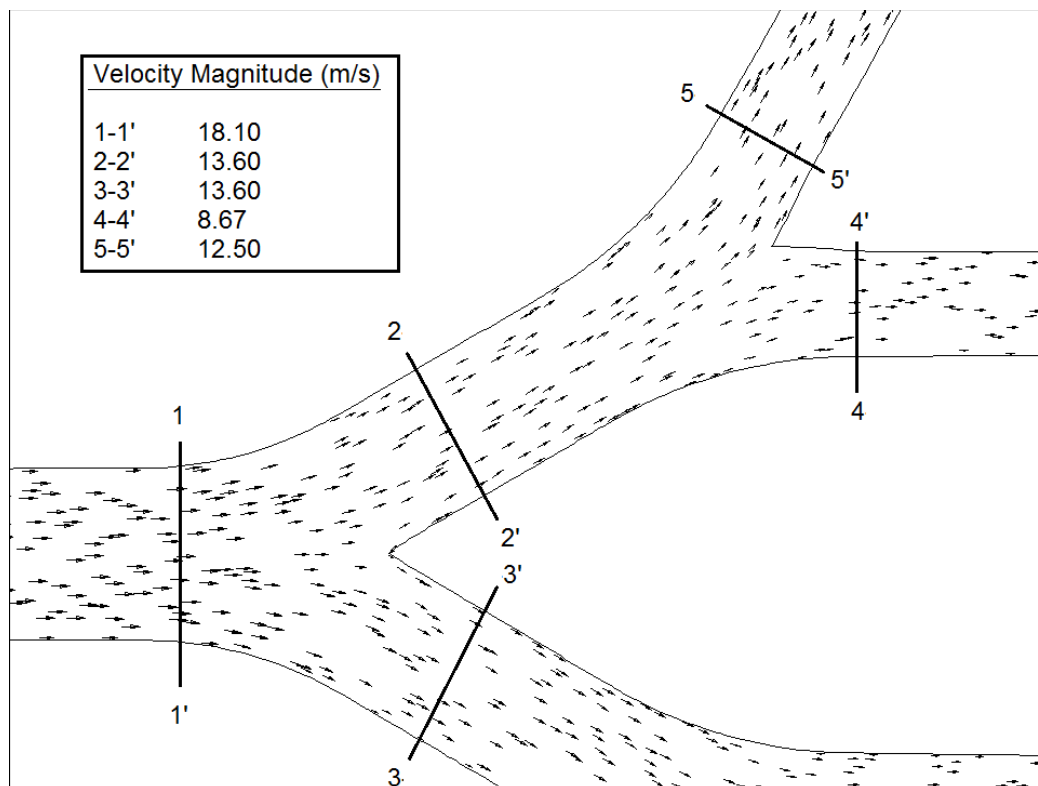


Figure 4.22: Velocity vector plot for planar double bifurcation for inlet flow rate of 30 L/min

### 4.3.4 Particle Injection and Deposition

Fig. 4.23 shows the particle distribution inside the bifurcations and specific particle deposited positions with their initial inlet positions. Particles are fairly distributed after the first bifurcating area but tend to distribute more at the outer tube after second bifurcation. This may be explained as the length of generation 1 is sufficiently long to stabilize the flow, thus causes fair particle distribution to generation 2, but the length of tubes in generation 2 is not long enough causing unstable flow (as explained in Fig. 4.20, Fig. 4.21), which gives more particles to outer tubes of generation 3. It is presumed that particle final deposition depends on initial injection position from the inlet, those from the center area of inlet (position x) tend to deposit at the first bifurcation (at position x'), those injected at near the circle boundary tend to have the final position at outer tube of third generation (as lines a-a' and o-o'), while those from area around center of inlet boundary will go to inner tube of third generation (as lines c-c' and z-z'). Those from area between 'a'-'e' or 'o'-'c' have chances to deposit on second bifurcation.
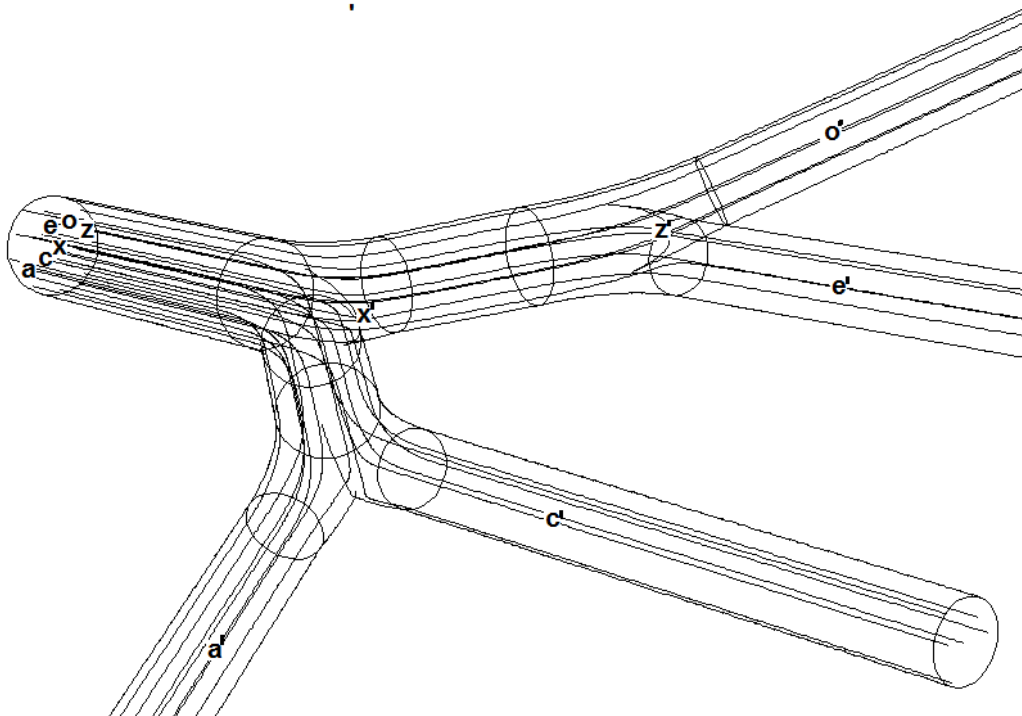


Figure 4.23: Particle behavior in double bifurcation

The final deposition location of particles with Stokes number of 0.12 for flow rates of 30 L/min and 60 L/min as shown in Fig. 4.24.
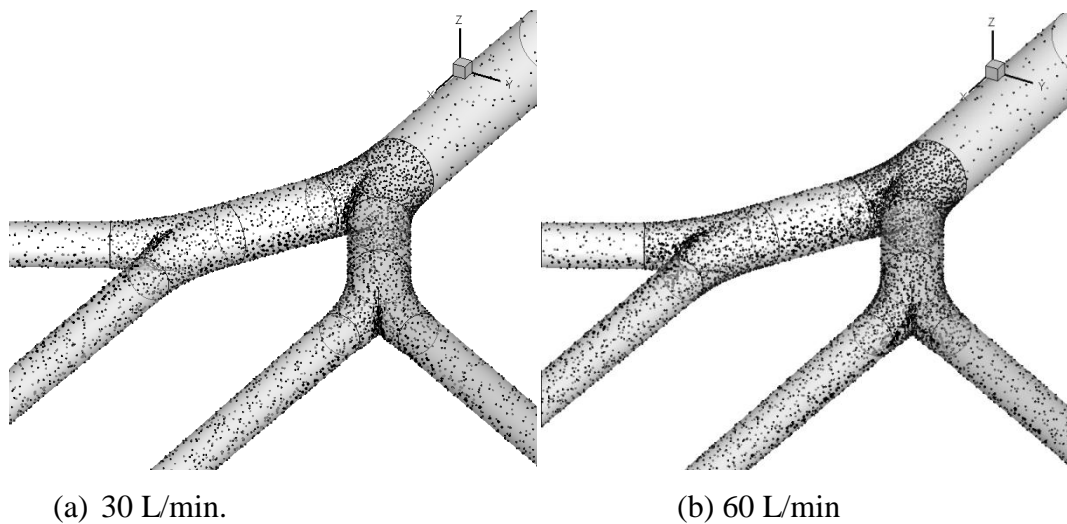


(a) 30 L/min.                          (b) 60 L/min

Figure 4.24: Final particle deposition with Stokes number, *St* = 0.12 for inlet flow rates of: (a) 30 L/min; (b) 60 L/min

For both cases, it is observed that the number of particles deposited on the first generation tube is less than the bifurcating area. This can be explained as the tube is assumed to be smooth and no obstacles on it, the particle deposited mostly based on the turbulence of fluid. Meanwhile, when the particle flow approaching the bifurcating area, the flow velocity was reduced since bifurcating area can be considered as a blockage and that explained the number of particle deposited in the carina ridge (bifurcation areas) suddenly increased. Both cases showed that the particles tend to deposit on inner side of generation tube after bifurcations, this might be explained as flow was divided by carina ridge and skew toward inner side. The particles deposited more at carina ridge areas due to high velocity and high Stokes number, therefore, the particle with $Q = 60L/\min$ showed a denser deposition concentration than the particle with $Q = 30L/\min$ in the first bifurcation.

Fig. 4.25 shows the graph comparison of particle deposition efficiency with different Stokes number (ranging from 0.02 − 0.12) for turbulent flow with inlet flow rates of 30 L/min and 60 L/min. The particle concentrations at carina ridges for both cases are highest.
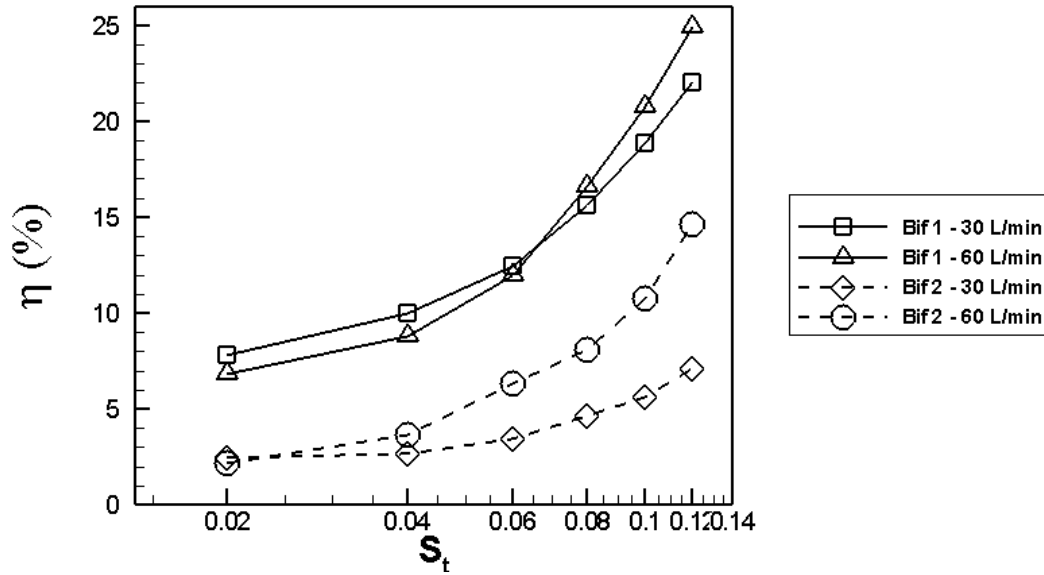
Figure 4.25: Deposition efficiency with different Stokes number for inlet flow rate of 30 L/min and 60 L/min

The flow in the second bifurcation tube is considered highly disturbed flow field, with additional consideration that the flow rate in next generation reduces ( $Q_2 = 0.5Q_1$ but $A_2 \approx 0.7A_1$ due to $d_2 = 0.83d_1$ which leads to $v_2 = 0.71v_1$ and $Re_2 = 0.71Re_1$ ). The particle deposition is primarily occurred based on the direct impaction at the divider (carina ridges), thus greater Reynolds and Stokes numbers resulting in higher depositions. It is accepted that while the flow may be marginally turbulent at the inlet, but it rapidly becomes laminar after few generations, which causing the reduction of deposition in bifurcation [74]. The lower deposition efficiency in second bifurcation can be explained as the flow in second bifurcations has lower Reynolds number compared to the first one. It can be seen that the inlet flow rates have effects on the deposition efficiency on bifurcations. While the difference of particle deposition on bifurcation 1 for both flow rates is insignificant (maximum 2% difference), the DE for bifurcation 2 shows great changes with higher Stokes number. The deposition efficiency $\eta$ for $St = 0.02$ is identical but it increases as Stokes number increases and reach to approximately 8% of difference. And it is also noticed that particles with greater Stokes number have higher deposition

efficiency. This can be explained as the particle with high Stokes number has bigger size and mass, thus the inertia force acting on the particle is high, and therefore the opportunity of deposition is higher. The deposition efficiency is proportional to Reynolds number and Stokes numbers.

CHAPTER 5

CONCLUSION AND RECOMMENDATION

## 5.1 Conclusion and Contribution

The particle dynamics in an unsteady vortical flow over a square cylinder placed in a channel was investigated for Reynolds numbers of Re = 150, 300, 600, 900 and 1200 by solving the incompressible Navier-Stokes equations. The detailed flow visualizations were then employed to characterize particle dispersion as a function of the Reynolds number and the particle Stokes number (refer to section 4.1). Important observations are as follows: With Re between 300 and 1200, the flow past the square cylinder was characterized by an unsteady fluid-wake flow and asymmetric vortex shredding near the obstruction. For $\mathrm{Re} < \mathrm{Re}_{crit} = 300$ (in this study Re =150), the fluid flows steadily and vortex shredding does not exist (refer to section 4.1). For Re = 1200, vortex get elongated, bigger and stronger. The particle distribution depends on vortical structures and Stokes number. Due to the fact that human nasal cavity and human lung consist of many obstacles, this study has provided basic understanding of primary flow and particle dynamics.

A detailed flow structure in a nasal cavity was modeled using CFD for the inlet Reynolds number, Re ~1500-6000. The model developed was validated experimental data and previously published numerical data and shows a good trend of the collection efficiency (refer to section 4.3.1). By increasing Reynolds number, the collection can be increased as high as ~20%. This might be used by the drug delivery scientists. In this part of the research, a detailed flow structure in a nasal cavity is modeled using CFD for the inlet Reynolds number, Re ~1500, 3000, 4000 and 6000. First the solutions were made less dependent on the mesh size. For this purpose the mesh was

considered all hexahedral mesh of 25,225 (Mesh I), 109,804 (Mesh II) and 568,801 cells (Mesh III). The configuration was decided that Mesh II (109,804 cells) was optimized to provide reasonable results with current computer resources. After that particle of various sizes was injected from the nostrils and the fate of the particles was tracked and validated with experimental data and numerical data; a good trend of the collection efficiency was shown. For Re up to 6000, the fluid flow dynamics was explored using $k - \varepsilon$ realizable turbulence model (refer to section 4.2). It was found there are few recirculation zones in the nasal cavity and local Reynolds number change along the flow as the cross-sectional area does vary. Hence the particle deposition in nasal cavity showed complexity as: low Stoke number particle followed the fluid flow, whereas as the Stoke number increases, the particles do not follow the fluid. For inertial parameter $10^4 - 3 \times 10^5$, the change in collection efficiency is the highest. Also for $St = 1 - 12$, the collection can be increased significantly by changing the flow rate. It is quantified that by increasing Re, the $\eta$ can be increased as high as ~20%.

For the simulation of fluid flow and particle dynamics in lower respiratory system, the capability of large eddy simulation (LES) in modeling turbulent flow in double bifurcation was investigated. The model configuration was validated for laminar flow (Re = 500 and Re = 2000) for a Stoke number (ranging from 0.02 to 0.12) with data from Comer *et al.* (refer to section 4.3.1). The higher Stokes number gives higher collection. The verification and validation results showed that LES is suitable to model the turbulent flow in lower airway. The particle deposition efficiency $\eta$ is affected by the Reynolds numbers and Stokes numbers. While the higher Stokes number gives higher $\eta$, Reynolds number also cause effects to the flow inside the bifurcating tubes. For 30 L/min inlet flow rate, the flow field presents an asymmetrical M-shape with peaks near the outer wall of the tube. Whereas, for 60 L/min inflow, an asymmetrically parabolic shape at beginning of third generation tubes with peaks near the inner side. And flows become stable and make a parabolic shape at near outlets.

From the overall findings, the study of this thesis can provide some useful information to improve the medical treatment for human, such as:

- Higher inlet velocity may produce higher deposition on nasal cavity.
- The bigger size of aerosol particles can lead the deposition deeper in the lungs.

## 5.2 Recommendation

Different people have different nasal cavity shape, some special patients have specific nasal cavity (asymmetrical for left and right sides, short in length). With the current findings, the drug delivery can also be customized. Reconstruction of those special shapes can give more chances to understand and contribute to medical knowledge. The University should have extensive CAD package for the reconstructing of complex geometry medical imaging. Access to powerful HPC (high performance computing) is a must for this kind of 3-D simulations.

# REFERENCES

[1] I. Balásházy and W. Hofmann, "Particle deposition in airway bifurcations-II. Expiratory flow," *Journal of Aerosol Science,* vol. 24, pp. 773-786, 1993.

[2] S. T. Jayaraju, "Study of the air flow and aerosol transport in the Human Upper Airway using LES and DES Methodologies," 2009.

[3] *World Health Organization (WHO) annual report,* 2006.

[4] X. L. Yang, Y. Liu, and H. Y. luo, "Respiratory flow in obstructed air ways," *Journal of Biomechanics,* vol. 39, pp. 2743-2751, 2006.

[5] A. R. Clark, *Medical aerosol inhalers: past, present, and future*. Colchester, ROYAUME-UNI: Taylor &amp; Francis, 1995.

[6] N. J. Roland, R. K. Bhalla, and J. Earis, "The local side effects of inhaled corticosteroids: current understanding and review of the literature," *Chest,* vol. 127, p. 1077, 2005.

[7] I. Balásházy, "Simulation of Particle Trajectories in Bifurcating Tubes," *Journal of Computational Physics,* vol. 110, pp. 11-22, 1994.

[8] Y.-S. Cheng, Y. Yamada, H.-C. Yeh, and D. L. Swift, "Deposition of Ultrafine Aerosols in a Human Oral Cast," *Aerosol Science and Technology,* vol. 12, pp. 1075 - 1081, 1990.

[9] J. K. Comer, C. Kleinstreuer, and C. S. Kim, "Flow structures and particle deposition patterns in double-bifurcation airway models. Part 2. Aerosol transport and deposition," *Journal of Fluid Mechanics,* vol. 435, pp. 55-80, 2001.

[10] J. K. Comer, C. Kleinstreuer, and Z. Zhang, "Flow structures and particle deposition patterns in double-bifurcation airway models. Part 1. Air flow fields," *Journal of Fluid Mechanics,* vol. 435, pp. 25-54, 2001.

[11] C. S. Kim, D. M. Fisher, D. J. Lutz, and T. R. Gerrity, "Particle deposition in bifurcating airway models with varying airway geometry," *Journal of Aerosol Science,* vol. 25, pp. 567-581, 1994.

[12] K. Richter, S. Janicki, R. A. Jörres, and H. Magnussen, "Acute protection against exercise-induced bronchoconstriction by formoterol, salmeterol and terbutaline," *European Respiratory Journal,* vol. 19, pp. 865-871, May 1, 2002 2002.

[13] Z. Zhang, C. Kleinstreuer, and C. S. Kim, "Cyclic micron-size particle inhalation and deposition in a triple bifurcation lung airway model," *Journal of Aerosol Science,* vol. 33, pp. 257-281, 2002.

[14] C. S. Kim and D. M. Fisher, "Deposition Characteristics of Aerosol Particles in Sequentially Bifurcating Airway Models," *Aerosol Science and Technology,* vol. 31, pp. 198 - 220, 1999.

[15] *Computational fluid-particle dynamics lab, NC state university, Raleigh, NC.*

[16] M. Brouns, S. T. Jayaraju, C. Lacor, J. D. Mey, M. Noppen, W. Vincken, and S. Verbanck, "Tracheal stenosis: A flow dynamics study," *Journal of Applied Physiology,* vol. 102, pp. 1178-1184, 2007.

[17] J. Russo, R. Robinson, and M. J. Oldham, "Effects of cartilage rings on airflow and particle deposition in the trachea and main bronchi," *Medical Engineering & Physics,* vol. 30, pp. 581-589, 2008.

[18] W. H. Finlay, "The mechanics of inhaled pharmaceutical aerosols," *Academic Press, London, UK.,* 2001.

[19] G. Batchelor, "Introduction to Fluid Mechanics," 2000.

[20] C. J. Geankoplis, "Transport Processes and Separation Process Principles," *Prentice Hall Professional Technical Reference,* 2003.

[21] C. Noakes and A. Sleigh, "Real Fluids," *An Introduction to Fluid Mechanics.,* 2010.

[22] J. A. Oliver and J. P. Meyer, "Single-phase heat transfer and pressure drop of the cooling of water inside smooth tube for transitional flow with different inlet geometries," *HVAC&R Journal,* vol. 16, pp. 471-496, 2010.

[23] R. Nave, "Laminar Flow," *Hyper Physics,* 2005.

[24] G. Falkovich and K. R. Screenivasan, "Lessons from hydrodynamic turbulence," *Physics Today,* vol. 59, pp. 43-49, 2006.

[25] B. E. Launder and D. B. Spalding, "Lectures in Mathematical Models of Turbulence," *Academic Press, London, England,* 1972.

[26] T. H. Shih, A. S. Liou, Z. Yang, and J. Zhu, "A new k-epsilon eddy-viscosity model for high Reynolds number turbulent flows - model development and validation," *Computers & Fluids,* vol. 24, pp. 227-238, 1995.

[27] M. Rhodes, *Introduction to Particle Technology.* New York: John Wiley & Sons, Inc., 2005.

[28] M. Kawaguti, "Numerical solution of the Navier-Stokes equations for the flow in a two-dimensional cavity," *J. Phys. Soc. Japan,* vol. 16, pp. 2307-2316, 1961.

[29] B. D. Bowen, S. Levine, and N. Epstein, "Fine Particle Deposition in Laminar Flow Through a Parallel-Plate and Cylindrical Channels," *J. Colloid and Interface Sic.,* vol. 54, pp. 375-390, 1976.

[30] F. Stratmann, H. Fissan, and T. W. Petersen, "Particle Deposition onto a Flat Surface from a Point Particle Source," *American Chemical Society,* vol. 31, pp. 39-41, 1988.

[31] N. T. Vatistas, "Effect of adhesion time on particle deposition: reentrainment and rolling," *Industrial & Engineering Chemistry Research,* vol. 31, pp. 1549-1554, 1992.

[32] Vašak, F. k, F. Kaštánek, B. D. Bowen, C. Y. Chen, and N. Epstein, "Fine particle deposition in laminar and turbulent flows," *The Canadian Journal of Chemical Engineering,* vol. 73, pp. 785-792, 1995.

[33] A. G. Konstandopoulos and D. E. Rosner, "Inertial effects on thermophoretic transport of small particles to walls with streamwise curvature--I. Theory," *International Journal of Heat and Mass Transfer,* vol. 38, pp. 2305-2315, 1995.

[34] R. W. Davis, E. F. Moore, and L. P. Purtell, "A numerical-experimental study of confined flow around rectangular cylinders," *Phys. Fluids,* vol. 27, pp. 46-59, 1984.

[35] K. R. May and R. Clifford, "The impaction of aerosol particles on cylinders, spheres, ribbons and discs," *Ann. Occup. Hyg.,* vol. 10, pp. 83-95, 1967.

[36] B. J. Lázaro and J. C. Lasheras, "Particle dispersion in the developing free shear layer. Part 2. Forced flow," *Journal of Fluid Mechanics,* vol. 235, pp. 179-221, 1992.

[37] E. K. Longmire and J. K. Eaton, "Structure of a particle-laden round jet," *Journal of Fluid Mechanics,* vol. 236, pp. 217-257, 1992.

[38] D. F. Proctor, "The upper airway," *In The Nose, eds. D.F. Proctor and I. Anderson. New York: Elsevier Biomedical Press,* 1982.

[39] D. F. Proctor, "Physiology of the upper airway," 1964.

[40] D. L. Swift and J. C. Strong, "Nasal deposition of ultrafine 218 Po Aerosols in human subjects," *j. Aerosol Sci.,* vol. 27, pp. 1125-1132, 1996.

[41] L. M. Beidler, "The chemical senses: gustation and olfaction," *In Medical Physiology, ed. V.B. Mountcastle. St. Louis: C.V. Mosby Co.,* 1980.

[42] B. Berglund and T. Lindvall, "Olfaction," *In the Nose: Upper Airway Physiology and the Atmospheric Environment, eds. D.F. Proctor and I. Andersen. New York: Elsevier Biomedical Press.,* 1982.

[43] N. Mygind, M. Pedersen, and H. Nielsen, "Morphology of the upper airway epithelium," *In The Nose, eds. D.F. Proctor and I. Anderson. New York: Elsevier Biomedical Press,* 1982.

[44] N. Cauna, "Blood and nerve supply of the nasal lining," *In The Nose, eds. D.F. Proctor and I. Anderson. New York: Elsevier Biomedical Press,* 1982.

[45] K. Inthavong, Z. F. Tian, J. Y. Tu, W. Yang, and C. Xue, "Optimising nasal spray parameters for efficient drug delivery using computational fluid dynamics," *Computers in Biology and Medicine,* vol. 38, pp. 713-726, 2008.

[46] B. Bailey, "Nasal function and evaluation, nasal obstruction," *In Head and Neck Surgery: Otolaryngology. 2nd ed. New York, NY: Lippincott-Raven.,* 1998.

[47] D. F. Proctor, *Physiology of the upper airway*, 1964.

[48] D. L. Swift and D. F. Proctor, *Access of air to the respiratory tract. In Respiratory Defense Mechanism,*. NY, USA: Marcel Dekker, 1977.

[49]     D. L. Swift, "Inspiratory inertial deposition of aerosols in human nasal airway replicate casts: Implication for the proposed NCRP lung model," *Radiation Protection Dosimetry,* vol. 38, pp. 29-34, 1991.

[50]     R. A. Guilmette, Y. S. Cheng, H. C. Yeh, and D. L. Swift, "Deposition of 0.005 -12 μm monodispersed particles in a computer-milled, MRI-based nasal airway replica," *Inhalation Toxicology,* vol. 6, pp. 395-399, 1994.

[51]     G. J. Zwartz and R. A. Guilmette, "Effect of flow rate on particle deposition in a replica of a human nasal airway," *Inhalation Toxicology,* vol. 13, pp. 109-127, 2001.

[52]     S. Hauermann, A. G. Bailey, M. R. Bailey, G. Etherington, and M. Youngman, "The influence of breathing patterns on particle deposition in a nasal replicate cast," *Journal of Aerosol Science,* vol. 33, pp. 923-933, 2002.

[53]     Y. S. Cheng, "Aerosol deposition in the extrathoracic region," *Aerosol Science and Technology,* vol. 37, pp. 659-671, 2003.

[54]     C. Croce, R. Fodil, M. Durand, G. Sbirlea-Apiou, G. Caillibotte, J.-F. Papon, J.-R. Blondeau, A. Coste, D. Isabey, and B. Louis, "*In Vitro* Experiments and Numerical Simulations of Airflow in Realistic Nasal Airway Geometry," *Annals of Biomedical Engineering,* vol. 34, pp. 997-1007, 2006.

[55]     K. Keyhani, P. W. Scherer, and M. M. Mozell, "Numerical simulation of airflow in the human nasal cavity," *Journal of Biomechanical Engineering,* vol. 117, pp. 429-441, 1995.

[56]     I. Hahn, P. W. Scherer, and M. M. Mozell, "Velocity profiles measured for airflow through a large-scale model of the human nasal cavity," *Journal of Applied Physiology,* vol. 75, pp. 2273-2287, 1993.

[57]     M. Lippmann, D. B. Yeates, and R. E. Albert, "Deposition, Retention, and Clearance of Inhaled Particles," *British Journal of Industrial Medicine,* vol. 37, pp. 337-362, 1980.

[58]     I. Gonda and E. Gipps, "Model of Disposition of Drugs Administered into the Human Nasal Cavity," *Pharmaceutical Research,* vol. 7, pp. 69-75, 1990.

[59]     D. L. Swift and D. F. Proctor, "Access of air to the respiratory tract.," *In Respiratory Defense Mechanism, eds. J.D. Brain, D.F. Proctor and L.M. Reid. New York: Marcel Dekker,* 1977.

[60]    E. R. Weibel, "Morphometry of the human lung," *Academic Press, New York,* 1963.

[61]    Y. Li and A. Naguib, "An oscillating hot-wire technique for resolving the magnitude and direction of velocity measurements using single hot-wire sensors," *Experiments in Fluids,* vol. 34, pp. 597-606, 2003.

[62]    D. Kilpatrick, T. Linderer, R. E. Sievers, and J. V. Tyberg, "Measurement of coronary sinus blood flow by fiber-optic laser Doppler anemometry," *American Journal of Physiology - Heart and Circulatory Physiology,* vol. 242, pp. 1111-1114, 1982.

[63]    W. W. Durgin and L. C. Neale, "Laser Doppler Anemometry for Flow Measurement," in *Symposium on Flow in Open Channels and Closed Conduits*, NBS, Gaithersburg, MD, 1977, pp. 471-477.

[64]    Y. Zhou and Y. S. Cheng, "Particle deposition in a cast of human tracheobronchial airways," *Aerosol Science and Technology,* vol. 39, pp. 492-500, 2005.

[65]    R. B. Schlesinger, J. L. Gurman, and M. Lippmann, "Particle deposition within bronchial airways: Comparisons using constant and cyclic inspiratory flows," *Annals of Occupational Hygiene,* vol. 26, pp. 47-64, 1982.

[66]    R. B. Schlesinger, D. E. Bohning, T. L. Chan, and M. Lippmann, "Particle deposition in a hollow cast of the human tracheobronchial tree," *Journal of Aerosol Science,* vol. 8, pp. 429-445, 1977.

[67]    C. A. Pope, D. W. Dockery, and J. Schwartz, "Review of epidemiological evidence of health effects of particulate air pollution," *Inhalation Toxicology,* vol. 7, pp. 1-18, 1995.

[68]    M. Kreuzer, M. K. Muller, A. Branchner, M. Gerken, B. Grosche, T. Wiethege, and H. E. Wichmann, "Histopathologic findings of lung carcinoma in German uranium miners," *Cancer,* vol. 89, pp. 2613-2621, 2000.

[69]    I. Balashazy, W. Hoffmann, and T. Heistracher, "Local particle deposition patterns may play a key role in the development of lung cancer.," *Journal of Applied Physiology,* vol. 94, pp. 1719-1725, 2003.

[70]    A. R. Clark, "Medical aerosol inhaler: Past, present and future," *Aerosol Science and Technology,* vol. 22, pp. 374-391, 1995.

[71]    N. J. Roland, R. K. Bhalla, and J. Earis, "The local side effects of inhaled corticosteroids: Current understanding and review of the literature," *Chest,* vol. 126, pp. 213-219, 2004.

[72]    R. Hess, "Aerosol Delivery Devices in the Treatment of Asthma," *Respiratory Care,* vol. 53, pp. 699-725, 2008.

[73]    S. Jafari, M. Salmanzadeh, M. Rahnama, and G. Ahmadi, "Investigation of particle dispersion and deposition in a channel with a square cylinder obstruction using the lattice Boltzmann method," *Journal of Aerosol Science,* vol. 41, pp. 198-206, 2010.

[74]    N. Nowak, P. P. Kakade, and A. V. Annapragada, "Computational Fluid Dynamics Simulation of Airflow and Aerosol Deposition in Human Lungs," *Annals of Biomedical Engineering,* vol. 31, pp. 374-390, 2003.

[75]    C. Van Ertbruggen, C. Hirsch, and M. Paiva, "Anatomically based three dimensional model of airways to simulate flow and particle transport using computational fluid dynamics," *J Appl Physiol,* vol. 98, pp. 970-980, 2005.

[76]    K. Nielsen, M. Skov, B. Klug, M. Ifversen, and H. Bisgaard, "Flow-dependent effect of formoterol dry-powder inhaled from the Aerolizer," *European Respiratory Journal,* vol. 10, pp. 2105-2109, September 1, 1997 1997.

[77]    ANSYS, "FLUENT GAMBIT Manual."

[78]    M. R. Maxey and J. J. Riley, "Equation of motion for a small rigid sphere in a nonuniform flow," *Physics of Fluids Journal,* vol. 26, pp. 883-889, April 1983 1983.

[79]    C. W. Hirt, B. D. Nichols, and N. C. Romero, "SOLA: A numerical solution algorithm for transient fluid flows," *Los Alamos National Laboratory Report, Los Alamos, NM, April, LA-5852.,* 1975.

[80]    F. H. Harlow and J. E. Welch, "Numerical Calculation of Time-Dependent Viscous Incompressible Flow of Fluid with Free Surface," *Physics of Fluids,* vol. 8, pp. 2182-2189, 1965.

[81]    S. K. Aggarwal and F. Peng, "A Review of Droplet Dynamics and Vaporization Modeling for Engineering Calculations," *Journal of Engineering for Gas Turbines and Power,* vol. 117, pp. 453-461, 1995.

[82]  I. E. Barton, "Computation of particle tracks over a backward-facing step," *Journal of Aerosol Science,* vol. 26, pp. 887-901, 1995.

[83]  Y. S. Cheng, T. D. Holmes, J. Gao, R. A. Guilmette, S. Li, Y. Surakitbanharn, and C. Rowlings, "Characterization of nasal spray pumps and deposition pattern in a replica of the human nasal airway," *Journal of Aerosol Medicine: Deposition, Clearance, and Effects in the Lung,* vol. 14, pp. 267-280, 2001.

[84]  C. S. Kim and D. M. Fisher, "Deposition characteristics of aerosol particles in successively bifurcating airway models," *Aerosol Sci. Tech. ,* vol. 31, pp. 198-220, 1999.

[85]  Y. Zhao and B. B. Lieber, "Steady Inspiratory Flow in a Model Symmetric Bifurcation," *Journal of Biomechanical Engineering,* vol. 116, pp. 488-496, 1994.

[86]  N. C. Straub, Ed., *Section V, The Respiratory Sysem, in Physiology*. Mosby, St. Louis: eds. RM Berne & MN Levy, 1998, p.^pp. Pages.

[87]  B. S. Massey and J. Ward-Smith, *Mechanics of FLuids*, 7th ed. UK: Nelson Thornes, 1998.

[88]  F. Odar and W. S. Hamilton, "Forces on a sphere accelerating in a viscous fluid," *Journal of Fluid Mechanics,* vol. 18, pp. 302-314, 1964.

[89]  J. T. Kelly, J. S. Asgharian, Kimbell, and B. A. Wong, "Particle deposition in human nasal cavity airway replicas manufactured by different methods. Part 1: Inertial regime particles," *Aerosol Science and Technology,* vol. 38, pp. 1063-1071, 2004.

[90]  R. E. Pattle, "The retention of gases particles in the human nose," *In Inhaled particles and vapors,* 1961.

[91]  Y. Zhang, W. H. Finlay, and E. A. Matida, "Particle deposition measurements and numerical simulation in a highly idealized mouth-throat," *Journal of Aerosol Science,* vol. 35, pp. 789-803, 2004.